國立交通大學

機械工程學系

博 士 論 文

驅動訊號波形、噴孔幾何參數與噴孔流道親疏水
性對噴墨頭液滴噴射行為影響之研究

Investigation of the effect of a transducer pulse, nozzle

geometry and liquid hydrophobicity on the drop formation of an

ink jet printhead

研 究 生：賴志銘

指導教授：林振德　教授

中 華 民 國 九 十 九 年 七 月

驅動訊號波形、噴孔幾何參數與噴孔流道親疏水性對噴墨頭液滴噴射

行為影響之研究

Investigation of the effect of a transducer pulse, nozzle geometry and
liquid hydrophobicity on the drop formation of an ink jet printhead

研究生：賴志銘　　　　　Student：Jr-Ming Lai

指導教授：林振德　　　　Advisor：Dr. Jenn-Der Lin

國 立 交 通 大 學

機 械 工 程 學 系

博 士 論 文

A Thesis

Submitted to Department of Mechanical Engineering

College of Engineering

National Chiao Tung University

in partial Fulfillment of the Requirements

for the Degree of

Doctor of Philosophy

in

Mechanical Engineering

July 2010

Hsinchu, Taiwan, Republic of China

中 華 民 國 九 十 九 年 七 月

驅動訊號波形、噴孔幾何參數與噴孔流道親疏水性對噴墨頭液滴噴射

行為影響之研究

學生： 賴志銘　　　　　　　　　　指導教授： 林振德 博士

國立交通大學機械工程學系博士班 （熱流組）

中文摘要

　　本研究利用數值模擬的方法，探討驅動訊號波形對一壓電式噴墨頭液滴噴射行為之影響。為了對驅動訊號波形與液滴形成之關係有一完整的了解，研究中將一雙極方波訊號區分成供液段、補液段、噴出段、間歇段、回拉段與靜止段，並找出每一波形區段的獨立參數，分析不同區段不同獨立參數組合，對噴出之主液滴體積、主液滴飛行速度、液滴斷裂時間與衛星液滴形成之影響。數值模擬部分，採用商業化計算流體力學軟體 CFD-ACE+來進行；透過邊界條件給予相對於電壓訊號之壓電隔板形變位移量以模擬不同訊號波形之壓電致動行為；利用流體體積－片段線性界面重建法來做液氣界面的時變追蹤，並以連續表面力法來考慮流體表面張力的效應。研究結果顯示，主液滴體積主要與訊號噴出段所造成最大腔體形變量有關；主液滴飛行速度主要與訊號噴出段之斜率有關。此外，縮短訊號間歇段能有效地抑制衛星液滴的形成。為了探討噴孔流道親疏水性與噴孔流道曲率對液滴噴射行為的影響，我們簡化液滴生成與噴射機構，採用一噴孔片透

過壓電材料的形變振動，將液體噴射而出的設計。研究中首先利用

CFD-ACE+建立一數值模型，再設計一液滴噴射實驗，利用實驗觀測

結果來驗證數值模型。研究結果顯示，當噴孔直徑越小，主液滴體積

越小，主液滴飛行速度越快。當噴孔片振動振幅越大或振動頻率越

快，會使主液滴體積變小，主液滴飛行速度變快。此外，在所考慮不

同流道曲率中，線性流道曲率會產生較小主液滴體積和較快的主液滴

飛行速度。當噴孔流道表面由親水變化到疏水時，主液滴體積會變

小，主液滴飛行速度會變快。
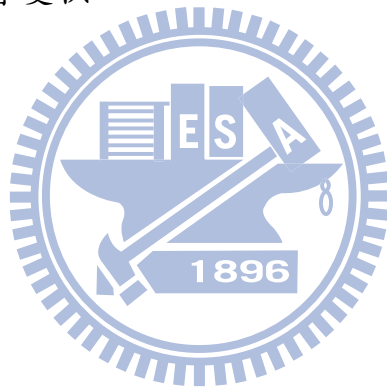
Investigation of the effect of a transducer pulse, nozzle geometry and

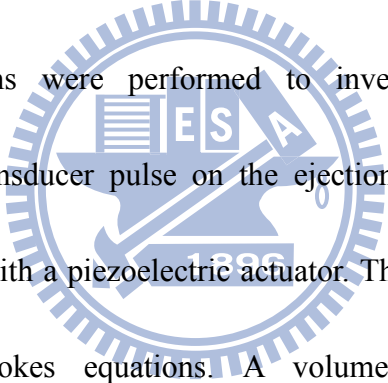liquid hydrophobicity on the drop formation of an ink jet printhead

Student：Jr-Ming Lai   Advisor: Dr. Jenn-Der Lin

Department of Mechanical Engineering

National Chiao Tung University

ABSTRACT

Numerical calculations were performed to investigate the effect of the component of a single transducer pulse on the ejection of a drop for a drop-on-demand ink-jet printhead with a piezoelectric actuator. The flow field is governed by continuity and Navier-Stokes equations. A volume-of-fluid method with a piecewise-linear interface construction is used to track the complicated topological variation of the liquid-gas interface. The computer code was validated with experimental results present in the literature. The volume of the primary drop is closely related to the maximum displacement D_f of chamber wall induced by piezoelectric actuator in the forward stroke; the velocity of the primary drop depends on the ratio of D_f to the time period of the forward stroke, $\Delta\tau_f$. Moreover, the formation of the primary drop depends weakly on the conditions of backward stroke

considered. A decreased interval between forward and backward strokes might serve

to suppress the formation of satellite drops owing to reducing the liquid thread length

l_b at pinching off to a value less than the upper limit l_b^*. The breaking up of freely

flying liquid thread from nozzle outlet has two modes – multiple breaking up and end

pinching, and depends on the thread length at pinching off. In an investigation of the

influence of liquid hydrophobicity and nozzle geometry on the drop formation process,

a system of a nozzle plate connected to a flat-plate piezoelectric material was

designed. The numerical models of the designed system were constructed and

validated by comparing simulation results with experimental observations. The

numerical results show that a decrease in nozzle exit diameter causes a decrease in

drop volume and an increase in drop velocity. When the vibrational amplitude or

frequency of the nozzle plate increases, which raises the input energy, drop volume

appears to decrease and drop velocity to increase. Besides, the linear-type curvature

seems to produce smaller drop volume and larger drop velocity. When the contact

angle varies from 7.1^0 to 170^0, drop volume seems to decrease and drop velocity to

increase.

誌　　　謝

Table of contents

List of tables

List of figures

x

xiv

Nomenclature

A : Maximum displacement of nozzle plate.

a : Ratio of speed of retreating thread tail to capillary speed.

c_1 : Ratio of pinching-off time to capillary time.

c_2 : Ratio of breaking-up time to capillary time.

D : Displacement of nozzle plate.

F : Volume-fraction function.

f : Frequency.

f_σ : Localized volume force.

$\underline{f_\sigma}$: Dimensionless counterpart of localized volume force.

g : Gravitational acceleration.

$\underline{\underline{I}}$: Identity tensor.

$\underline{k}$: Gravitational unit vector.

l_b : Thread length at pinching off.

l^*_b : Critical thread length.

M_2 : Liquid mass.

$\underline{n}$: Unit normal vector.

$\underline{n}_{out}$: Outward normal vector on outlet boundary.

$\underline{n}_{wall}$: Outward normal vector of wall.
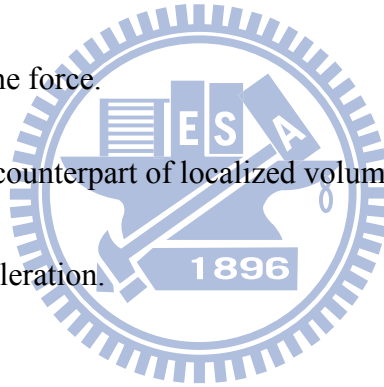
$\bar{p}$: Non-dimensional pressure.

R_{noz} : Nozzle exit radius.

r_d : Drop radius.

t : Time.

$\bar{t}$: Non-dimensional time.

t_{b1} : Pinching-off time.

t_{b2} : Breaking-up time.

t_{ca} : Capillary time.

$\underline{t}_{wall}$: Tangential vector of wall.

U : Capillary speed.

V : Volume.

V_2 : Liquid volume.

z_p : Position of leading edge of liquid thread.

z_t : Position of thread tail tip.

θ_e : Static contact angle.

μ : Fluid viscosity.

μ_e : Effective fluid viscosity.

μ_1 : Air viscosity.

μ_2 : Liquid viscosity.
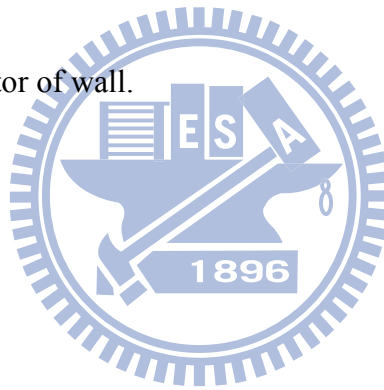
$\underline{v}$: Non-dimensional fluid velocity vector.

v_{ca} : Capillary speed.

v_p : Speed of leading edge of liquid thread.

v_r : Speed of retreating thread tail.

ρ : Fluid density.

ρ_e : Effective fluid density.

ρ_1 : Air density.

ρ_2 : Liquid density.

σ : Surface tension.

σ_{sg} : Solid/gas interfacial force.

σ_{sl} ; Solid/liquid interfacial force.

Chapter 1. Introduction

1.1 Background

In a search for new methods to fabricate oligonucleotide microarrays [1], color filters of liquid-crystal display panels [2], multicolor-polymer light-emitting-diode displays [3] and transistors [4], and to visualize protein distributions [5], attention to ink-jet printing has increased. Ink-jet printheads comprise two main types – continuous ink jets (CIJ) and drop-on-demand (DOD) ink jets. In the CIJ printhead, liquid emerges continuously from a nozzle to form a jet on compressing the chamber ink sufficiently, therefore disintegrating into a train of drops through Rayleigh instability [6, 7]. In contrast, liquid remains still in a DOD printhead nozzle, forming a meniscus unless pressure is applied to overcome the surface tension [8]. Because of its simplicity and the feasibility of a decreased size of the system, the DOD printhead has a major share of the market of ink-jet printers.

The basic configuration of an ink-jet device is in general composed of a chamber with one open end, called a nozzle, from which a liquid jet emanates to disintegrate into drops; the other end is connected to a fluid reservoir that supplies the liquid needed to produce the next drop. Most commercial DOD ink-jet printers use either a thermal or a piezoelectric method as actuation to transform an electric signal into the

motion of a fluid [8]. In the thermal ink-jet device, the expansion of a vapor bubble, induced by an electrically commanded miniature heater, forces the fluid into motion. The piezoelectric ink-jet devices substitute the deformation of an electrically commanded solid sheet instead of a bubble expansion [8, 9]. To actuate the piezoelectric material or the heating element, an excitation signal, typically as a pulse, must be incorporated. The great advantage of the thermal ink-jet device is that it can be produced with a micro electro-mechanical system (MEMS), but its brief lifetime constitutes a great disadvantage [8, 10]. In addition, liquid in the thermal device must be heated and vaporized to form a bubble as a pump. This heating might cause chemical alteration of the properties of the liquid, thereby limiting the applications of this device. The piezoelectric ink-jet device is extensively exploited for its reliability and adaptability in various applications of micro-fluidic control even though the means of production and a high driven-voltage pulse entail great cost. To improve a DOD ink-jet printhead and its applications to fabrications mentioned above, the ejection of drops should be comprehended fully. This ejection behavior involves complicated fluid mechanics involving a competition among viscous, capillary, inertial and contact-line forces. Varied research is reported in the literature.

1.2 Literature survey

2

An experiment to investigate the fluid mechanics of a drop ejection depends mainly on stroboscopic observation. The basic principle of this method is that the region of interest, in which liquid emerges in the form of a jet that subsequently disintegrates into drops, is illuminated with a pulsed light such as a light-emitting diode (LED). The images of the ejected liquid are recorded with a camera incorporating a charge-coupled device (CCD) associated with a microscope. The stroboscope light is generally synchronized with the CCD camera. Many experimenters have visualized the liquid jet and the formation of a drop from DOD ink-jet printheads [11-16]; for instance, Meinhart et al. [14] utilized a particle-image-velocimetry system with micrometer resolution to measure simultaneously the velocity flow field with spatial resolution to 5-10 μm and temporal resolution to 2-5 μs. Fan et al. [12] assessed the drop quality from a temporal sequence of magnified images recorded with a CCD camera and a stroboscopic technique while varying the nozzle size, voltage signal and liquid properties. Kwon et al. [13] developed edge-detection techniques for the jet speed and drop diameter using CCD camera images with a varied trigger interval. Moreover, Dong *et* al. [16] used the stroboscopic photography to capture sequential images of the drop ejection process from a piezoelectric ink-jet printhead. In this study, several key stages of DOD drop formation were identified and quantitative analysis of the dynamics of drop formation

was developed.

The prediction of droplet formation, which can not only validate theoretical models with experimental observation but also provide insight into asymptotic conditions, constitutes a substantial challenge to numerical simulation. Early models failed to predict the temporal evolution of the velocity, shape and trajectory of a drop because models of interfacial physics were inadequate and topology variations were complicated [17-21]. As numerical methods have developed and computing power has advanced, computational fluid dynamics (CFD) has become a promising tool to overcome the limitations of theoretical models. Among diverse approaches, the volume-of-fluid (VOF) method proposed by Hirt and Nichols [22] has proven to be effective for its simplicity and robustness [23-29]. Wu et al. [28] demonstrated the feasibility of the full cycle of ink-jet printing including the ejection, formation and collision of drops against a target substrate with their custom program; employing a finite-difference-based method to solve fluid dynamics and the VOF method to capture the variation of the interface, this program was validated with experimental observation. Liou et al. [25] simulated the ejection of a printhead (SEAJet) by applying commercial CFD software (COMET, StarCD Suite) based on the VOF method to handle free-surface problems. The software discretizes governing equations by means of a finite-volume approach and exploits the continuum-surface-force (CSF) model to

4

account for the effect of surface tension; the predicted evolution of the meniscus inside the printhead was compared with published experimental results. Pan et al. [27] used commercial CFD software (Flow-3D) to simulate the drop formation of a drop ejector with a micro-electro-mechanical diaphragm and provided useful information concerning the design of this ejector; the software was tested to be capable of modeling the free-surface problems, employing the finite-volume approach to solve the governing equations of fluid flow and the VOF method to track effectively the interface deformations. Feng [23] conducted various numerical experiments to find design rules of ink-jet devices utilizing the same software (Flow-3D); the volume, velocity and shape of drops were chosen to evaluate the jet performance. Yang et al. [29] exploited commercial software (CFD-ACE+), also applying the VOF approach for interface tracking to explore numerically the drop ejection of a printhead (Picojet); 17 simulation cases were undertaken to reveal the design concept of the printhead. Anantharamaiah et al. [30] employed the CFD code from Fluent Inc. to investigate the relationship between the nozzle inlet roundness and the diameter of ejected liquid jet in the applications of hydroentangling. The interfacial flow model used in this study was VOF method along with CSF model to consider the surface tension effect. The paper of Anantharamaiah et al. [31] provide extensive discussions of the effect of nozzle geometry on the formation of constricted waterjets, which have an air gap between the

liquid and nozzle wall. In this study, the VOF method together with CSF model was used as the two-phase flow model. Although other numerical methods have been proposed [32, 33], the VOF methods are considered to be commonly used for the modeling of the drop formation in DOD ink-jet printheads.

The full theoretical model of the piezoelectric DOD ink-jet printhead involves the coupling of structural, electric and interfacial flow fields. The direct coupled-field simulation of this printhead might require substantial computing power and cost. An alternative method, so-called load transfer, coupling multiple fields on applying results from one analysis as load in another analysis, might be effective to simulate the multiphysics of a piezoelectric DOD ink-jet printhead. Several authors [19, 28, 29, 33, 34] have shown the feasibility of the load-transfer method to simulate the full system of the piezoelectric printhead. Wu et al. [28] used the propagation theory of acoustic waves before the simulation of interfacial flow of piezoelectric ink-jet printing to estimate the temporal variation of pressure imposed at a location upstream from the nozzle outlet as a boundary condition on pressure. Yu et al. [33] coupled an interfacial flow solver with an equivalent circuit model that transfers the effect of the ink cartridge, supply channel, vibration plate, and piezoelectric actuator into the pressure at the nozzle inflow with a given voltage signal. Kim et al. [34] measured the displacement waveform from a piezoelectric actuator with a laser Doppler vibrometer (LDV); this

waveform information then served as input data at the piston-moving boundary for the three-dimensional simulation of an ink jet. Chen et al. [19] used the finite-element software (ANSYS) to determine the temporally dependent averaged moving velocity of the piezoelectric diaphragm; this velocity was imposed as an inflow boundary condition in a drop ejection simulation of an ink-jet printhead. Yang et al. [29] reported that the transient displacement function of the piezoelectric diaphragm determined (with ANSYS) was imposed as a prescribed moving-boundary condition to investigate the drop ejection of a printhead (Picojet).

In competitive industrial printing markets, a commercially available piezoelectric DOD ink-jet printhead (Picojet) is known for its enduring reliability, diverse fluid compatibility and structural durability. This printhead comprises several stainless-steel plates bonded together to form inner flow channels and cavities with ultrasonic bonding, and uses the bending-mode design of a piezoelectric actuator. As a micro-fluidic dispenser, this printhead is capable of discharging up to 18000 drops per second with a discrepancy of drop volume below 10 %[29, 35].

1.3 Motivation and objectives

As the preceding review illustrates, most previous work has focused on the influence of the diameter of the nozzle exit, the electrically driven signal and the

properties of the dispensed liquid on the drop ejection of ink-jet printheads. The quality of ink-jet printers is closely related by the volume of a primary drop, the creation of an unwanted secondary drop, known as the satellite drop and asymmetric drop formation. The primary drop volume determines the resolution of the printed pattern on a substrate or the quantity of microfluidic deposition; however, the occurrence of the satellite drop would disturb the primary drop charging and degrade the printing resolution by impacting the substrate in undesired locations. The asymmetric drop formation skews the drop trajectory and causes drop misregistration at designated sites, thereby decreasing the accuracy of drop placement. The primary drop volume tends to be affected by the nozzle size and electrically driven signal, and the formation of the satellite drop by the signal waveform and liquid properties. Moreover, the signal waveform and the roundness of nozzle opening seem to have a great effect on the skew phenomena of drop ejection. In most DOD applications, the voltage waveform to drive the piezoelectric actuator is a square-wave pulse or a succession of two square-wave pulses. The effect of the voltage signal on drop ejection has been investigated experimentally and numerically. From an experimental point of view, authors [36, 37] focused mainly on the influence of the maximum amplitude and the frequency of voltage signals on the drop-ejection behavior and on seeking an optimal range of operating conditions in which satellite drops fail to form,

based on an iterative method. Because of machine restrictions, the variable range of operation conditions was constrained. In contrast numerical calculations in research [23, 38] focused on a fundamental understanding of the fluid mechanics of DOD ink-jet printing that in general involves the elucidation of a competition between the flow directed toward the nozzle outlet and that directed away from it, based on a simplified printhead configuration and an ideally imposed flow rate or pressure pulse as a function of time upstream of the nozzle outlet.

Using numerical simulations we have systematically divided a single transducer pulse with a so-called bipolar waveform composed of two square-wave pulses in succession – the first positive and the second negative – into components and investigated the effects of these components and their various combinations on the ejection of a drop in terms of volume, speed and period of decomposition of the primary drop and the formation of satellite drops. According to Rayleigh's pioneering works[6], a liquid jet emanating from a nozzle tends to form drops at some distance from the nozzle due to the instability created by the existence of liquid surface tension. This instability leading to the breakup of the liquid jet and then drop formations originate from the growth of an infinitesimal disturbance along the liquid jet, which reduces the surface area and energy. Following Rayleigh[6], there is the most rapidly growing disturbance which sets the sized drops formed under one excitation of

external noises and reduces the surface area of the liquid jet the most. The environmental disturbances produced at the nozzle and convected down the jet tend to be random. Therefore, the drop formation frequency and the distance from the nozzle where drops first appear alter at random. According to previous researches[6, 7], the formation of drops can be forced to happen at a well-defined frequency and distance from the nozzle by flustering the jet periodically with sufficient power in order that random environmental disturbances are ignorable. One way to perturb the liquid jet periodically is to introduce a periodic pressure change at the liquid side of the nozzle. In the drop formation of a piezoelectric ink jet printhead, the pressure variation in the nozzle can be driven by the electrically controlled solid wall movements. This motivates us to investigate the effect of a transducer pulse on the drop formation and microfluidic control of a piezoelectric ink jet printhead.

The literature review also shows that little is known about the effect of the wetting condition of the nozzle wall and its curvature on drop formation through the ink-jet print heads. Furthermore, when an ink-jet print head is fabricated in progressively smaller size for the purpose of enhancing resolution, the capillary effects including the vapor- liquid interfacial tension and the wetting condition on the solid wall, coupled with curvature of that wall, play an increasingly important role on the drop ejection. In the present work we performed numerical simulations to

investigate the detailed process of formation of a droplet when considering various dynamic contact angles (various dynamic contact-angle patterns represent varied wetting conditions) and curvature of the nozzle wall. To simplify the models stemming from the complicated geometry of the interior flow channels in ink-jet print heads, we adopted a model of a nozzle plate connected with a flat-plate piezoelectric material; we compared the numerical results with experimental measurements to validate the present computer code. The results of this work might yield suggestions for the design of ink-jet printheads and contribute to a fundamental understanding of the fluid mechanics of DOD ink-jet printing.

The rest of the thesis is organized as follows. Chapter 2 describes the theoretical models and computational methods used in this study. Chapter 3 presents computational results and discusses the effect of a transducer pulse on the DOD drop formation. Chapter 4 considers the influence of liquid hydrophobicity and nozzle passage curvature on a drop ejection process. In this chapter, firstly, the physical models and solution methods are described. Secondly, the description of the experimental setup and conditions are given. Next, a comparison of numerical results with experimental observations is presented. Finally, numerical results and a discussion of the effect of the orifice diameter, the curvature of the nozzle passage and wall wetting conditions on the drop ejection are provided. Chapter 5 presents the

conclusions and future work.
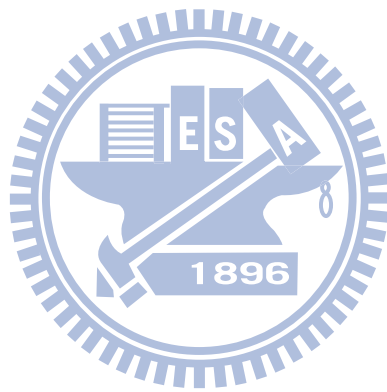
Chapter 2. Theoretical models and computational methods

2.1 Interfacial flow models

We investigated the drop-ejection behaviors of a printhead (Picojet) with the bending-mode design of an piezoelectric actuator [29, 35]. We considered a system with an isothermal, incompressible Newtonian fluid of constant density and constant viscosity. The origin of coordinates is based at the center of the nozzle exit plane and the axial unit vector is directed away from the nozzle. Figure 2.1 shows a schematic of the printhead configuration (Picojet) and its computational domain adopted in our theoretical models. The dimensions of the pressure chamber are length 1.880 mm, width 0.980 mm and height 0.200 mm, and those of the ink-supply channel are 1.440, 0.550 and 0.100 mm, respectively; the diameter of the nozzle outlet is 0.0343 mm. The dynamics of drop formation are accepted to be governed by the continuity and the Navier-Stokes equations subject to appropriate boundary and initial conditions. To distinguish the dependent parameters and variables, we made the governing equations, initial conditions and boundary conditions non-dimensional by using the radius of the orifice, R_{noz} and capillary period, $t_{ca} = (\rho R_{noz}^3 / \sigma)^{1/2}$ in which appear density ρ and surface tension σ, as characteristic length and time. Assuming that the fluid obeys the linear Newtonian friction law and neglecting the compressibility, we rewrite these

equations in these non-dimensional forms.

$$\nabla \cdot \underline{v} = 0 \tag{1}$$

$$\frac{1}{Oh}[\frac{\partial \underline{v}}{\partial t} + \underline{v} \cdot \nabla \underline{v}] = \nabla \cdot [-\bar{p}\underline{I} + \nabla \underline{v} + (\nabla \underline{v})^T] + G\underline{k} \tag{2}$$

in which $\bar{t}$ is time in units of t_{ca}, $\underline{v}$ is the fluid velocity vector in units of

$U = R_{noz}/t_{ca}$, $\bar{p}$ is static pressure in units of $\mu U / R_{noz}$ with μ denoting the

viscosity of the fluid, $\underline{I}$ is the identity tensor, $\underline{k}$ is gravitational unit vector,

$Oh = \mu / \sqrt{\rho R_{noz} \sigma}$ is Ohnesorge number and $G = \rho R_{noz}^2 g / \sigma$ is the Bond number with

g denoting the gravitational acceleration. Except condition of no slip and no

penetration at solid walls, the boundary condition for traction at the free surface must

be satisfied,

$$\underline{n} \cdot [-\bar{p}\underline{I} + \nabla \underline{v} + (\nabla \underline{v})^T] = Oh\underline{n}\nabla \cdot \underline{n} \tag{3}$$

with local unit normal vector $\underline{n}$ at the free surface.

The physical phenomena of drop formation involve a complicated topological

variation of the liquid-air interfacial flow such as the liquid decomposition and

coalescence. A severe problem confronting researchers in numerical analysis is the

mathematical description of the free surface. Possible solutions might arise from

either Lagrangian methods or Eulerian methods; the former configure the mesh to

adapt continuously to the temporally dependent deformation of the liquid-air interface,

whereas the latter employ a fixed mesh through which the arbitrarily shaped interface

moves. Although maintaining the discontinuity of the liquid-air interface with fidelity,

Lagrangian methods have difficulty treating the severe distortion of a mesh allied to

the complicated topological variation of the liquid-air interface. However, the

Lagrangian finite-element (FE) method can satisfactorily predict the development of

microthreads and overturning but not the dynamics near the point of necking and

pinching off [38]. Here, we utilize an interface-capturing method, a variation of the

volume-of-fluid (VOF) scheme and belonging to the Eulerian type, to resolve this

transient behavior of the free surface separating two incompressible and immiscible

fluids in the drop formation [39]. The most characteristic feature of this

interface-capturing method is that the two fluids are considered as one effective fluid

with a scalar variable, F, called the volume-fraction function. Let the properties of air

and liquid be denoted by subscripts 1 and 2, respectively, and let V_2 and M_2 be the

volume and mass of the liquid. V_2 and M_2 are then given as

$$V_2 = \int F dV$$

(4)

$$M_2 = \int F \rho_2 dV$$

(5)

in which ρ_2 represents the liquid density. The total volume V is then

$$V = \sum_{K=1}^{2} V_K$$

(6)

Considering mass conservation and constant fluid properties, we obtain an equation

for the evolution of the volume fraction: [39, 40]

$$\frac{\partial F}{\partial t} + \underline{v} \cdot \nabla F = 0$$

(7)

By definition, the volume-fraction function is a ratio of volume occupied by the liquid in a computational cell to the total cell volume and takes unit value at the liquid side and zero at the air side. The crossing region ($0 < F < 1$) depicts the free surface, of which the position is generally defined to have $F = 0.5$. The critical issue in this method of capturing the free surface is the discretization of the convective term in Eq. (7). We use in particular a multidimensional unsplit advection algorithm with a piecewise construction of a linear interface (PLIC) to make discrete this convective term [39]. In the numerical simulation the surface tension at the free surface is modeled with a localized volume force f_σ in the framework of the continuum surface-force (CSF) model (Brackbill et al., [41]) that is ideally suited for Eulerian interfaces of arbitrary topology:

$$\underline{f}_\sigma = \frac{1}{Oh}[-\nabla \cdot (\frac{\nabla F}{|\nabla F|})]\nabla F$$

(8)

where $\underline{f}_\sigma$ is the dimensionless counterpart of f_σ and the term in brackets describes the mean curvature of the free surface. This localized volume force can then be incorporated into Navier-Stokes equations. Equation (7) must be coupled with Eqs. (1) and (2). Velocity vectors are first updated on solving Eqs. (1) and (2), then substituted into Eq. (7), so to obtain the redistribution of the volume-fraction function. The physical properties of the effective fluid including the density and

viscosity in each computational cell are determined in the following manner:

$$\rho_e = F\rho_2 + (1 - F)\rho_1 \qquad (9)$$

$$\mu_e = \frac{F\rho_2\mu_2 + (1 - F)\rho_1\mu_1}{\rho_e} \qquad (10)$$

For the model considered here, the arrangement of the types of boundary condition is shown in Fig. 2.1(b). We suppose that the boundaries at the solid wall meet the conditions no slip and no penetration. Except above boundary conditions, the problems with free surface flow also require the conditions at the moving contact line to be specified for a variable level of the wettability of the nozzle wall. The contact line is defined as a location at which liquid, gaseous and solid phases meet. In treatment of this wetting condition, we assume that the contact angle, formed by the liquid/gas and liquid/solid interface, equals the static (equilibrium) angle according to Young's equation:

$$\sigma \cos\theta_e = \sigma_{sg} - \sigma_{sl} \qquad (11)$$

where θ_e is the static contact angle and σ, σ_{sg} and σ_{sl} are liquid/gas, solid/gas and solid/liquid interfacial forces respectively; the related dynamic contact angle on the wall regions is hence set constant during the drop formation. The implementation of the boundary condition for the dynamic contact angle is readily incorporated within the framework of the CSF model. Volumetric force $\underline{f}_\sigma$ applied to the numerical cells immediately at the solid walls is calculated with

17

$$\frac{\nabla F}{|\nabla F|} = \underline{n}_{\text{wall}} \cos\theta_{\text{e}} + \underline{t}_{\text{wall}} \sin\theta_{\text{e}} \qquad\qquad (12)$$

where $\underline{n}_{wall}$ and $\underline{t}_{wall}$ represent outward normal and tangential vectors for the wall, respectively. In the present study, the contact angle θ_e is set to be 7.1^o for the system of water on the plate nickel nozzle wall, according to Yang et al. [29]. For the outlet boundaries, the pressure conditions are set to be 1 bar.

2.2 Modeling of a transducer pulse

The full theoretical model of the piezoelectric DOD ink-jet printhead involves the coupling of structural, electric and interfacial flow fields. The direct coupled-field simulation of this printhead might require substantial computing power and cost. To circumvent the inherent difficulties of this coupled-field simulation, we utilized a temporally dependent function of the wall displacement with a trapezoidal shape and ignored vibration ripples of higher order to model the temporal variation of a deformable diaphragm caused by the bending effect of the piezoelectric material, as shown in Fig. 2.2(a). The piezoelectric material deflects outward in the period $\Delta\tau_s$ and stays fixed in $\Delta\tau_{p1}$, enlarging the pressure chamber and causing liquid to fill it. In the periods $\Delta\tau_f$ and $\Delta\tau_{p2}$, the piezoelectric material in this so-called forward and pause stages moves inward and keeps still to decrease the chamber volume and cause the liquid to be ejected from the nozzle outlet. In the periods $\Delta\tau_b$ and $\Delta\tau_{p3}$,

the piezoelectric material resumes its equilibrium state thus producing a negative

pressure (suction) to facilitate the pinch-off of liquid thread. In the rest of this article,

we denote supply stage $\Delta\tau_s$, refill stage $\Delta\tau_{p1}$, forward stage $\Delta\tau_f$, pause stage

$\Delta\tau_{p2}$, backward stage $\Delta\tau_b$ and equilibrium stage $\Delta\tau_{p3}$. Figure 2.2(b) shows the

temporal variation of the basic voltage signal applied to the PZT actuator of a

printhead (Picojet) and the wall displacement related to the equilibrium state at the

centroid of the chamber wall adjacent to the piezoelectric material. Here, the

dimensions of the PZT actuator with rectangular shape are length 1.24 mm, width

0.98 mm and height 0.2 mm. This momentary displacement function was determined

by the stress module of the commercial code (CFD-ACE+) based on the finite

element numerical method. According to our theoretical models, the drop formation

can be driven by a pressure, velocity or piston moving as a condition at the boundary.

Among them, an application of the moving boundary involves the instantaneous

remeshing of the interior grids of the solution domains of which the boundaries are

moving and thus increases the computational cost. We therefore assumed that drop

ejection is driven by the boundary condition of specified velocity that is obtained on

differentiation of the temporally dependent function of the diaphragm displacement

shown in Fig. 2.2(a). Moreover, the axial deformation of the diaphragm is of order 10

nm, much less than the thickness of the ink chamber, 200 μm. We here neglect the

effect of the deformation of the diaphragm adjacent to chamber wall. The rate Q of

chamber volume displacement arising from the temporal variation of the deformable

diaphragm can be tied with the Weber number, $We \equiv \rho Q^2 / \pi^2 \sigma R_{noz}^3$, which depicts the

ratio of inertial to surface tension force [38]. It is noted that the Weber number can be

different in various stages; in the following, except refill, pause and equilibrium

stages in which the corresponding Weber number is vanished, we denote the Weber

number in supply stage We_s, forward stage We_f and backward stage We_b.

Therefore, in the present study, the temporally dependent function of the diaphragm

displacement can be represented as the independent parameters: D_s, We_s, $\Delta\tau_{p1}$,

D_f, We_f, $\Delta\tau_{p2}$, D_b, We_b and $\Delta\tau_{p3}$ for the waveform in Fig. 2.2(a).
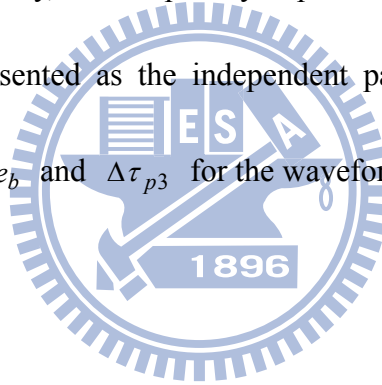
2.3 Computational methods

To validate the present theoretical models, we performed all computations with

multipurpose commercial code (CFD-ACE+) based on the finite-volume numerical

method to solve the three-dimensional Navier-Stokes equations and the iterative

semi-implicit method for pressure-linked equations consistent (SIMPLEC) with

velocity-pressure coupling. Convective and diffusive fluxes are approximated by

central difference scheme. Here, the explicitly first-order backward Euler scheme

served for discretization of time. The primary variables are the velocity, pressure and

20

volume fraction, which cannot be determined until convergent criteria are satisfied for each time step. A flow chart of the principal algorithmic steps is shown in Fig. 2.3. Due to the use of the multidimensional unsplit advection algorithm, which is a geometrically-based flux calculation procedure for the evolution of volume-fraction function, an inherent stability requirement on the size of time step must be considered. To reduce simulation time without losing stability, the size of the next time step is calculated before each new time step. The time step is computed from a fixed value of the Courant number (Co) and the changeable local velocity in the interface cells and their immediate neighbors (0<F<1). Corresponding to the maximum velocity $v_{i,\max}$ found in the grid cells of interest, the minimum value of the time step is calculated and implemented using the following relationship:

$$\Delta t_{new} = Co \frac{\Delta x_{\min}}{v_{i,\max}} ,$$
(13)

where $\triangle t_{new}$ is the time step calculated and $\triangle x_{\min}$ is the length scale of the smallest grid cells of interest. The Co number is utilized to restrict the crossing of interface to certain amount of a cell width during each time step. In the current study, the value of the Courant number is set as low as 0.05 to ensure that the free surface crosses less than a cell during the time step. Therefore, the actual local Courant number is less than or equal to 0.05. In an early stage of this study, test cases with Co=0.05 and 0.02 were also performed. The influence of the finer time step size on the transient

behavior of drop ejection is insignificant. Considering most applications of ink-jet printing, we use a fluid of density 1000 kg m^{-3}, viscosity 3.5 cp and surface tension 0.0725 N m^{-1} at which Ohnesorge number equals the value 0.1. In addition, based on the preliminary simulations, we choose the values of $D_s = 0.03 \mu m$, $\Delta \tau_s = 3 \mu s$, $\Delta \tau_{p1} = 9 \mu s$, $D_f = 0.06 \mu m$, $\Delta \tau_f = 3 \mu s$, $\Delta \tau_{p2} = 3.5 \mu s$, $D_b = 0.03 \mu m$ and $\Delta \tau_b = 3 \mu s$ as the reference conditions of the transducer pulse in the remainder of this study unless they are indicated otherwise. Here, the value of $\Delta \tau_{p3}$ is adjusted to ensure that the flow in the printhead is gradually stopped with the initial condition reload for the next drop ejection.

(a)

(b)
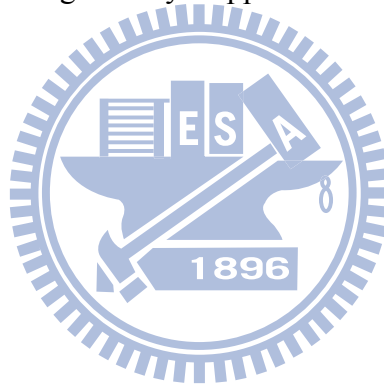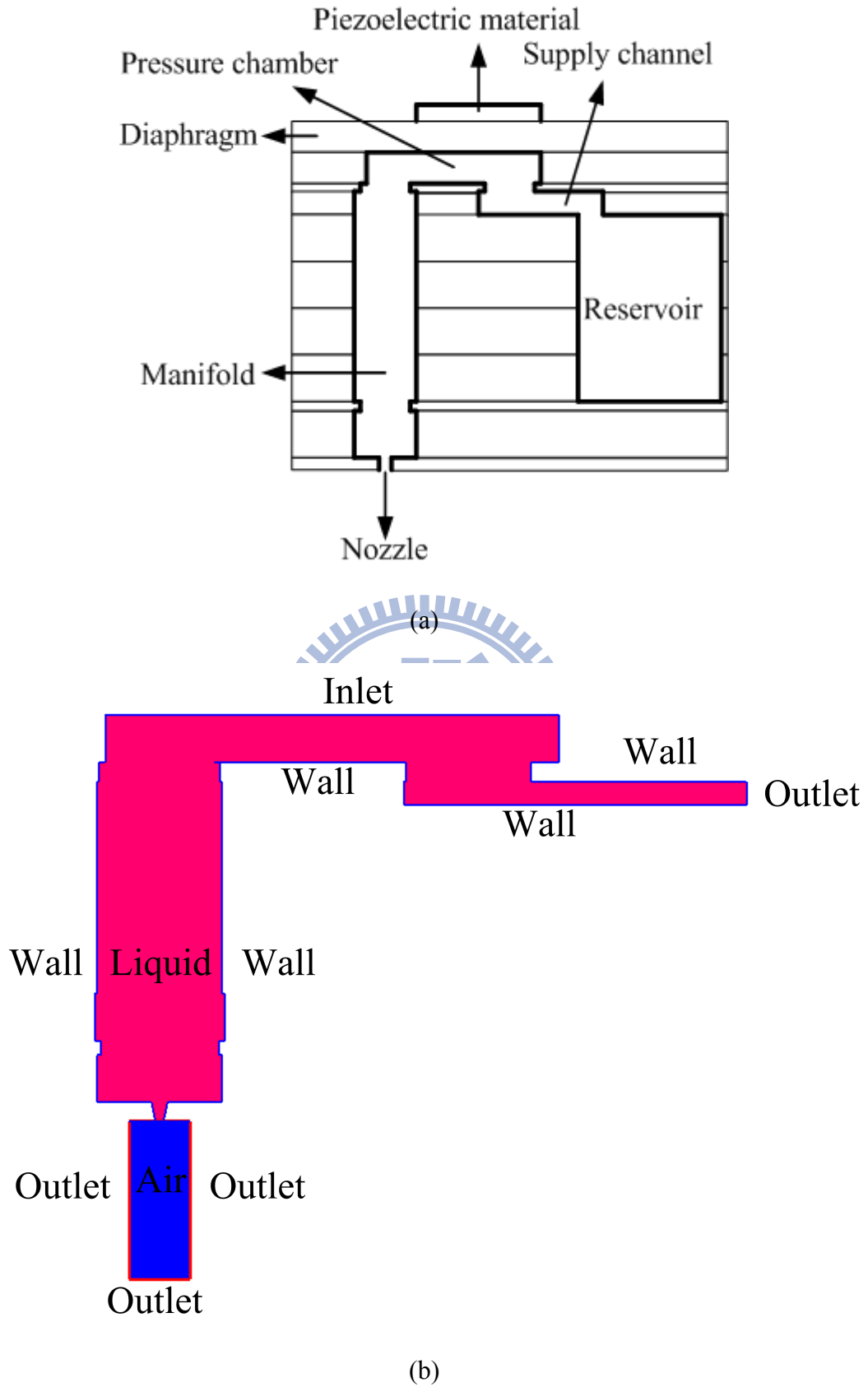
Figure 2.1. (a) Schematic of printhead (Picojet) and (b) its computational domain.
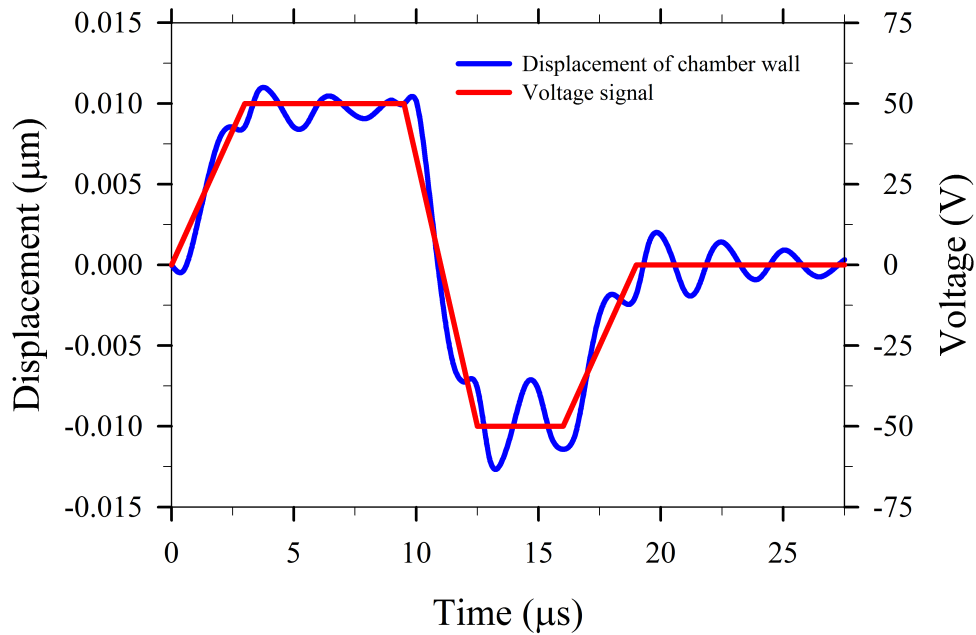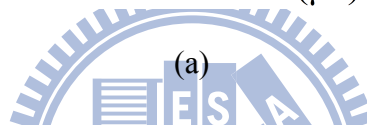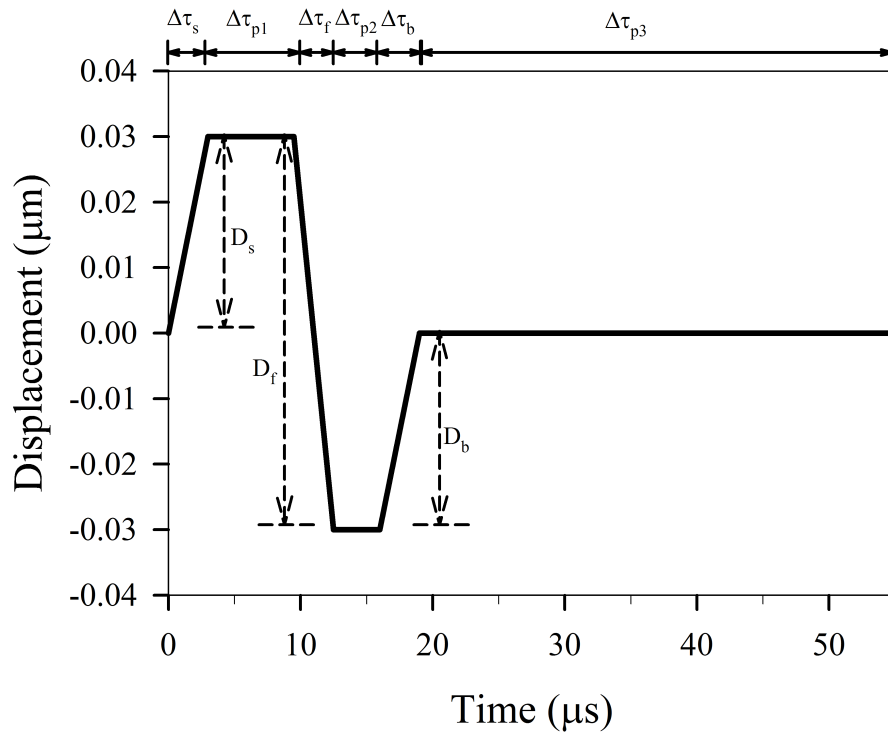
Figure 2.2.   (a) Temporally dependent function of wall displacement and (b) temporal profile of the voltage signal and displacement of the wall beside the piezoelectric transducer.
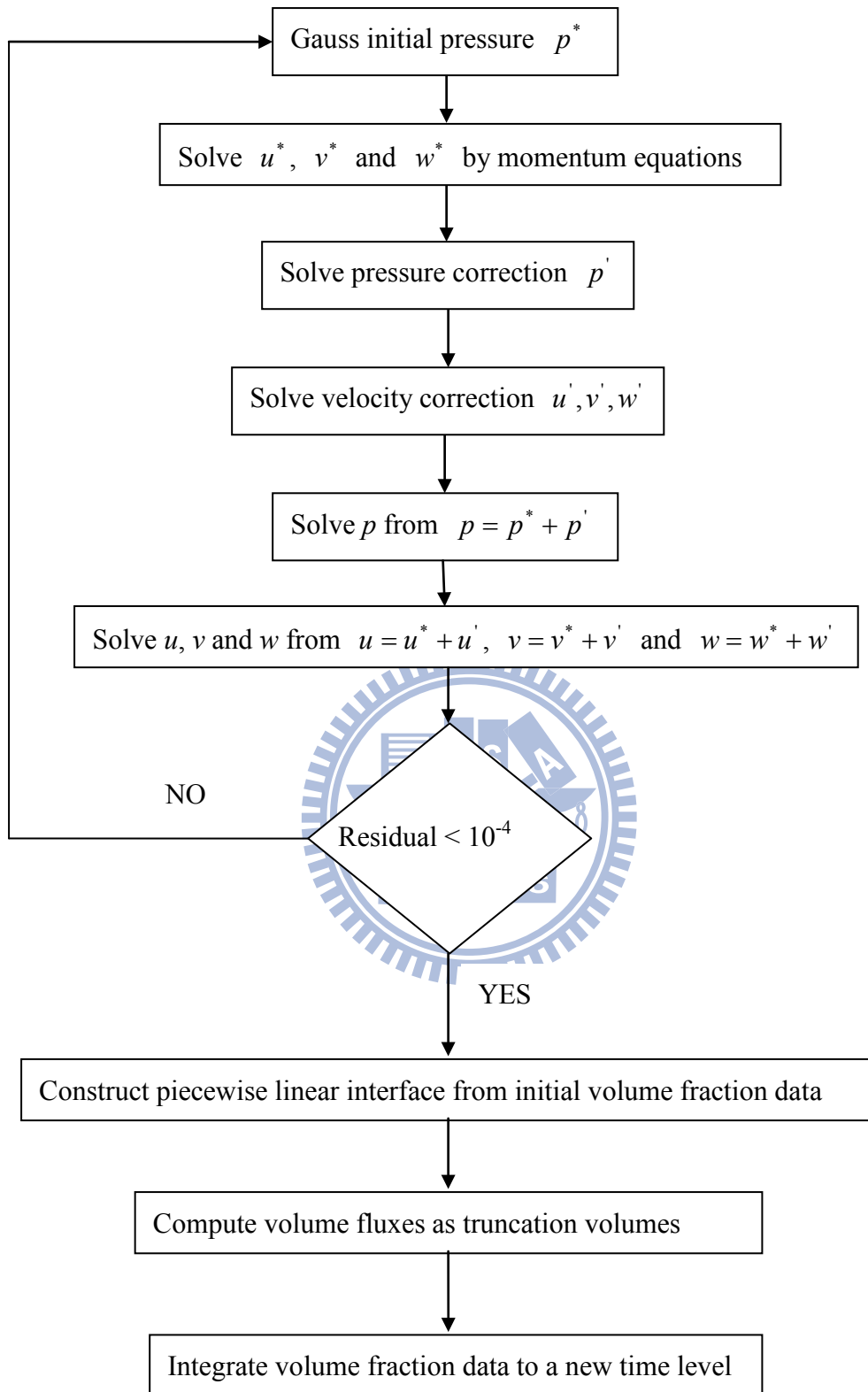
Figure 2.3. Flow chart of the principal algorithmic steps.

Gauss initial pressure p^*

Solve u^*, v^* and w^* by momentum equations

Solve pressure correction p'

Solve velocity correction u', v', w'

Solve p from $p = p^* + p'$

Solve u, v and w from $u = u^* + u'$, $v = v^* + v'$ and $w = w^* + w'$

Residual $< 10^{-4}$

NO

YES

Construct piecewise linear interface from initial volume fraction data

Compute volume fluxes as truncation volumes

Integrate volume fraction data to a new time level

Chapter 3. Simulation results and discussion

3.1 Grid convergence and model validation

The numerical grids of the printhead to simulate drop ejection are illustrated in

Fig. 3.1. The computational domain is divided into five parts – the ink-supply channel,

the ink chamber, the manifold, the nozzle and the area outside the nozzle. To achieve

a uniform distribution of the discretization errors, we utilized non-uniform grids that

adopt a small grid spacing in regions such as near the nozzle, the immediate solid

walls and the trajectory of the flight drops of which the derivatives of the variables

alter radically and large discretization errors are expected. All numerical grids are

three-dimensional hexagons with smallest spacing 1.5 μm, which corresponds to the

criterion that, according to the VOF method, at least 4-5 cells are required across the

gap to provide an adequate resolution of the free surface in that gap [39, 40].

To test the grid dependence, we devised grids of total numbers 186898, 282408

and 411654 cells adding 10 per cent of the total grid points in each dimension. Table 1,

2 and 3 show the time at which the liquid thread pinches off from the nozzle outlet,

the drop tip position and velocity of the drop head defined as a estimated velocity at

the leading edge of the drop, as well as the volume of the primary drop using varied

meshes. In the present study, the shape of the primary drop after the oscillation of the

surface wave is sufficiently decayed by viscous dissipation could be approximated to a sphere whose diameter is determined by measuring the maximum end-to-end distance of the liquid drop and could be used to estimate the drop volume. It is shown that the pinch-off times obtained with these three meshes are in excellent agreement. Table 2 shows the difference in drop tip position where the velocity of drop head is estimated decreases with grid refinement. It is seen that the discretization error in drop tip position is around 0.43 % when refining from 282408 cells to 411654 cells, whereas that 1.04 % when refining from 186898 cells to 282408 cells. In addition, Table 2 also presents that the discretization error in the estimated velocity of the drop head is around 2.28 % between 282408 cells and 411654 cells, and that around 3.78 % between 186898 cells and 282408 cells. Table 3 makes clear that the difference in primary drop volume decreases with grid refinement. The computed error in drop volume at 40 μs when the shape of the primary drop could be approximated to a sphere between 282408 cells and 411654 cells is around 1.49 %, and that between 186898 cells and 282408 cells is around 6.11 %. The net volumes of fluid expelling from nozzle outlet over the total time period of simulation are 19.9982 pL on 186898 grids, 19.5928 pL on 282408 grids, and 19.6372 pL on 411654 grids. The difference in this net volume of fluid between 282408 cells and 411654 cells is 0.226 % and that between 186898 cells and 282408 cells 2.07 %. Therefore, Grid independence is

satisfied with a mesh of 282408 cells achieving a compromise between accuracy and

computing time which in this paper is around 96 h of central processing unit (CPU)

time. As also illustrated in existing literature[42], it is worthy to point out that when the

primary drop moves downstream behind certain simulation field, it does not conserve

mass well. This may be due to the numerical grids with larger spacing arranged in this

field, and/or the linear order of the multidimensional unsplit advection algorithm with

PLIC. The most effective remedy may be a careful attention to higher order schemes

and sufficient grid resolutions.

Figure 3.2 shows a comparison of the predictions with experimental observations

of Yang et al. [29] of the temporal evolution of the position of the leading edge of the

liquid drop. In this case, we used water as a working fluid whose density, viscosity

and surface tension are 1000 kg m^{-3}, 1.0 cp and 0.0725 N m^{-1}, respectively. The

corresponding parameters of the transducer pulse were set to be $D_s = 0.029 \mu m$,

$\Delta \tau_s = 3 \mu s$, $\Delta \tau_{p1} = 6.5 \mu s$, $D_f = 0.058 \mu m$, $\Delta \tau_f = 3 \mu s$, $\Delta \tau_{p2} = 3.5 \mu s$, $D_b = 0.029 \mu m$

and $\Delta \tau_b = 3 \mu s$. In addition, we excluded the first drop ejection from data analysis

owing to an unbalanced liquid meniscus at the nozzle exit plane. Restricted to the

limit of experimental setup configured by Yang et al.[29], the drop tip position was

measured every five microsecond after the liquid thread emerged from nozzle outlet.

This temporal resolution is insufficiently to determine the evolution of ejected liquid

during different stages of a piezoelectric actuator. However, based on the results

shown in Fig. 3.2, the numerical models predict the same trend as the experimental

observation, and a reasonable agreement is obtained between the experiment and

simulation. In addition, the comparison between the predictions and visualized images

of evolution of ejected drop could be found in research of Yang et al.[29], which used

the theoretical models and arrangements of numerical grids similar to the current

study.

3.2 Forward stage

According to research of Dong et al. [16], a typical DOD drop formation is

divisible typically into five stages – ejection, stretching, pinching off, recoil and

breaking up. Figure 3.3 shows these key stages observed in our numerical simulations.

In the ejection stage, the liquid meniscus initially protrudes from the nozzle orifice

and then quickly extends outward due to the forward stroke of the piezoelectric

actuator [Fig. 3.3(a)]. As the forward actuation ends, the rate of liquid flow toward the

plane of the nozzle exit rapidly decreases during the period $\Delta \tau_{p2}$; then some liquid is

even sucked back into the nozzle under the effect of the backward actuator. A

decreased rate of liquid flow toward the nozzle outlet would cause the difference in

axial velocity between the head of the liquid column and liquid near the plane of the

nozzle exit. This velocity inequality accounts further for the stretching of the liquid column, as shown in Fig. 3.3(b). In addition, two necking points are observable during the stretching stage, first near the nozzle orifice and second near the bulbous head of liquid thread, as shown in Fig. 3.3(c). After a short interval, the tail of liquid thread pinches off from the nozzle outlet to form a freely flying liquid thread [Fig. 3.3(d)]. The tail and the leading edge of the freely flying liquid thread are asymmetric and thus behave differently. Because the pressure at pinching off is large, the tail of the free liquid thread begins to recoil toward the thread head and gradually evolves into a bulbous shape, as shown in Fig. 3.3(e). During the recoil stage, the second necking point continues to develop until the freely flying liquid thread breaks into two parts – a primary drop and a secondary freely flying liquid thread with asymmetric ends. Because the secondary freely flying liquid thread retracts to decrease the surface energy, a satellite drop might be formed [Fig. 3.3(f)]. This DOD drop formation with one satellite drop formed by end pinching might be found in most current simulations. In addition, two specific times could be observed in the drop formation process described above: pinching-off time when the ejected liquid thread detaches from the remaining liquid in the nozzle and breaking-up time when the primary drop is formed.

To investigate the effect of D_f, $\Delta\tau_f$ and We_f on drop ejection, we conducted seven numerical experiments, as shown in Table 4. It is noticed that not all

waveforms designed may assure the actuator of returning to the original position after the backward strokes are applied. That is because to systematically examine the effects of components of a transducer pulse, all parameters are fixed except the one of interest in a numerical experiment. The disruptions of the fluid interface failed to occur in experiment 2, whereas experiment 1 with D_f increased to 0.06 μm and experiment 3 with $\Delta\tau_f$ decreased to 1.5 μs produced a pinching off of the liquid thread. It would appear that the ratio of D_f to $\Delta\tau_f$ must exceed a minimum value for a successful drop ejection. The value of $D_f/\Delta\tau_f$ multiplied by the area of the chamber wall adjacent to the piezoelectric material represents the rate of chamber volume displacement and could be related to the Weber number (inertial/surface tension force). For experiments 1, 2 and 3, Fig. 3.4 shows the evolution of the liquid thread shape and velocity vector in the liquid side. On the effect of the backward stroke of actuation, the flow near the plane of the nozzle exit is reversed, which causes the formation of a stagnation plane sweeping toward the head of liquid thread. Figure 3.4(a) shows that, under the conditions of experiment 2, the stagnation plane sweeps through the entire liquid thread and the thread fails to pinch off. Experiments 1 and 3, in contrast, show that the stagnation plane does not sweep to the liquid thread tip and the effect of the reversed flow causes necking near the nozzle and then the pinching off of the liquid thread, as shown in Fig. 3.4(b) and Fig. 3.4(c).

31

Figure 3.5(a) shows the variation of the volume of the primary drop in these conditions. The drop volume in experiment 1 equals approximately that in experiment 5, and the drop volume in experiment 3 that in experiment 6; the drop volume in experiment 4 is near that in experiment 7. The drop volume falls into three zones that correspond to three distinguishable values of D_f. Figure 3.5(b) shows the variation of the velocity of the center of mass of the primary drop upon breaking up in these cases. The velocity of the primary drop increases substantially as We_f is increased, which corresponds to an increased inertial force. Experiments 1, 3 and 4 show that the drop velocity correlates positively with the primary drop volume; a similar relation is seen at different value of We_f, as shown in experiments 5 and 6 in agreement with the results of Feng [23]. This is because that the large amount of ejected liquid decreases the restoring effect of surface tension due to the smaller curvature of the fluid interface. Figure 3.6 shows the temporal variation of the rate of volume flow at the plane of the nozzle entrance. The total volume entering the nozzle during the forward stroke of the actuation in experiment 3 and representing the area underneath the line in Fig. 3.6(a) is 15.268 pL, whereas that in experiment 6 is 19.725 pL. Figure 3.6(b) shows that the total volume entering the nozzle during the forward actuation in experiment 7 is greater than that in experiment 4. These results indicate that through conservation of mass the total volume ejected from the nozzle increases when the

value of We_f increases and that of D_f remains constant. The variation with experiments of duration of the liquid thread pinching off from the nozzle outlet is shown in Fig. 3.7. The period for pinching off in experiment 3 is less than that in experiments 1 and 4. The period to pinch off seems to increase as D_f increases with We_f remaining constant; a possible explanation is that the large amount of ejected liquid corresponding to a large value of D_f decreases the effect of driving the breaking of surface tension by the small curvature of the fluid interface. As mentioned above, however, the large ejected volume of liquid might weaken the restoring effect of surface tension and then has a large forward momentum density, which facilitates the pinching off of liquid thread with a rapid elongation and necking, as shown in Fig. 3.5(b). When We_f has a large value, the forward momentum density because of increased volume of ejected liquid increases greatly, as shown in Fig. 3.5(b). The period to pinch off in experiment 5 is less than that in experiment 6 as the driving effect on pinching off through the increasing forward momentum density induced by increasing D_f is dominant, as shown in Fig. 3.7. Figure 3.7 also shows that the period for pinching off of the liquid thread in experiment 5 is less than that experiment 1. When We_f increases, the forward momentum density possibly increases, which accelerates the pinch-off of liquid thread by rapid elongation and necking, shown in Fig. 3.5(b). A similar relation is found between experiments 3 and

6. However, Fig. 3.6 shows that, when the value of We_f increases, the ejected liquid volume increases, thus decreasing the effect of the driving of the breaking of surface tension and then decelerating the thread pinching off. Figure 3.7 shows that the period for pinching off in experiment 7 is greater than that in experiment 4 because the driving of the pinching off is contained by the increased volume of ejected liquid when We_f in experiment 7 is greater than that in experiment 4.

3.3 Backward stage

Table 5 shows the variation of the conditions of the backward stroke in five numerical experiments for the investigation of the effect of D_b $\Delta\tau_b$ and We_b on the drop ejection. Figure 3.8 shows the variation of the volume of the primary drop and the velocity of the center of mass of the primary drop upon breaking up in these experiments; the drop volumes are approximately constant in all cases. Moreover, the estimated values of the drop velocity in all experimental conditions fall into the same range. The backward inertial force in all these cases might be insufficient to draw all ejected liquid back and the meniscus would invade the tube through conservation of mass. Figure 3.9 shows the evolution of the shape of the liquid thread during the period of the backward stroke in the various experiments. The temporal variation of the tip position of the liquid thread for these cases is almost constant, and the contours

of the liquid interface are similar except near the plane of the nozzle exit. Under the

effect of the reversed flow caused by the backward actuation, the liquid interface near

the plane of the nozzle exit tends to be drawn back, and the mean curvature of the

interface is negative and becomes smaller and smaller (liquid surface near the nozzle

exit is concave). Here, we assume that the principal curvature on the free surface is

positive if the center of the circle of curvature lies on the liquid side. According to Eq.

(8), the smaller the mean curvature at a point on the free surface, the larger the

localized volume force induced by surface tension effect. After the period of the

backward actuation terminates, the liquid in the nozzle would thus be pulled out again

through the effect of the imbalance of surface tension and the inertia of the liquid in

the ink-supply channel. The extent of tube invasion by the retracting meniscus and the

acceleration of the thinning of the fluid neck increase as We_b increases [see Fig. 3.9,

18.5 and 19.5 μs]. Experiment 8, in which the condition of the backward actuation has

the same value of We_b as in experiment 9 but a large working interval, $\Delta\tau_b$, shows

a greater extent of tube invasion and a smaller curvature of the liquid interface, thus

causing a larger rate of volume flow of the liquid toward the nozzle outlet. Figure

3.10 shows the temporal variation of the rate of volume flow at the plane of the nozzle

entrance. At the end of the backward stroke, the rate of volume flow at the plane of

the nozzle entrance is directed toward the nozzle outlet and turns gradually into a still

state. As mentioned above, experiment 8 has the rate of volume flow much less than experiment 9 because of the small curvature of the retracting meniscus. Experiment 11 is analogously expected to have a lesser rate of volume flow than experiment 10, as shown in Fig. 3.10. Figure 3.11 shows the variation with experiments of duration of the liquid thread pinching off from the nozzle exit. Experiment 11 seems to have the smallest interval of pinching off. The backward actuation of experiment 11 might proceed through a considerable period in which pinching off of the liquid thread occurs before the rate of volume flow of the liquid toward the nozzle outlet begins because the surface tension is unbalanced. Experiment 8 appears to have large duration of pinching off because the large rate of volume flow toward the nozzle outlet occurs behind the period of the backward stroke, as shown in Fig. 3.10, therefore decelerating the thinning of the fluid neck and prolonging the pinching off. Distinct values of We_b cause varied acceleration of the thinning of the fluid neck, which facilitates the thread pinching off. Various intervals $\Delta\tau_b$ of backward stroke along with various values of We_b may cause varied extent of tube invasion, which obstructs the thread pinching off by inducing the rate of volume flow toward the nozzle outlet beyond the period of backward actuation. Experiments 1, 9 and 10 with different combinations of We_b and $\Delta\tau_b$ lead to the same duration of the thread pinching off, as shown in Fig. 3.11.

3.4 Pause stage

In an investigation of the effect of $\Delta\tau_{p2}$ on the ejection of a drop, Table 6 summarizes nine numerical experiments with various values of $\Delta\tau_{p2}$. Figures 3.12 and 3.13 show the temporal evolution of the shape of the liquid thread near the point of pinching off for experiments 1, 12, 8 and 15 respectively. After pinching off of the liquid thread occurs, experiment 12 shows that the tail of the freely flying liquid thread recoils toward the thread head whereas experiment 1 shows one satellite drop to be formed by end pinching. Both experiments 8 and 15 show one satellite drop to be formed, but, in the case of experiment 15, the satellite drop flies with a larger velocity than that of the former primary drop; the satellite drop might overtake and then merge with the primary drop. Among cases considered here, in experiments 12, 13, 16 and 17 there occurs no satellite drop. These results indicate that a decrease in $\Delta\tau_{p2}$ can damp the formation of the satellite drop; further investigations are described in the next section.

Figure 3.14 shows the variation of the volume of the primary drop and the velocity of the center of mass of the primary drop upon breaking up in considered experiments. The volume of the drop is approximately constant in all cases except experiments 12, 13, 16 and 17 with slightly larger drops. Moreover, other than experiments 12, 13, 16 and 17 with slightly larger drop velocities, all experiments

show nearly the same estimated velocity. The tail of the free liquid thread might tend

to recoil toward the thread head, thus causing an increased volume and velocity of the

drop in agreement with the experimental results of Dong et al.[16] Figure 3.15 shows the

variation with experiments of duration of the liquid thread pinching off from the

nozzle exit. This duration decreases with decreasing $\Delta\tau_{p2}$. For a decreasing period in

which the flow rate toward nozzle outlet is reversed, the necking and then pinching

off of the liquid thread from the nozzle outlet occurs early. Figure 3.16 shows the

temporal evolution of the free surface contour of the liquid thread crossing the period

of actuation of the backward stroke for experiments 1, 12 and 13. Compared to

experiment 1, experiments 12 and 13 show an early necking of the liquid thread,

because of the decreased pause stage. The temporal variation of the position of the

thread head for these experiments is almost constant, as shown in Fig. 3.16.

3.5 Suppression of satellite drops

    The breaking up of freely flying liquid thread has two modes – multiple breaking

up because of wave-like instability and end pinching where the liquid thread pinches

off from a bulbous end[16, 43]. The mechanism of end pinching may be a consequence of

the fluid motion induced by capillary pressure gradients near the end of liquid thread[43].

The two modes of the breaking up of free liquid thread could be observed in the

present simulations. The examples of end pinching and multiple breaking up are found in Fig. 3.3 and Fig. 3.17 respectively. During multiple breaking up, a wave-like disturbance appears along the freely flying liquid thread. This disturbance grows until the liquid thread breaks up at several places and varied times. The liquid thread in multiple breaking up tends to form numerous satellite drops of varied size.

The breaking up of the freely flying liquid thread is related closely to the length of the liquid thread at pinching off, which is defined as the distance between the leading-edge position and tail tip position of the thread. In their DOD dispensing experiments Dong et al. [16] observed that, for the freely flying water thread of small length at pinching off, the formation of a satellite results from end pinching and for a long thread a wave-like instability occurs and multiple breaking up is dominant. Figure 3.18 shows the variation with cases of liquid thread length at pinching off in the current simulations. For a ratio of thread length to nozzle radius (17.15 μm) greater than about 9.67, multiple breaking up occurs through a wave-like instability. When this ratio is smaller than 8.8, the breaking up becomes an end-pinching mode, as shown in Fig. 3.18(a). In addition, the longer the length of liquid thread, the more satellite drops are formed. Experiment 5, for example, shows five satellite drops, experiment 6 three satellite drops and experiment 7 two satellite drops. The thread length at pinching off is positively correlated with the value of We_f. With the same

value of We_f, an increased D_f might yield an increased length of thread at pinching off. The causes of these phenomena might be that, when We_f increases, the forward momentum density increases, thus accounting for an increasing difference in axial velocity and then a more elongated thread. When We_f is constant, the larger D_f implies a larger forward momentum density and then greater elongation of the thread. A decreased $\Delta\tau_{p2}$ could slightly shorten the liquid thread length at pinching off by accelerating the rate of necking, shown in Fig. 3.18(b).

To investigate further the effect of actuation conditions on the thread length at pinching off, we performed additional experiments, as illustrated in Table 7. Figure 3.19 shows the variation in liquid thread length at pinching off for these experiments. The values of l_b / R_{noz} in these cases are all above 9.67; the multiple breaking-up mode is then dominant. These results indicate that the varying parameters in the pause and backward stages cause a slight variation of thread length at pinching off. From the discussion above, we conclude that the thread length at pinching off from the nozzle outlet is governed mainly by the conditions of the forward stroke – D_f and We_f.

In most applications, the satellite drops would degrade the printing quality or increase the difficulty of a precise microfludic control; for this reason a suppression of satellite drops has considerable practical significance. As noted above, the breaking-up mode of the freely flying liquid thread and its thread length at pinching

40

off have been shown to be mutually positively correlated. In the end-pinching mode, the formation of a satellite drop seems to be predictable and its size is comparable. Several authors [16, 44-46] have suggested criteria to observe satellite formation by end pinching; for instance, the numerical research done by Notz and Basaran [45] shows that the liquid thread with sufficiently large initial aspect ratio defined as the ratio of a half thread length to thread radius pinched off daughter drops from almost spherical ends by end pinching when $Oh < O(0.1)$. In this study, the shape of the liquid thread was assumed to be a cylinder with hemispherical caps at its two ends. In contrast, satellite drops caused by multiple breaking up tend to occur arbitrarily and have varied size.

To investigate the suppression of satellite drops, we focus our attention on the end-pinching breaking up of the freely flying liquid thread into the primary drop and the free secondary liquid thread. This secondary thread contracts into a single satellite drop. In the following analysis based on work of Dong et al. [16], we denote the pinching-off time as t_{b1}, the breaking-up time t_{b2}, the thread length at pinching off l_b, the position z_t of the tail tip of the thread, the position z_p, of the leading edge of the thread, the average speed $v_r = dz_t/dt\|_{t_{b2} \to t_{b1}}$ of the retreating thread tail and average speed $v_p = dz_p/dt\|_{t_{b2} \to t_{b1}}$ of the leading edge of the thread, as indicated schematically in Fig. 3.20. The freely flying liquid thread would contract into a single drop without satellite formation provided that the thread length at pinching off from

the nozzle is less than a critical value l_b^*. If we denote the radius of this final single

drop as r_d,

$$l_b - 2r_d \leq (t_{b2} - t_{b1})(v_r - v_p).$$

(14)

Scaling the period with the capillary time and the velocity with the capillary speed,

we obtain

$$t_{b1} = c_1 t_{ca},$$

(15)

$$t_{b2} = c_2 t_{ca},$$

(16)

$$v_r = a v_{ca},$$

(17)

in which c_1, c_2 and a are parameters, $t_{ca} = (\rho R_{noz}^3 / \sigma)^{1/2}$ is the capillary

duration and $v_{ca} = (\sigma / \rho R_{noz})^{1/2}$ is the capillary speed. By definition, c_1 is the ratio

of pinching-off time t_{b1} to the capillary duration, c_2 the ratio of breaking-up time

to the capillary duration and a the ratio of retreating velocity to the capillary speed. In

the present study, the time scale is $t_{ca} \approx 8.341$ μs and velocity scale $v_{ca} \approx 2.056$ m

s^{-1}. Substituting Eqs. (15), (16) and (17) into Eq. (14), we rewrite the equation as

$$l_b - 2r_d \leq (c_2 - c_1)t_{ca} v_{ca} a(1 - \frac{v_p}{v_r}).$$

(18)

Replacing r_d with the radius of nozzle orifice and assuming that $v_r > v_p$, we

rearrange Eq. (18) as

$$\frac{l_b}{R_{noz}} < (c_2 - c_1)a + 2 \equiv \frac{l_b^*}{R_{noz}}.$$

(19)

Table 8 presents this prediction in our simulations. Except for experiment 15, l_b / R_{noz} is larger than the critical value l_b^* / R_{noz}; then one satellite drop can be observed. Notice that although the value l_b / R_{noz} in experiment 15 is less than the critical value l_b^* / R_{noz}, the prediction in this case shows one satellite formed; however, the life time of this satellite is quite short compared to experiment 8, as shown in Fig. 3.13. One explanation for this is that in order to highlight the significant variables of the critical value l_b^* / R_{noz}, we approximate the radius of the final single drop r_d as nozzle radius and neglect the term v_p / v_r in Eq. (18), which would slightly enlarge the upper limits l_b^* / R_{noz}. It can be seen in Table 8 that the ratio of the radius r_p of the primary drop followed by one satellite to nozzle radius (17.15 μm) in experiment 15 is approximately 0.746, which can be expected to be slightly smaller than r_d / R_{noz}. From Eq. (19), the critical length of the thread at pinching off without formation of satellite drops depends mainly on c_2, c_1 and a. The value c_2 represents the time at which the primary drop is formed through either end pinching or multiple breaking up. As recommended by Dong et al. [16], c_1 and c_2 are closely related to the liquid properties, nozzle radius and the waveform of the transducer pulse. The variation of c_2 in our current experiments is given in Fig. 3.21 and Table 8. c_2 in experiment 1 is approximately equal to that in experiment 5 and c_2 in experiment 3 to that in experiment 6. The value c_2 in experiment 4 is

almost the same as that in experiment 7. These results indicate that c_2 depends strongly on D_f. The relation between c_1 and the waveform of the transducer pulse is shown in preceding sections. Compared to the experimental results of Dong et al. [16], the ratio of the average speed of the retreating thread tail to the capillary speed, as shown in Table 8, ranges from 2.2 to 3.2 showing reasonable values. It is noted that in a few simulation cases, upon the pinching off of liquid thread from nozzle outlet, a tiny isolated liquid fragment called flotsam is observed. This flotsam is characterized by the vanishing velocity and size comparable to a single numerical cell. The appearance of the flotsam would interfere with the measurement of the retreating speed and the length of liquid thread at pinching off, and should be excluded from the data analysis. As already noted, experiments 12, 13, 16 and 17 appear to show no satellite drop because the tail of the liquid thread contracts into the thread head. Experiments 12 and 13 show an interval t_{b1} of pinching off smaller than in experiment 1. To estimate the critical value of experiments 12 and 13, we took $c_2 = 4.559$ and $a = 2.635$ as obtained in experiment 1 with the same value of D_f and because the value of a in experiments 14 and 15 is larger than that in experiment 8, as indicated in Table 8. We thus obtain the critical thread length at pinching off $l_b^* / R_{noz} = 4.055$, larger than $l_b / R_{noz} = 3.994$ in experiment 12, in agreement with a prediction obtained from Eq. (19). An estimate of the value l_b^* / R_{noz} in experiments

16 and 17 is similarly obtained on taking c_2 and a identical to values in experiment 9. Table 9 contains the estimate of a critical thread length l_b^* / R_{noz} in experiments 12, 13, 16 and 17. It is seen that a decrease in pause stage $\Delta \tau_{p2}$ could both shorten the liquid thread length l_b at pinching off and enlarge the critical value l_b^*, thus damping the satellite formation.

Based on the analysis above and from Eq. (19), we prefer the larger c_2, the smaller c_1 and the larger a to induce the larger l_b^* / R_{noz}. The larger the value l_b^* / R_{noz}, the wider the range of liquid thread length at pinching off without satellite formation. As shown in Figs. 3.21 and 3.7, both c_1 and c_2 appear to increase when D_f increases with constant We_f. An increase in We_f leads to a decrease in c_1 when D_f is fixed, as shown in Fig. 3.7. However, the larger We_f would cause the longer length l_b / R_{noz} of liquid thread at pinching off, which may contribute to the formation of satellite drops as depicted in Fig. 3.18. Both l_b / R_{noz} and c_1 tend to decrease as the pause stage $\Delta \tau_{p2}$ decreases. According to research of Dong et al.[16], the interval between c_1 and c_2 increases when liquid viscosity increases, liquid surface tension decreases or nozzle radius decreases. The parameter a is shown not to be significantly related to the liquid surface tension, nozzle radius and the waveform of the transducer pulse. However, as the liquid viscosity increases, the value of a would slightly increase. In conclusion, for a DOD drop generator with a given liquid,

the waveform of transducer pulse could carefully be designed to obtain a longer t_{b2},

a shorter t_{b1} and then larger upper limits l_b^*.

3.6 Supply, refill and equilibrium stages

To investigate the effect of D_s, $\Delta\tau_s$ and We_s on the liquid supply to the

printhead, we performed five numerical experiments, shown in Table 10. Figure 3.22

shows the temporal variation of the position of the free surface along the center line of

the nozzle in these cases. Upon initiation of the liquid supply, the flow in the nozzle

and ink supply channel is directed toward the ink chamber having a volume

displacement caused by the altered dimensions of the piezoelectric actuator. Under the

effect of the reversed flow, the meniscus near the nozzle outlet retracts and the mean

curvature of the interface is negative and becomes smaller and smaller (liquid surface

is concave). After the termination of supply, the flow in the nozzle turns to the nozzle

outlet through the effect of the imbalance of surface tension and inertia of the liquid in

the supply channel in this so-called refill stage. According to the position of the free

surface as a function of time shown in Fig. 3.22, the rate of the retracting meniscus

increases as We_s increases. Experiment 26 reveals that, after 6 μs, the rate of the

retracting meniscus decreases. The inertial force of the reversed flow is gradually

balanced by the restoring effect of the surface tension due to the smaller and smaller

curvature of the liquid interface. Except for experiment 23, all numerical experiments

show that the extent of invasion of the tube by the retracting meniscus is about 15 μm

from the nozzle outlet. Moreover, Fig. 3.22 also shows that the period of refill stage

which ends when the free surface along the nozzle center line reaches the nozzle exit

plane is approximately 9 μs in these cases. Figure 3.23 shows the temporal variation

of the rate of volume flow at the plane of the nozzle entrance. The rate of reversed

volume flow increases as We_s increases. After termination of the ink supply,

experiment 23 has a rate of volume flow less than experiment 24, whereas experiment

26 has a rate of volume flow less than experiment 25. The large extent of tube

invasion caused by the retracting meniscus might account for the small curvature of

the liquid interface, and then the larger restoring effect of surface tension to drive the

flow toward the plane of the exit nozzle at the termination of ink supply.

In most applications of microfluidic control, firing frequency, which represents

the number of drops per second the printhead can dispense, determines the throughput

or the speed at which an ink jet system can complete images. The firing frequency of

printheads is equal to the reciprocal of the total time interval of a transducer pulse. In

current study, the equilibrium stage $\Delta \tau_{p3}$ forms a large proportion of the transducer

pulse and then its value determines the firing frequency of the printhead. In order to

obtain stable drop formation, the value of $\Delta \tau_{p3}$ should be large enough to ensure the

flow in the printhead of reverting to the initial condition for the next drop ejection.

Figure 3.24 shows the variation of the primary drop volume and velocity with firing

frequency by varying the value of $\Delta\tau_{p3}$ in experiment 1. Both variation of drop

volume and velocity are around 1 % at frequency of 4.348 kHz. When the firing

frequency increases up to 15.625 kHz, the discrepancy of drop volume is still below

10 %, yet the drop velocity is as large as 21.6 %. From the results shown in Fig. 3.24,

the firing frequency below 5 kHz appears to confirm the stable drop formation.

3.7 Effect of the Ohnesorge number

In order to investigate the effect of the Ohnesorge number, Oh on DOD drop

formation, we varied liquid viscosity, thus resulting in Oh altered from 0.02 (water) to

1. Figure 3.25 shows the variation with Oh of primary drop volume and velocity; the

drop volumes are approximately constant and the drop velocity decreases slightly

when Oh increases. It is noticed that when Oh=0.2, the tail of the liquid thread after

pinching off from nozzle outlet recoils toward the thread head and there occurs no

satellite drops, thus causing an increased volume of the drop. Figure 3.26 shows the

temporal variation of the rate of volume flow at the plane of the nozzle entrance. The

total liquid volume entering the nozzle during the forward stage decreases with Oh.

Furthermore, when Oh increases, the forward momentum density of ejected liquid

decreases due to increasing viscous resistance; in the cases of Oh=0.5 and Oh=1.0, the

pinching off of the liquid thread fails to occur and a powerful actuation is required.

Figure 3.27 shows the temporal evolution of the shape of the liquid thread when Oh

are 0.15, 0.2 and 0.5. It would appear that the case of Oh=0.15 shows one satellite

drop formed by end pinching whereas that of Oh=0.2 no satellite formation. When Oh

increases up to 0.5, fluid interface disruption would not occur. The lower the rate of

viscous momentum transfer, the lower the Ohnesorge number. Therefore, the rate at

which the effect of reversed inflow can be felt across the entire liquid thread increases

as Oh increases. The variation with Oh of pinching off and breaking up times is

shown in Fig. 3.28. Both pinching off and breaking up times tend to increase as Oh

increases. It is possible that increasing viscous force relative to surface tension force

slows the capillary pinching of the thread tail and bulbous thread head. Figure 3.29

shows the variation with Oh of the length of the liquid thread at pinching off. The

liquid thread length appears to decrease as Oh increases; furthermore, the values of

l_b / R_{noz} in these cases are all smaller than 8.8 and the end-pinching mode is then

dominant in the formation of satellite drops. To suppress satellite formation, we prefer

the larger interval between pinching-off and breaking-up times to induce the larger

l_b^* / R_{noz}, and the smaller value l_b / R_{noz} according to Eq. (19). The interval between

c_1 and c_2 tends to increase when Oh increases, as shown in Fig. 3.28. Therefore,

for a DOD application, the suppression of satellite drops could be achieved by increasing liquid viscosity, decreasing surface tension and decreasing nozzle outlet radius. Figure 3.30 shows the temporal variation of the position of the free surface along the center line of the nozzle. Despite different values of Oh, the rates of the retracting meniscus are approximately the same during the supply stage; the smaller the value Oh, the larger the extent of invasion of the tube by the retracting meniscus. Moreover, Fig. 3.30 also makes plain that the periods of refill stage are virtually invariant with Oh.
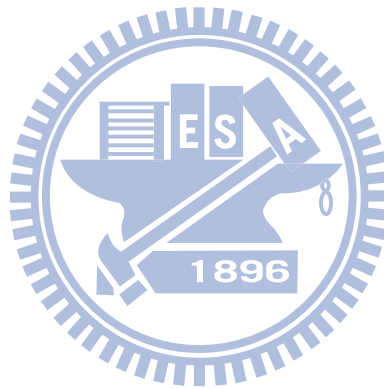
Table 1. Interval for a liquid thread from a nozzle outlet to pinch off, with three meshes.

186,898 cells	282,408 cells	411,654 cells
period to pinch off / μs		
30.512	30.512	30.515

Table 2. Velocity of the drop head with three meshes.

Time / μs	186,898 cells	282,408 cells	411,654 cells
	Head velocity / m s^{-1} (drop tip position / μm)		
15	5.81632 (46.3)	5.59234 (45.9)	5.66525 (46)
20	4.00525 (70.7)	4.15712 (69.7)	4.20037 (70.3)
25	2.97289 (87.8)	2.93412 (87.1)	2.83467 (87.1)
30.5	2.74526 (103.1)	2.75629 (101.9)	2.72694 (102.5)
35	3.09152 (116)	3.19418 (114.9)	3.25551 (115.8)
40	2.84138 (131.3)	2.58049 (130)	2.46021 (130.1)

Table 3. Primary drop volume with three meshes.

Time / μs	186,898 cells	282,408 cells	411,654 cells
	Primary drop volume /pL		
30.5	8.94073	8.93109	9.081
40	6.89494	7.34343	7.45479

Table 4. List of experiments for the forward stage.

Experiment	D_s /μm	$\Delta\tau_s$ /μs	$\Delta\tau_{p1}$ /μs	D_f /μm	$\Delta\tau_f$ /μs	We_f	$\Delta\tau_{p2}$ /μs	D_b /μm	$\Delta\tau_b$ /μs
1	0.03	3	9	0.06	3	162.7	3.5	0.03	3
○2	0.03	3	9	0.03	3	40.7	3.5	0.03	3
3	0.03	3	9	0.03	1.5	162.7	3.5	0.03	3
4	0.03	3	9	0.12	6	162.7	3.5	0.03	3
5	0.03	3	9	0.06	1.5	650.7	3.5	0.03	3
6	0.03	3	9	0.03	0.75	650.7	3.5	0.03	3
7	0.03	3	9	0.12	4.8	254.2	3.5	0.03	3

Table 5. List of experiments for the backward stage.

Experiment	D_s /μm	$\Delta\tau_s$ /μs	$\Delta\tau_{p1}$ /μs	D_f /μm	$\Delta\tau_f$ /μs	$\Delta\tau_{p2}$ /μs	D_b /μm	$\Delta\tau_b$ /μs	We_b
1	0.03	3	9	0.06	3	3.5	0.03	3	40.7
8	0.03	3	9	0.06	3	3.5	0.06	3	162.7
9	0.03	3	9	0.06	3	3.5	0.03	1.5	162.7
10	0.03	3	9	0.06	3	3.5	0.03	6	10.2
11	0.03	3	9	0.06	3	3.5	0.06	12	10.2

Table 6. List of experiments for the pause stage.

Experiment	D_s /μm	$\Delta\tau_s$ /μs	$\Delta\tau_{p1}$ /μs	D_f /μm	$\Delta\tau_f$ /μs	$\Delta\tau_{p2}$ /μs	D_b /μm	$\Delta\tau_b$ /μs
1	0.03	3	9	0.06	3	3.5	0.03	3
12	0.03	3	9	0.06	3	1.75	0.03	3
13	0.03	3	9	0.06	3	0.8	0.03	3
8	0.03	3	9	0.06	3	3.5	0.06	3
14	0.03	3	9	0.06	3	1.75	0.06	3
15	0.03	3	9	0.06	3	0.8	0.06	3
9	0.03	3	9	0.06	3	3.5	0.03	1.5
16	0.03	3	9	0.06	3	1.75	0.03	1.5
17	0.03	3	9	0.06	3	0.8	0.03	1.5

Table 7. List of additional experiments.

Experiment	D_s /μm	$\Delta\tau_s$ /μs	$\Delta\tau_{p1}$ /μs	D_f /μm	$\Delta\tau_f$ /μs	$\Delta\tau_{p2}$ /μs	D_b /μm	$\Delta\tau_b$ /μs
5	0.03	3	9	0.06	1.5	3.5	0.03	3
18	0.03	3	9	0.06	1.5	0.8	0.03	3
19	0.03	3	9	0.06	1.5	0.8	0.03	1.5
20	0.03	3	9	0.06	1.5	0.8	0.03	0.75
21	0.03	3	9	0.06	1.5	0	0.12	3

Table 8. Liquid thread length at pinch-off compared with prediction.

Experiment	C_1	C_2	a	v_{ca} /m s^{-1}	v_p /m s^{-1}	r_p / R_{noz}	l_b / R_{noz}	l_b^* / R_{noz}
1	3.899	4.559	2.635	2.056	2.38	0.745	4.0	3.739
4	4.378	5.217	2.501	2.056	2.443	0.949	5.773	4.099
8	4.197	4.617	2.721	2.056	2.511	0.745	4.385	3.143
9	3.899	4.498	2.833	2.056	2.4	0.745	3.813	3.698
10	3.898	4.858	2.259	2.056	2.56	0.744	4.501	4.169
11	3.719	4.859	2.298	2.056	2.546	0.744	4.974	4.618
14	4.2	4.62	3.263	2.056	2.426	0.751	4.0	3.371
15	3.99	4.65	3.004	2.056	2.433	0.746	3.848	3.983

Table 9. Estimate of the critical value of the thread length at pinching off.

Experiment	C_1	C_2	t_{ca} / μs	a	v_{ca} /m s^{-1}	l_b / R_{noz}	l_b^* / R_{noz}
12	3.78	4.559	8.341	2.635	2.056	3.994	4.055
13	3.63	4.559	8.341	2.635	2.056	3.878	4.449
16	3.84	4.498	8.341	2.833	2.056	3.644	3.869
17	3.721	4.498	8.341	2.833	2.056	3.592	4.206

Table 10. List of experiments for the supply stage.

Experiment	D_s /μm	$\Delta\tau_s$ /μs	We_s
22	0.03	3	40.7
23	0.06	3	162.7
24	0.03	1.5	162.7
25	0.03	6	10.2
26	0.06	12	10.2
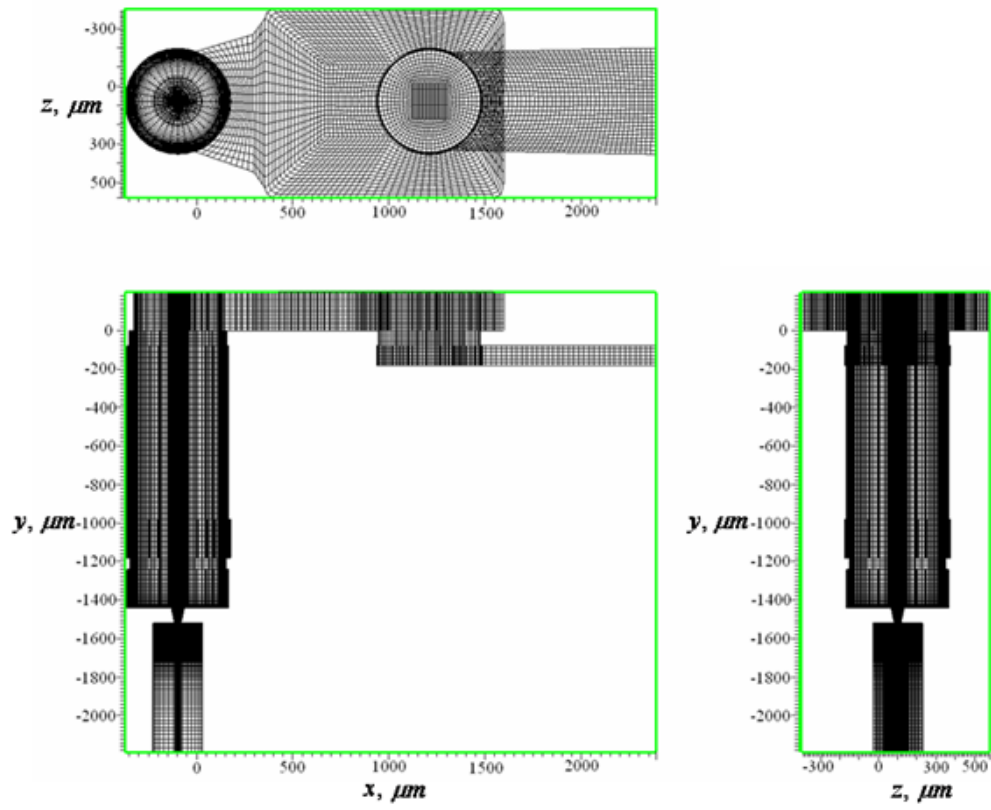
Figure 3.1. Numerical grids of a printhead (Picojet).
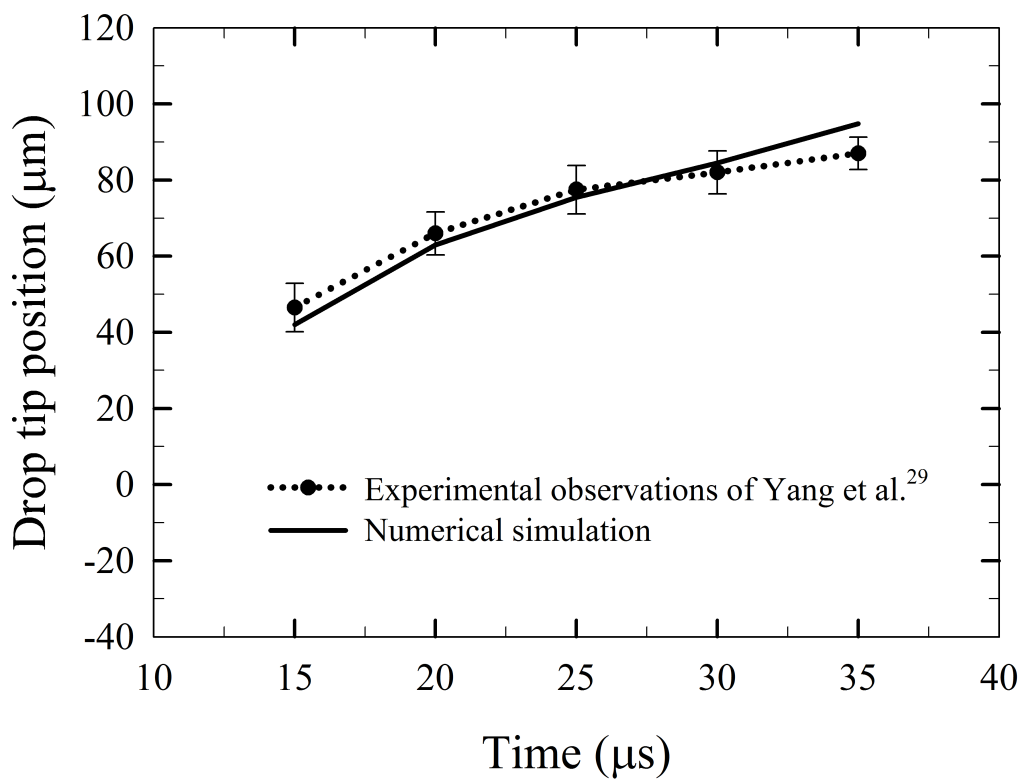
Figure 3.2. Comparison between experiment and numerical simulation.

| 14.0 µs | 19.0 µs | 33.0 µs | 36.5 µs | 41.0 µs | 51.0 µs |
| (a) | (b) | (c) | (d) | (e) | (f) |
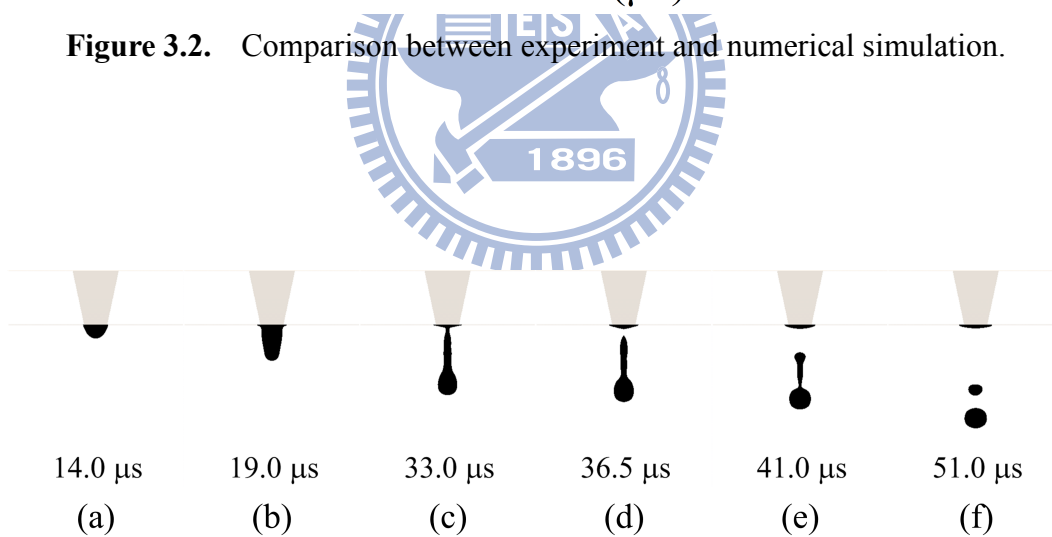
Figure 3.3. Key stages observed in our numerical experiment 4: (a) ejection, (b) stretching, (c) necking, (d) pinching off, (e) recoil and (f) breaking up.

12.0 μs   14.0 μs   16.0 μs   18.5 μs   20.5 μs

(a)

12.0 μs   14.0 μs   16.0 μs   18.5 μs   20.5 μs

(b)

12.0 μs   14.0 μs   16.0 μs   18.5 μs   20.5 μs

(c)
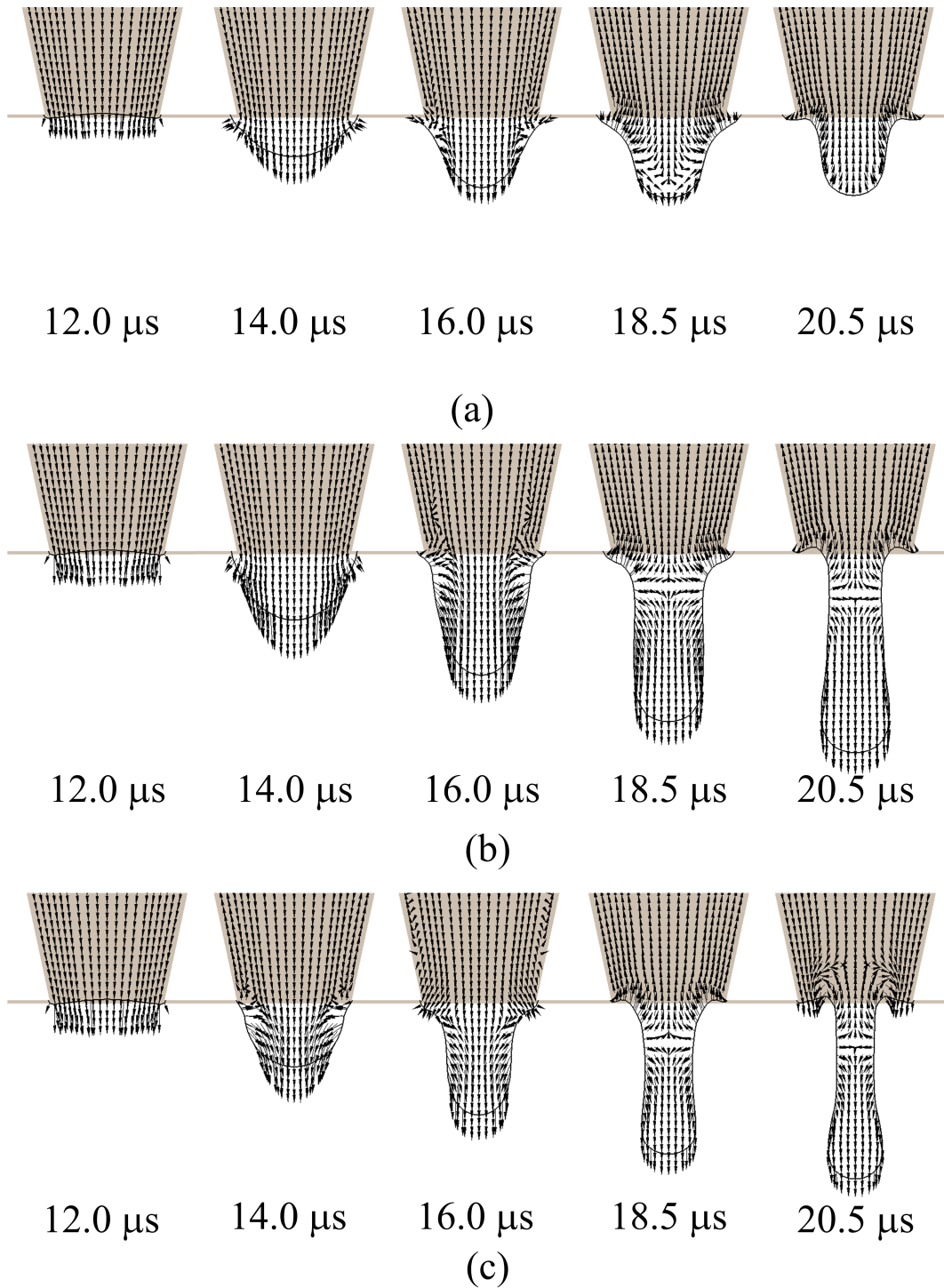
Figure 3.4. Evolution of the liquid thread shape and velocity vector at the liquid side: experiments (a) 2, (b) 1 and (c) 3.
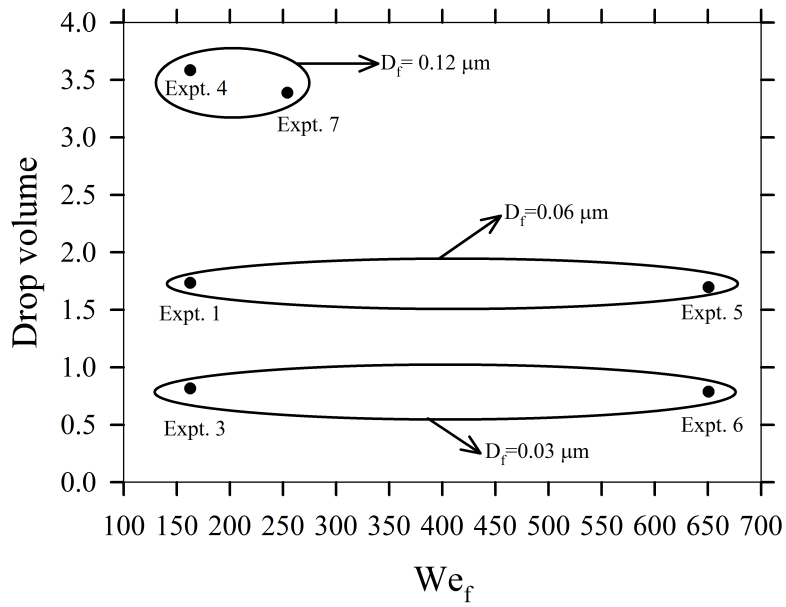
(a)
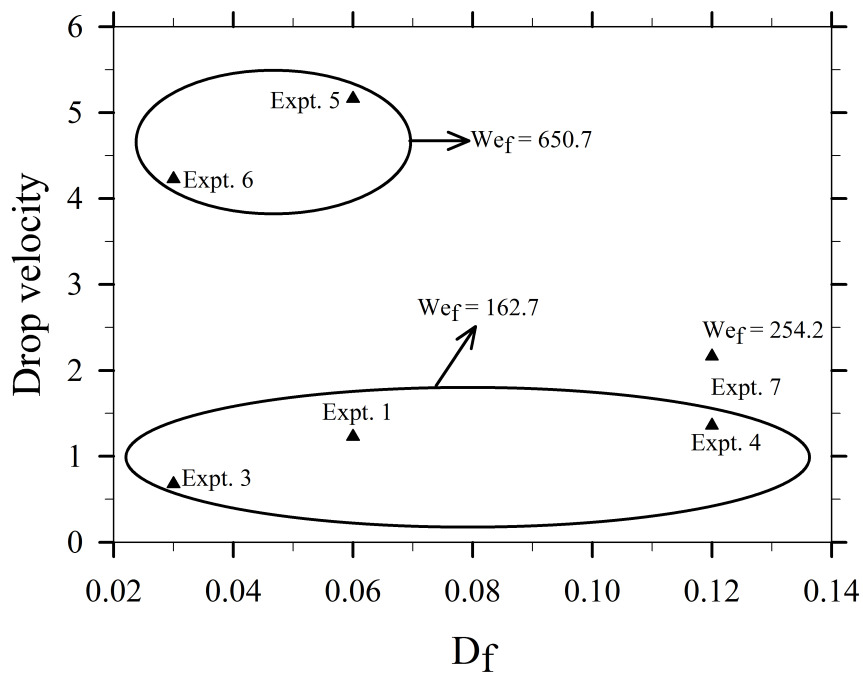
(b)

Figure 3.5. Variation of (a) the volume of the primary drop and (b) the velocity of the primary drop in experiments; the volume is in units of $R_{noz}^3 = 5.044$ pL and the velocity in units of $R_{noz}/t_{ca} = 2.056$ m s^{-1}.
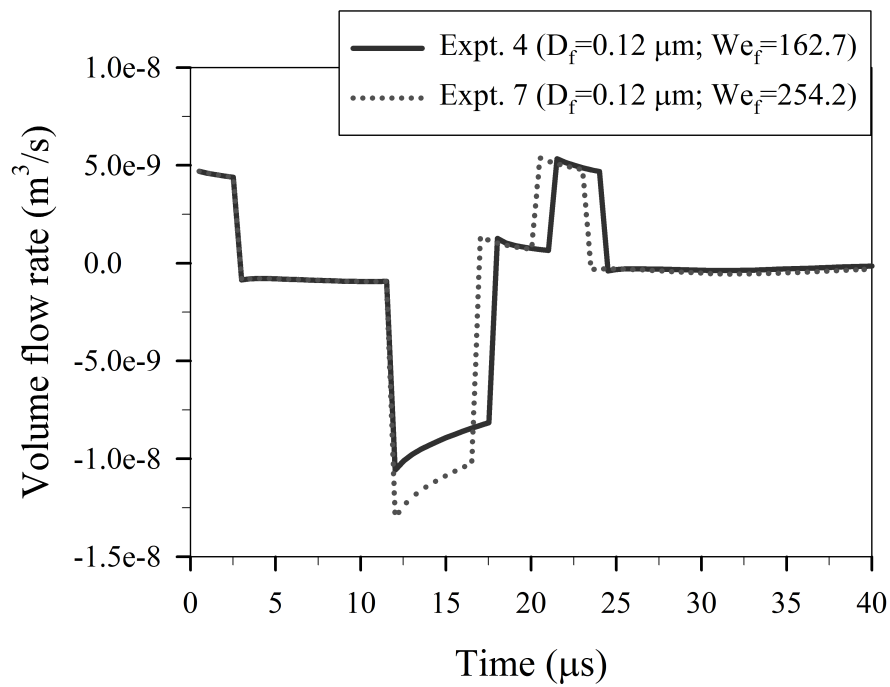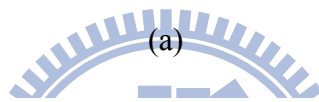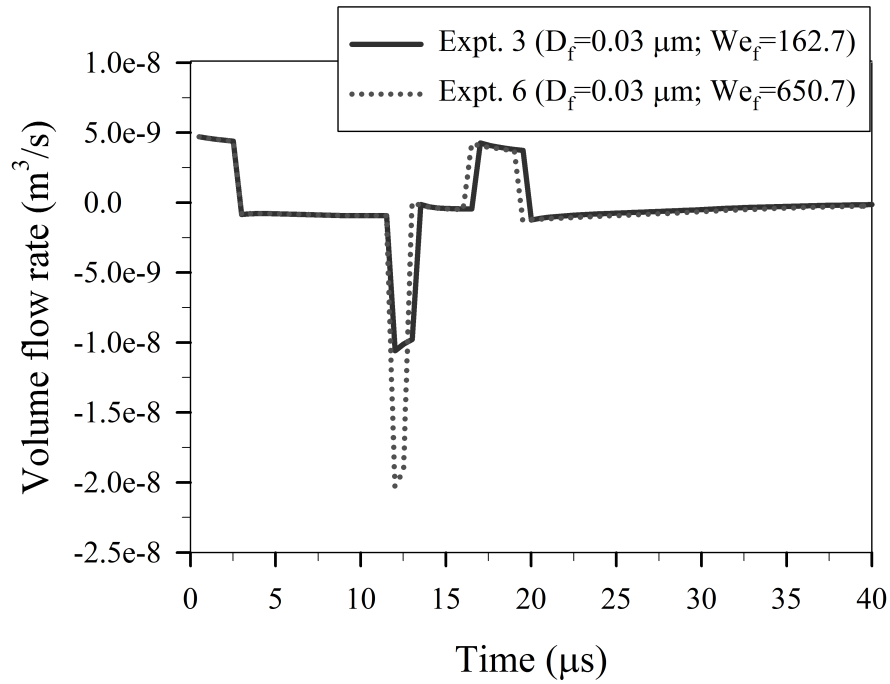
Figure 3.6. Temporal variation of the rate of volume flow at the plane of the nozzle entrance: (a) experiments 3 and 6, and (b) experiments 4 and 7.
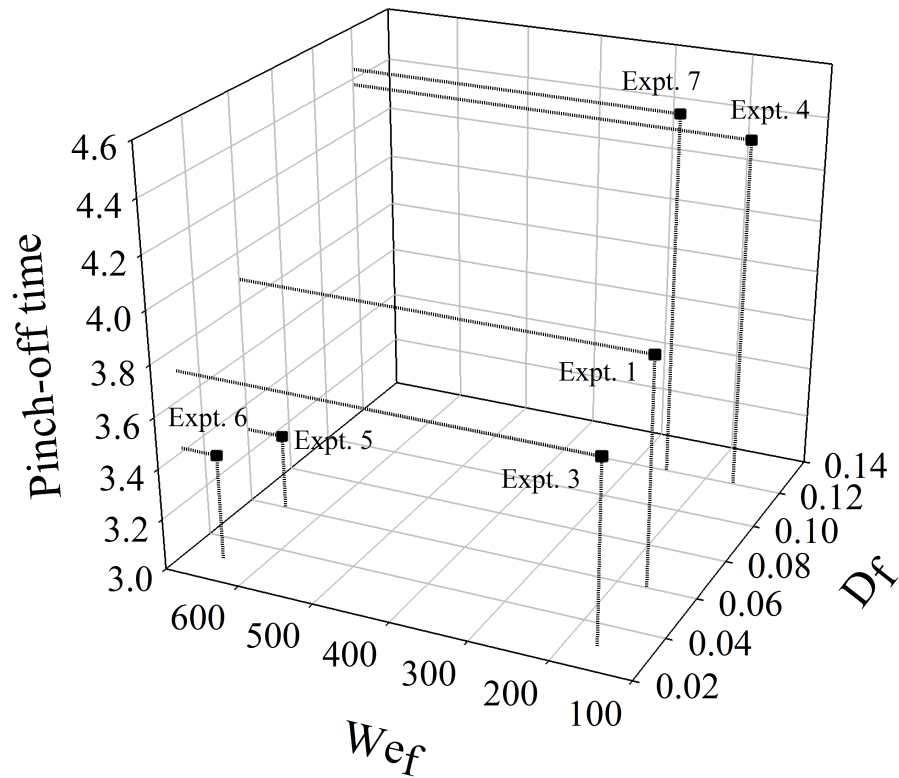
Figure 3.7. Variation with experiments of pinch-off time of liquid thread from nozzle exit; the time is in units of t_{ca}=8.341 μs.
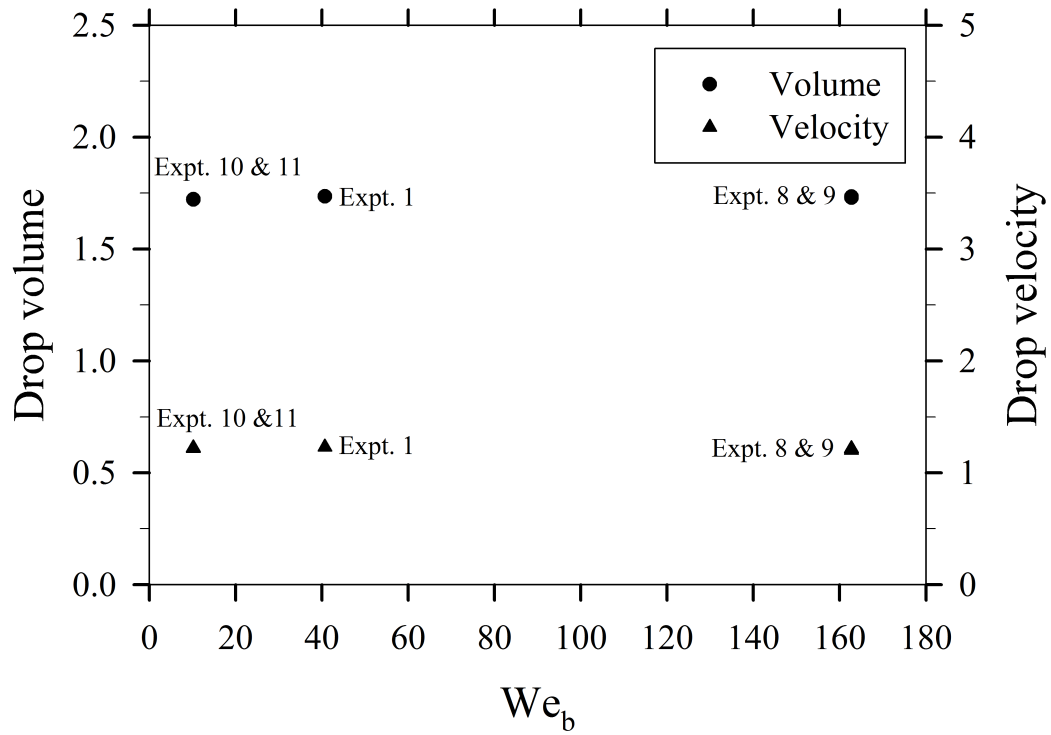
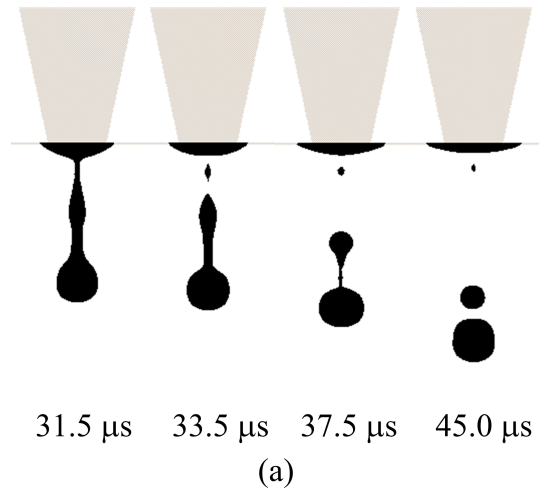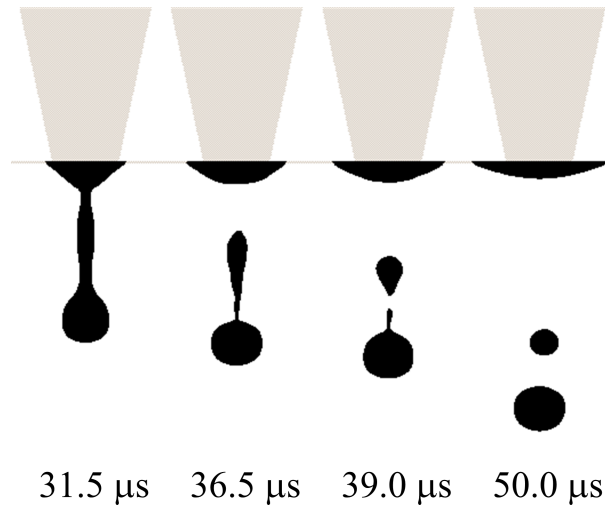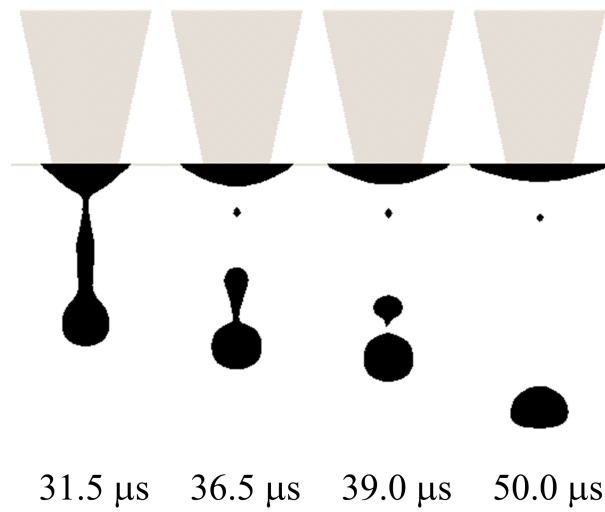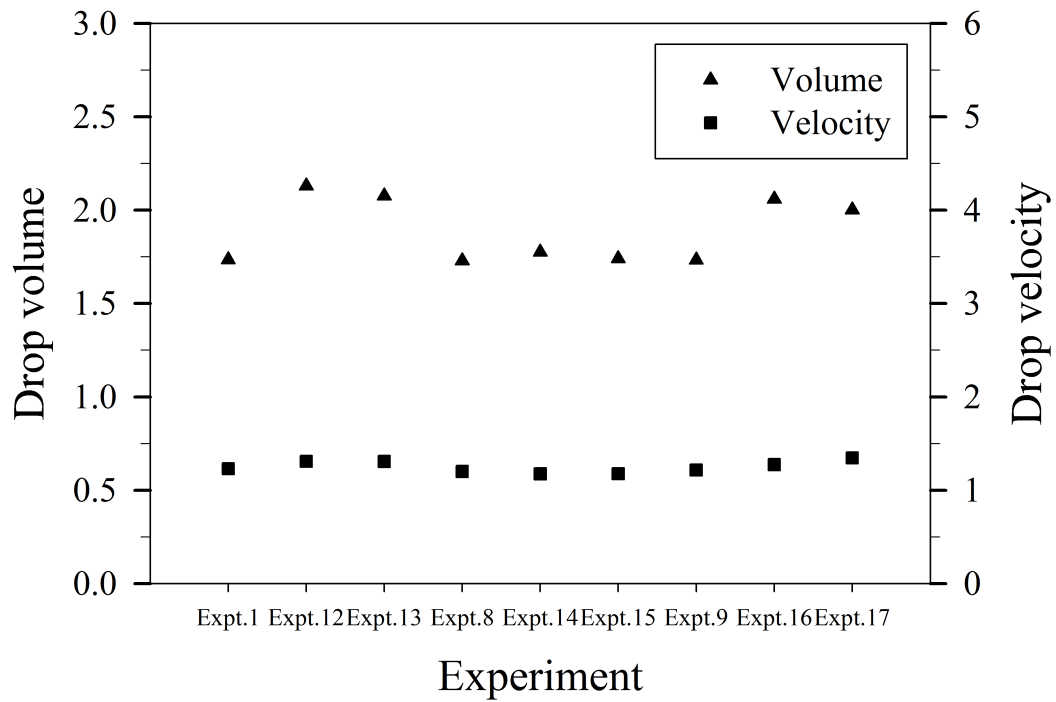**Figure 3.8.** Variation of the volume of the primary drop and velocity of the primary

drop in experiments; the volume is in units of $R_{noz}^3 = 5.044$ pL and the velocity in

units of $R_{noz} / t_{ca} = 2.056$ m s^{-1}.

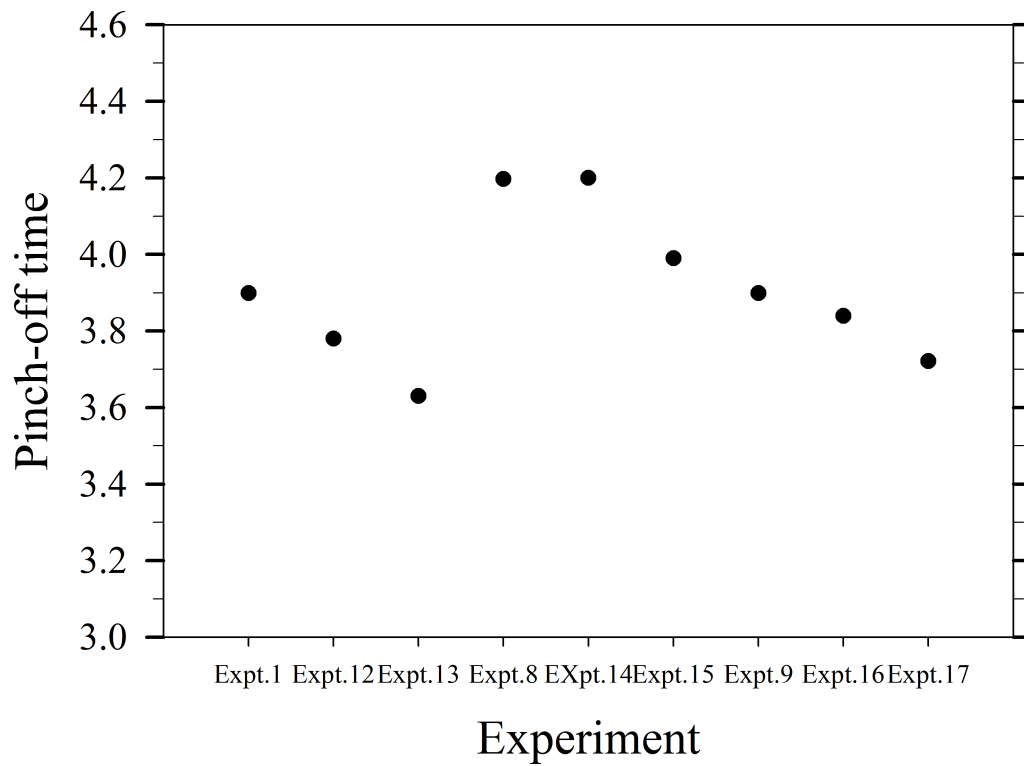**Figure 3.9.** Evolution of the shape of the liquid thread during the backward stroke.
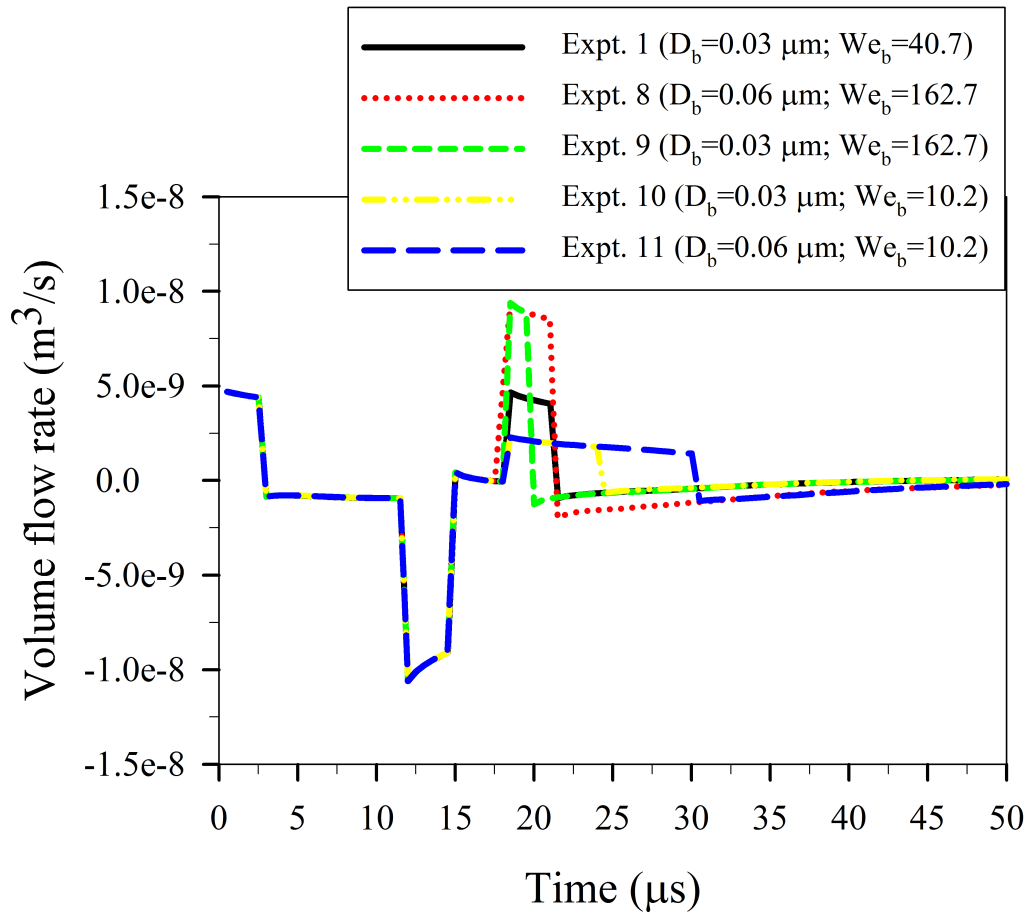
Figure 3.10. Temporal variation of the rate of volume flow.

The figure legend reads:

Expt. 1 (D_b=0.03 μm; We_b=40.7)
Expt. 8 (D_b=0.06 μm; We_b=162.7
Expt. 9 (D_b=0.03 μm; We_b=162.7)
Expt. 10 (D_b=0.03 μm; We_b=10.2)
Expt. 11 (D_b=0.06 μm; We_b=10.2)

The vertical axis is labeled "Volume flow rate (m^3/s)" with values 1.5e-8, 1.0e-8, 5.0e-9, 0.0, -5.0e-9, -1.0e-8, -1.5e-8.

The horizontal axis is labeled "Time (μs)" with values 0, 5, 10, 15, 20, 25, 30, 35, 40, 45, 50.
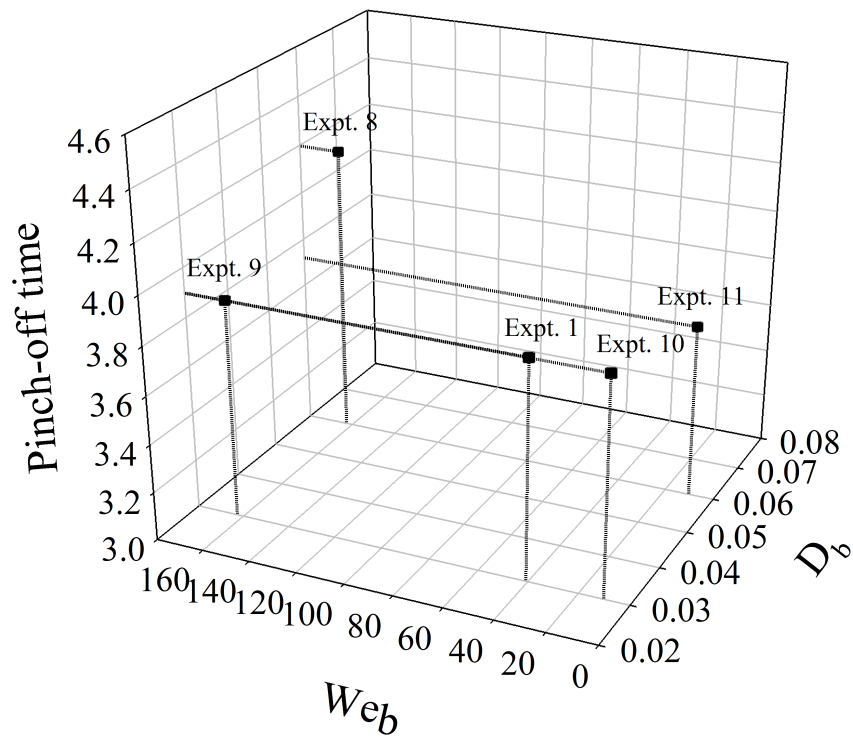
Figure 3.11. Variation with experiments of pinch-off time of liquid thread from nozzle exit; the time is in units of t_{ca}=8.341 μs.

| 31.5 μs | 33.5 μs | 37.5 μs | 45.0 μs |

(a)

| 31.5 μs | 33.5 μs | 37.5 μs | 45.0 μs |

(b)
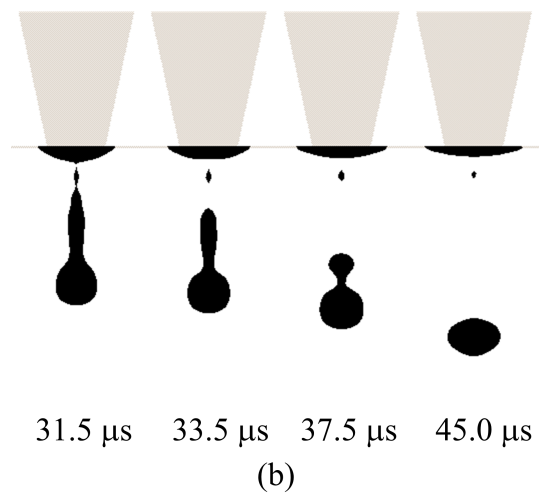
Figure 3.12. Temporal evolution of the liquid thread shape in experiments (a) 1 and (b) 12.

31.5 μs   36.5 μs   39.0 μs   50.0 μs

(a)

31.5 μs   36.5 μs   39.0 μs   50.0 μs

(b)

Figure 3.13. Temporal evolution of the liquid thread shape in experiments (a) 8 and (b) 15.

Figure 3.14. Variation of the volume of the primary drop and velocity of the primary drop in experiments; the volume is in units of $R_{noz}^3 = 5.044$ pL and the velocity in units of $R_{noz}/t_{ca} = 2.056$ m s^{-1}.

Figure 3.15. Variation of duration of the liquid thread pinching off from nozzle exit; the time is in units of t_{ca}=8.341 μs.
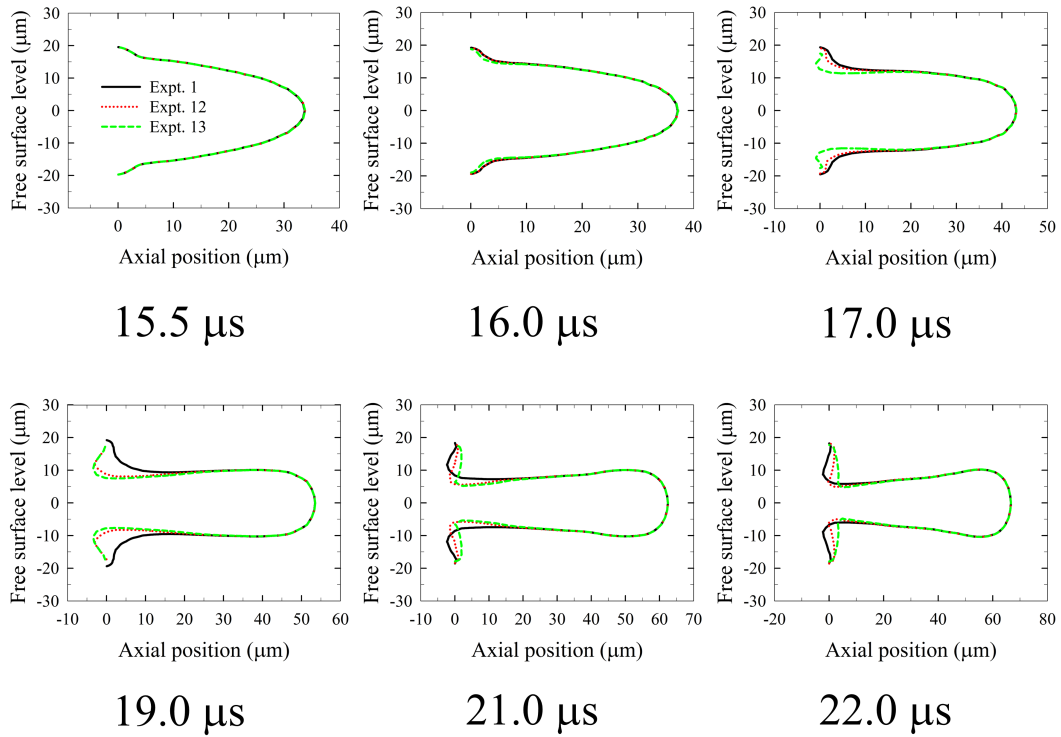
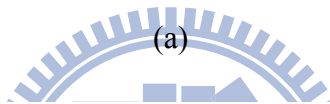**Figure 3.16.** Temporal evolution of the free surface contour of the liquid thread crossing the period of actuation of the backward stroke.
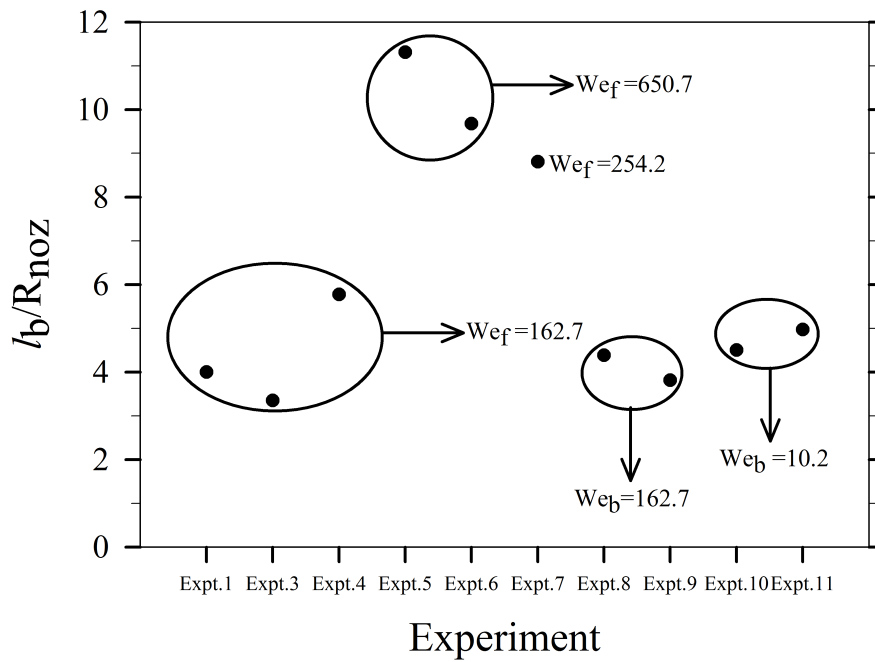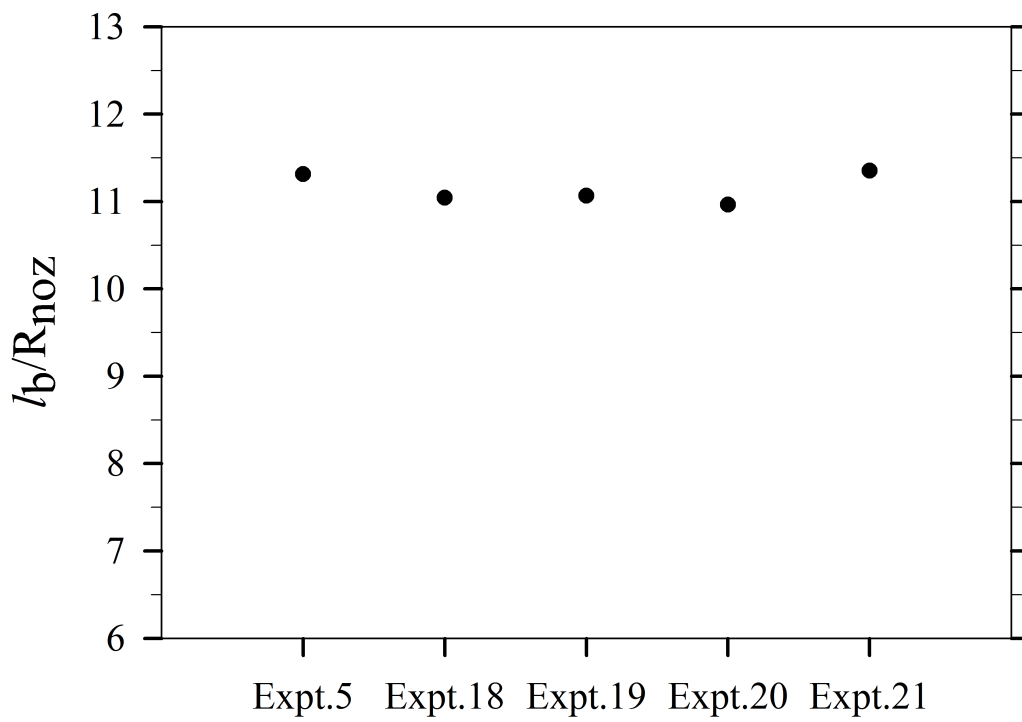

24.0 μs   30.0 μs   36.0 μs   38.0 μs   42.0 μs
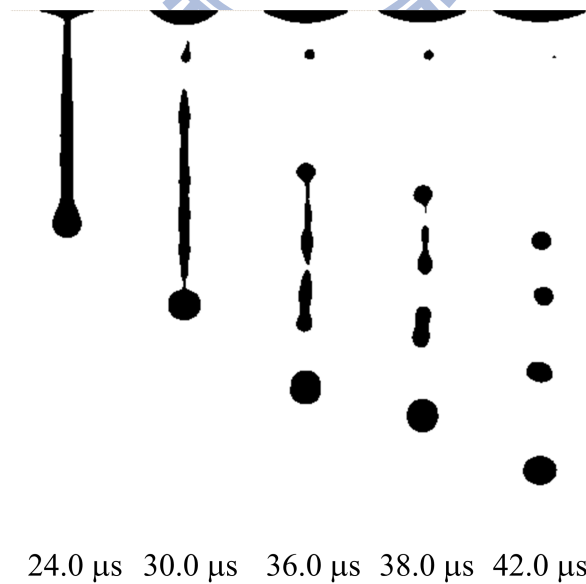
Figure 3.17. Satellite formation by multiple breaking up observed in numerical experiment 6.

(a)
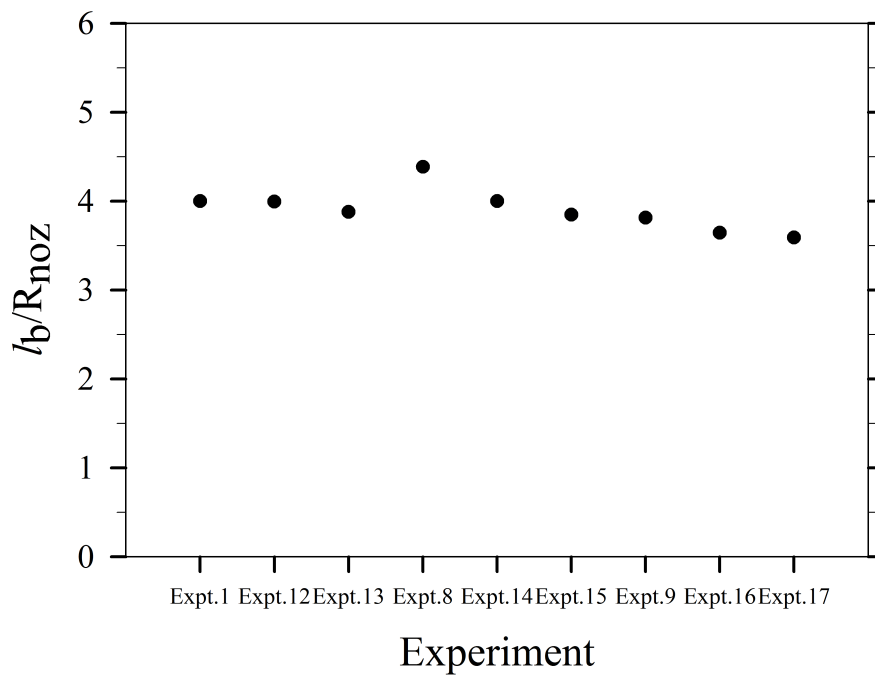
(b)

Figure 3.18. Variation of length of the liquid thread at pinching off with varied conditions in (a) forward and backward stages, and (b) the pause stage.

Figure 3.19. Variation of length of liquid thread at pinching off in various conditions.
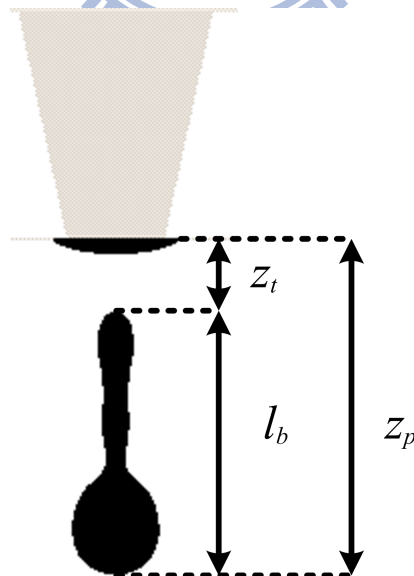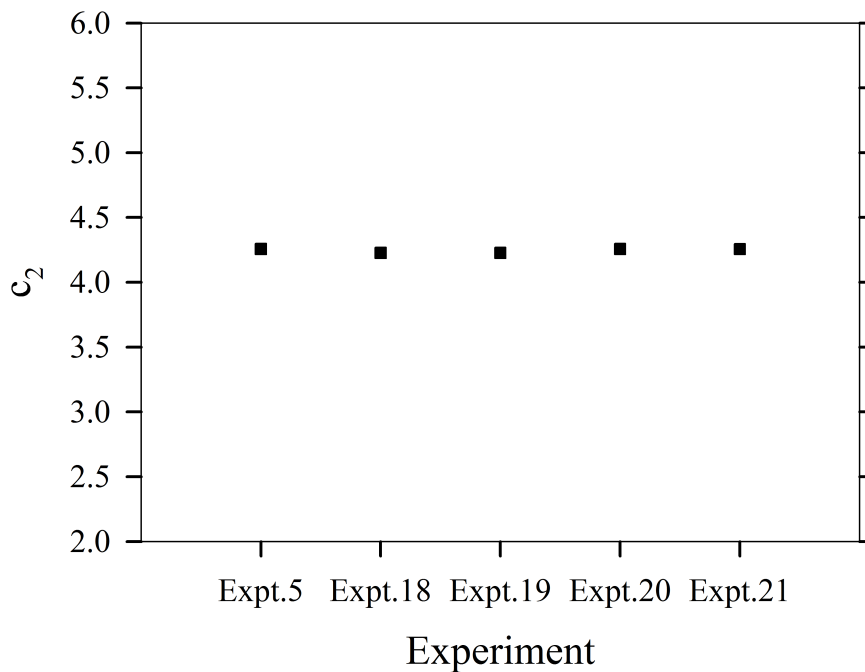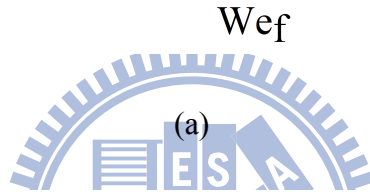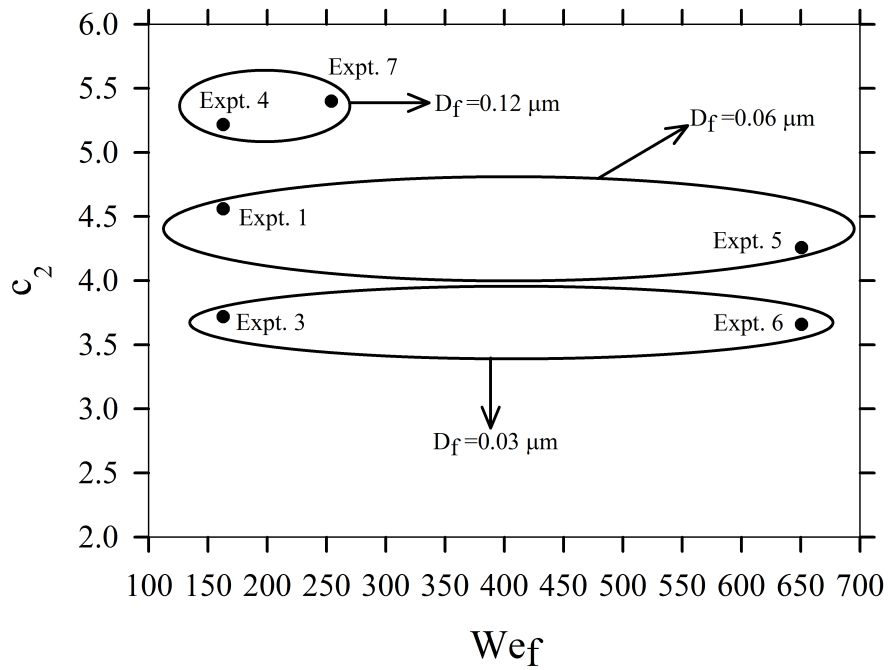

Figure 3.20. Schematic diagram of representative points during the evolution of an ejected liquid thread.

(a)

(b)

Figure 3.21. Variation of c_2 with experiments shown in Tables (a) 4 and (b) 7.
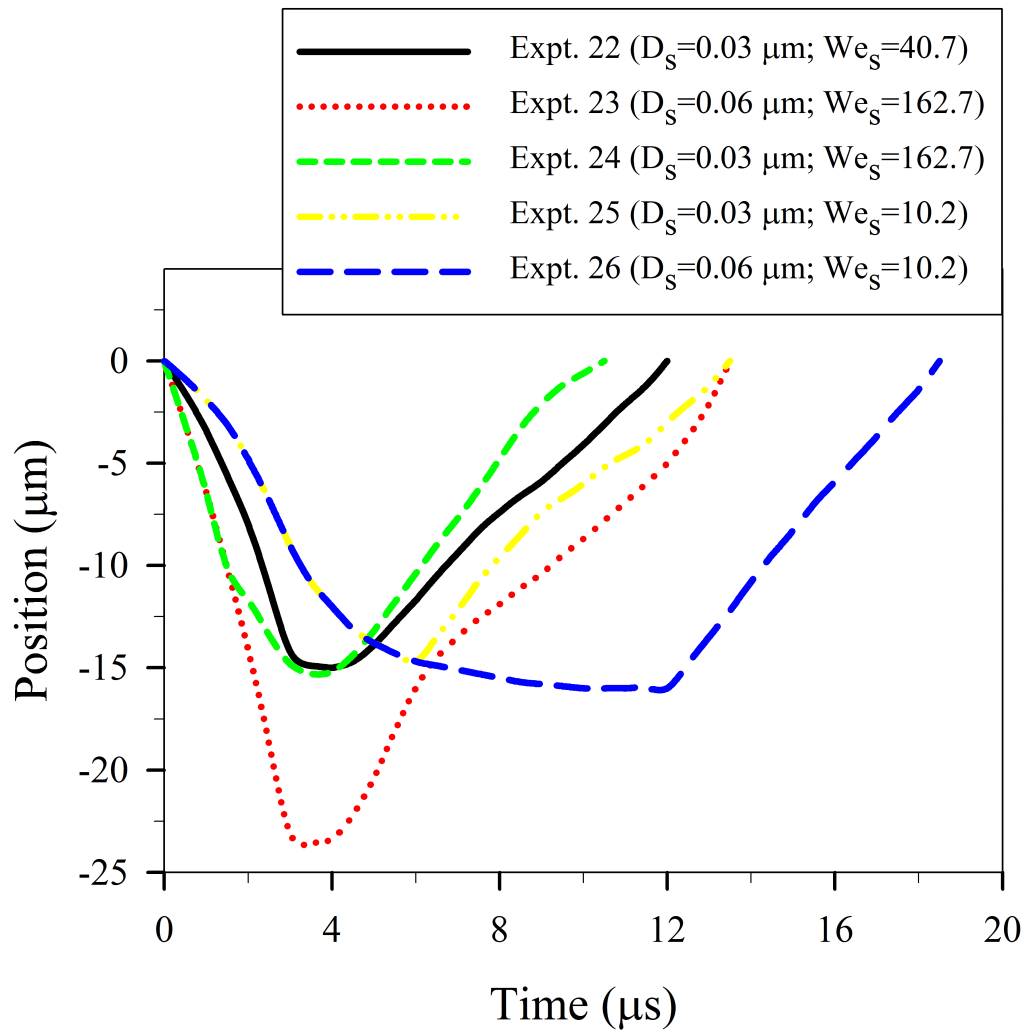
Figure 3.22. Temporal variation of the position of the free surface along the center line of the nozzle.
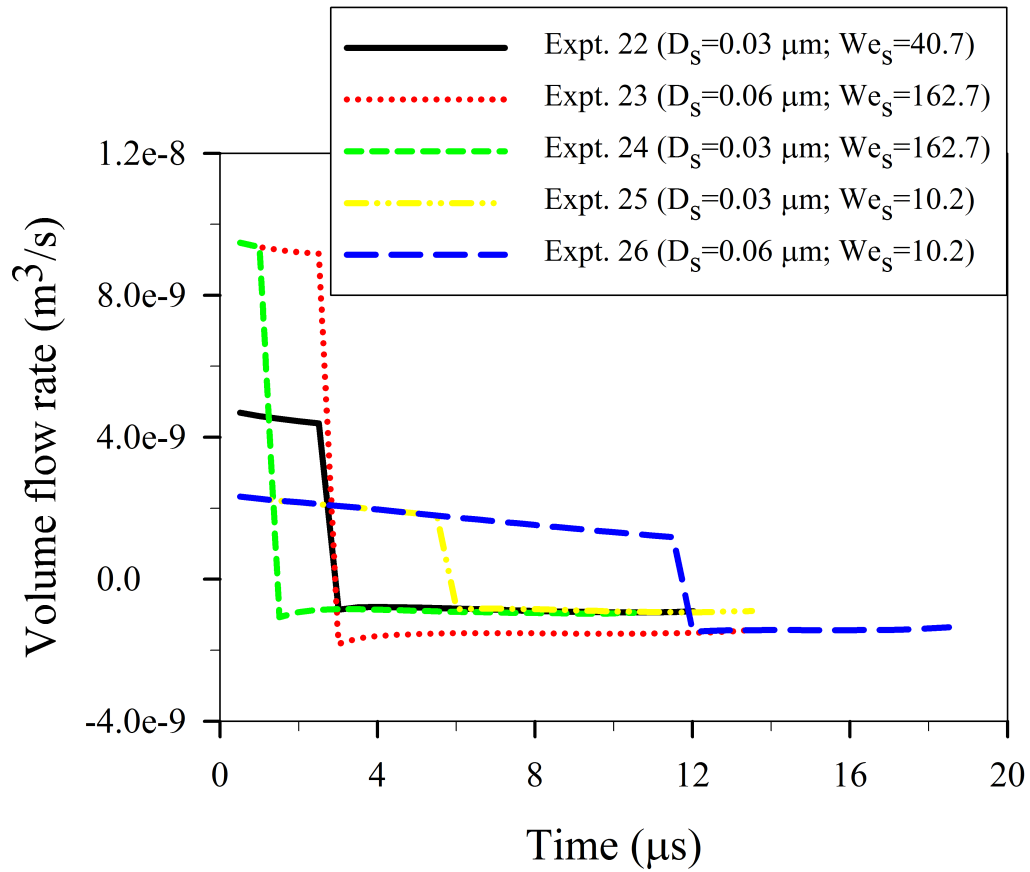
Figure 3.23. Temporal variation of the rate of volume flow rate at the plane of the nozzle entrance.

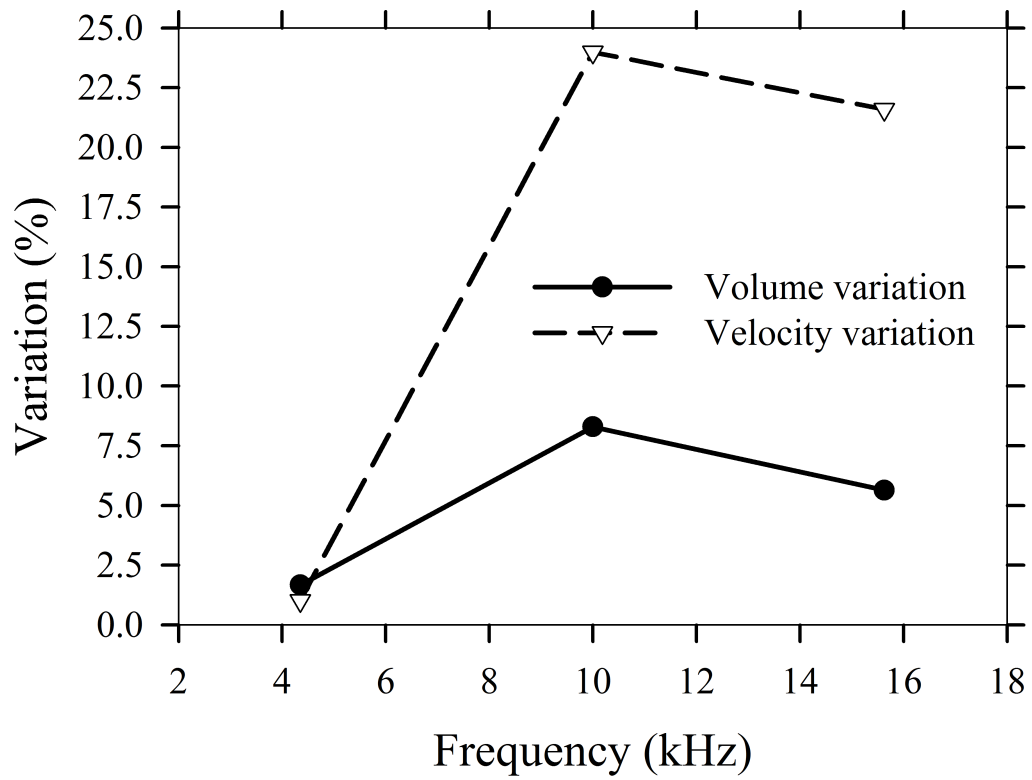**Figure 3.24.** Variation of the primary drop volume and velocity with firing frequency.
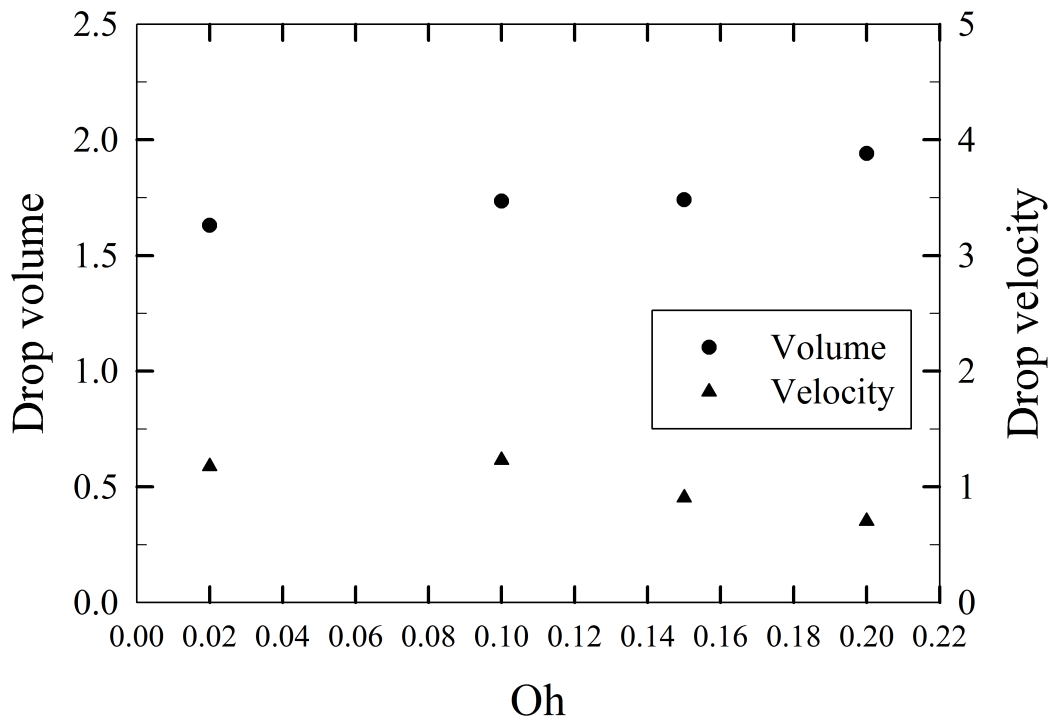
Figure 3.25. Variation with the Ohnesorge number Oh of the volume of the primary drop and velocity of the primary drop in experiments; the volume is in units of $R_{noz}^{3} = 5.044$ pL and the velocity in units of $R_{noz}/t_{ca} = 2.056$ m s^{-1}.
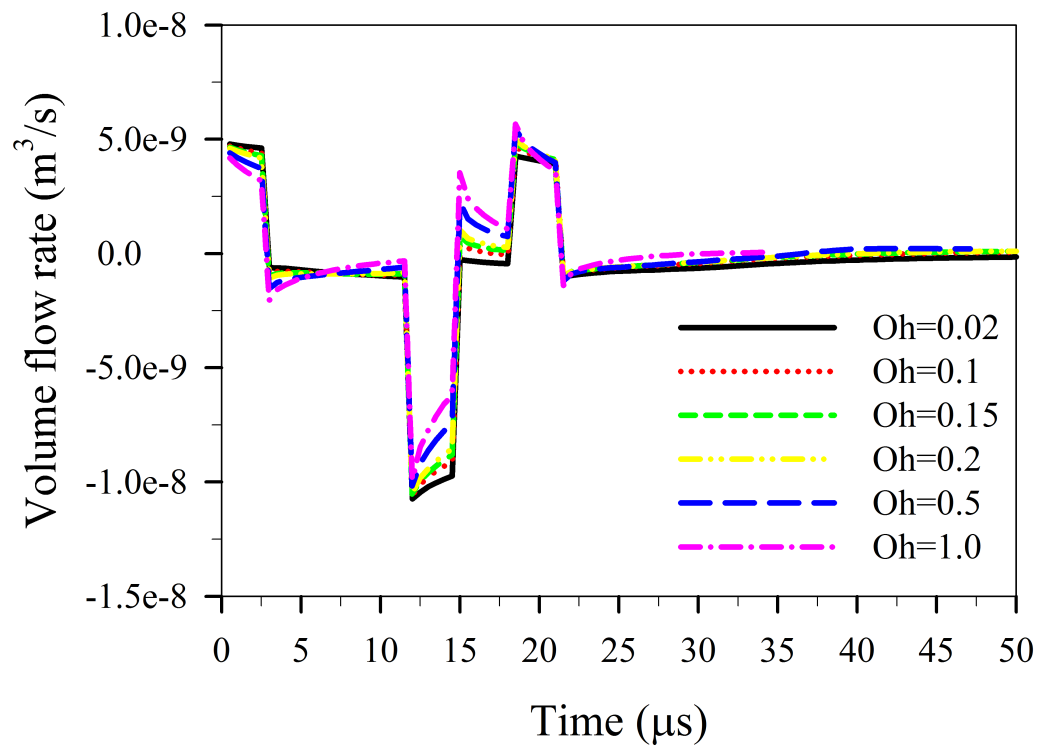
Figure 3.26. Temporal variation of the rate of volume flow.

15.0 µs   18.0 µs   21.0 µs   32.0 µs   36.0 µs   40.0 µs

(a)

15.0 µs   18.0 µs   21.0 µs   32.0 µs   36.0 µs   40.0 µs

(b)

15.0 µs   18.0 µs   21.0 µs   32.0 µs   36.0 µs   40.0 µs
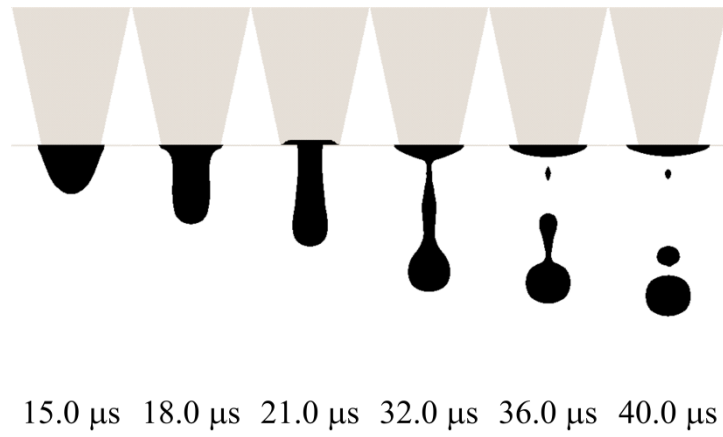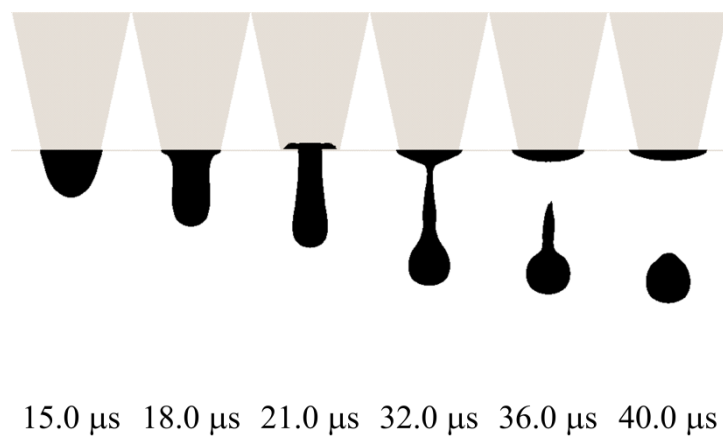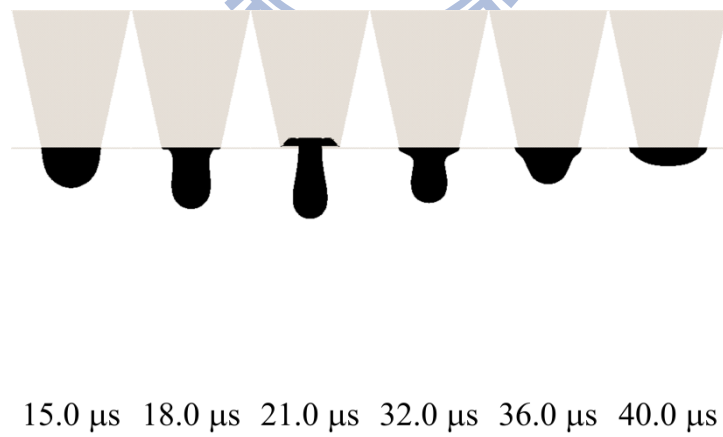
(c)

Figure 3.27. Temporal variation of the liquid thread shape: (a) Oh=0.15, (b) Oh=0.2 and (c) Oh=0.5.
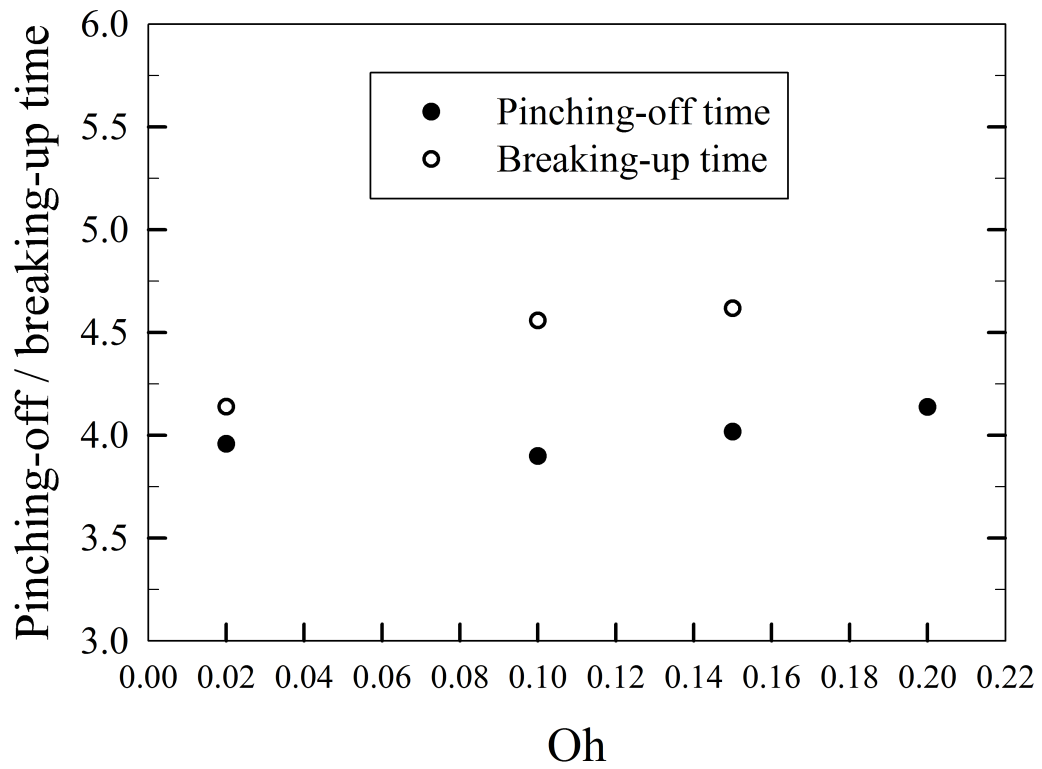
Figure 3.28. Variation with the Ohnesorge number Oh of the pinching-off and breaking-up times of liquid thread; the time is in units of t_{ca}=8.341 μs.
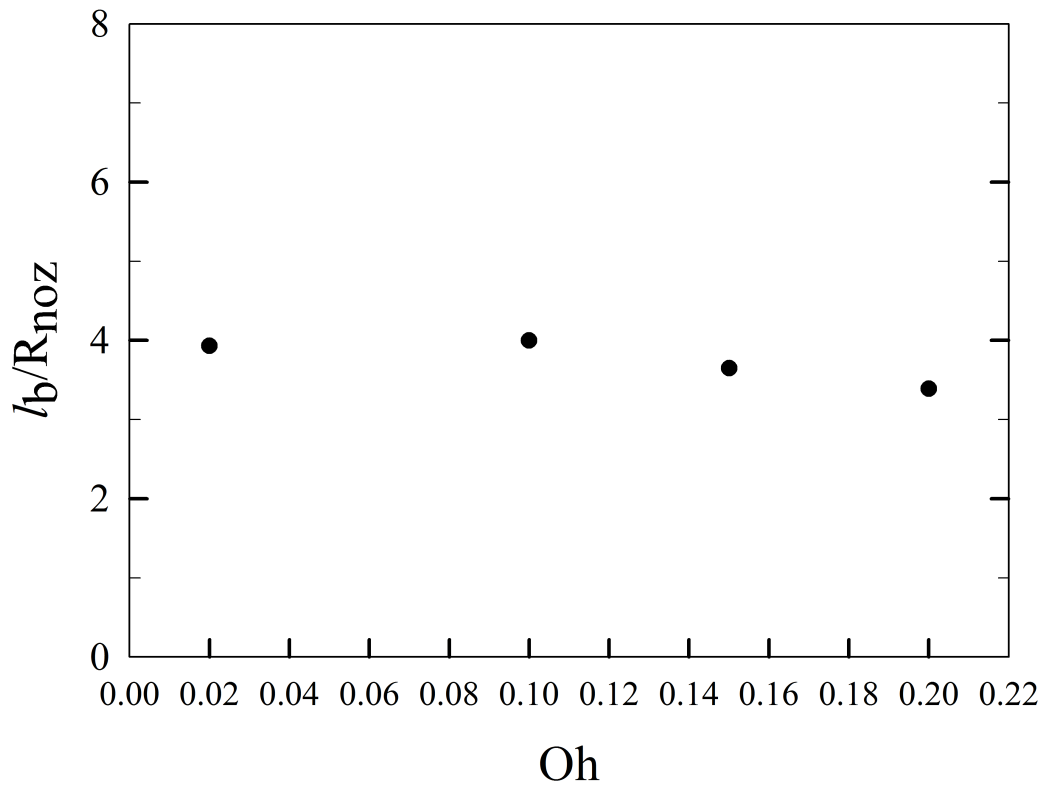
Figure 3.29. Variation with the Ohnesorge number Oh of the liquid thread length at pinching off.
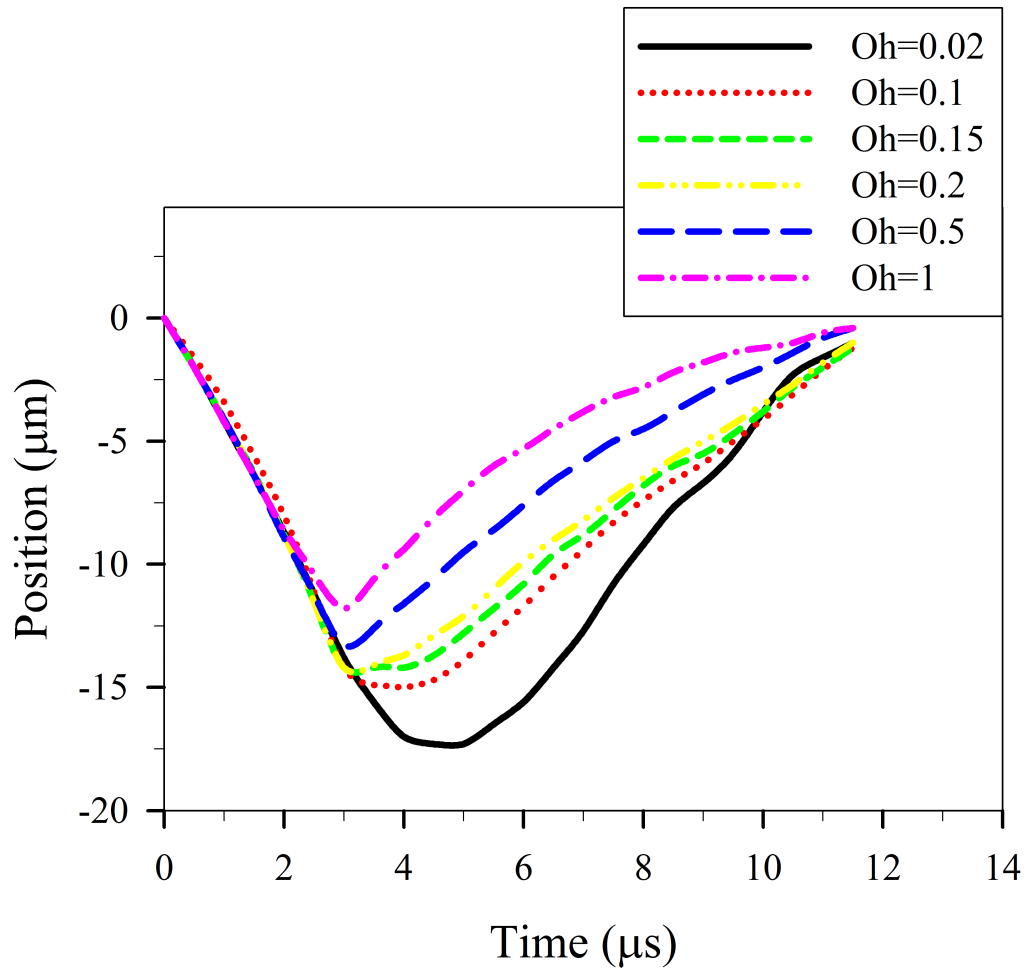
Figure 3.30. Temporal variation of the position of the free surface along the center line of the nozzle.

Chapter 4. Influence of liquid hydrophobicity and nozzle geometry on a drop ejection process

To investigate the effect of the liquid hydropphobicity and nozzle passage curvature on the drop formation process, and simplify the models stemming from the complicated geometry of the interior flow channels in ink-jet printheads, we used a model of a nozzle plate connected with a flat-plate piezoelectric material. To validate the present theoretical models, a comparison between experimental measurements and numerical simulations was devised .

4.1 Physical model and solution methods

Consider a system of a nozzle plate joined to a flat-plate piezoelectric material having a liquid drop on it as shown in Fig. 4.1. When a voltage signal is applied to the piezoelectric material, it alters its dimensions periodically, therefore inducing an acoustic wave to propagate through the nozzle plate and the liquid drop. This propagation of the acoustic wave causes a vibrational motion of the nozzle plate and an oscillating pressure difference between the liquid and the air, thus driving drops to become ejected. Our objective is to observe the influence of the exit diameter of the nozzle, the curvature of the nozzle passage, the wetting conditions of the nozzle passage wall and the vibration of the nozzle plate on the variables of immediate

practical importance such as the drop volume, the speed and the breaking-up time during the drop formation. Shown in Fig. 4.2 is the configuration adopted in our theoretical models and simplified to be axially symmetric in terms of the reality of the experimental arrangement[47].

Here, we consider a hemispherical liquid drop placed on a flat solid wall drilled for liquid protrusion and moving up and down in a specific fashion corresponding to the vibration of the realistic nozzle plate, thus causing a pressure difference between the liquid and the ambient atmosphere so as to expel the liquid drops. According to Feng[23], the assumption that the fluid is incompressible is acceptable, as the propagation wavelength which is estimated to be 7500 μm is greater than the radius of the hemispherical liquid drop 4000 μm. In the current estimate of the propagation wavelength, the speed of the propagation of the acoustic wave in water is approximately 1500 m s^{-1} and the frequency of the acoustic wave is set up to 200 kHz used in the present study. And thus the dynamics of drop formation are governed by the Navier-Stokes equation and the continuity equation for incompressible fluid that obeys the linear Newtonian friction law as shown in Eqs. (1) and (2). In modeling this interfacial phenomenon of the drop formation, we adopt an interface-capturing method, a variation of the VOF scheme, to resolve this transient behavior of the free surface separating two incompressible and immiscible fluids and CSF model to

consider the surface tension effect, as mentioned in Chapter 2.

For the model considered here, the arrangement of the types of boundary condition is shown in Fig. 4.2. The wall boundary meets these conditions:

$$\underline{v} \cdot \underline{n}_{wall} = 0, \tag{20}$$

$$\underline{v} \cdot \underline{t}_{wall} = 0, \tag{21}$$

$$\frac{\partial \overline{p}}{\partial \underline{n}_{wall}} = 0, \tag{22}$$

in which $\underline{n}_{wall}$ and $\underline{t}_{wall}$ represent outward normal and tangential vectors for the wall respectively. To model appropriately the vibration of the nozzle plate, we assume that the instantaneous displacement of the solid wall boundaries adopts a trigonometric form,

$$D = A \cdot \sin(2\pi f t), \tag{23}$$

in which A is the displacement and f frequency. At the outlet boundary, the conditions are satisfied as follows:

$$\overline{p} = \text{constant}, \tag{24}$$

$$\frac{\partial \underline{v}}{\partial \underline{n}_{out}} = 0, \tag{25}$$

$$F = 0. \tag{26}$$

Here, $\underline{n}_{out}$ signifies an outward normal vector on the boundary paths. In addition, the

pressure and velocity inside fluids are initially 1 atm and at rest, respectively. The

initial distribution of liquid and gaseous materials is shown in Fig. 4.2. All

computations were performed with commercial software CFD-ACE+ for

computational fluid dynamics, which is a multipurpose computer code based on

finite-volume discretization to solve the two-dimensional axially symmetric

Navier-Stokes and continuity equations for the velocity and pressure variables. The

velocity-pressure coupling was conducted with an iterative semi-implicit method for

pressure-linked equations in a consistent (SIMPLIC) numerical scheme. The velocity

and pressure fields in a time step were obtained when the convergence criteria are

satisfied. In addition, the specified displacement, given by Eq. (23) was programmed

as a customized user subroutine with a prescribed moving boundary condition, which

is compatible with the CFD-ACE+ computer code.

4.2 Experimental methods and conditions

In order to validate the theoretical models as mentioned above, we used a

high-speed photography for visualizing droplet formation process and utilized the

experimental setup shown schematically in Fig. 4.3. In the present experiments,

droplets are expelled from a nozzle plate connected with a flat-plate piezoelectric

material, as shown in Fig. 4.1. To circumvent the difficulty of flow visualization and

crosstalk of ejected droplets, we placed the nozzles in a row with a hole-to-hole

spacing of 2 mm on the nozzle plate, which is 10 mm in length and 13 mm in width,

as shown in Fig. 4.4 and fabricated by lithography and electroforming [48-50].

Figure 4.5 shows the schematic diagram of the process of fabricating nozzle

plate. The mould patterning and the nickel electroforming were the main processes to

frame the nozzle plate used in this study. A silicon wafer coated with aurum having

100 nm in thickness was used as substrate for constructing the electroforming

components. The positive tone photoresist (AZ 1500) was utilized as electroforming

moulds and nickel the electroforming material. The mechanism of forming nozzle in

substrate was by the over-electroforming around the columnar photoresist mould.

When the thickness of deposited nickel material is larger than the height of columnar

mould, the deposited nickel begins to develop laterally and vertically. The more the

over-electroforming, the smaller the size of nozzle outlet. Therefore, a nozzle with an

ellipsoid-like curvature of passage could be produced. Figure 4.6 shows SEM photo

of a nozzle used in this study. The conductive epoxy adhesive was applied on the

attached interface between the nozzle plate and the piezoelectric material, which is 24

mm in length, 18 mm in width and 0.7 mm in thickness. Moreover, the field of this

attached interface is 1 mm in length and 13 mm in width. If the periodic voltage

signal whose waveform was square, peak-to-peak amplitude 24 V and frequency 63.3

kHz was applied to the piezoelectric material, the nozzle plate would vibrate periodically, which is induced by the deformation of piezoelectric material along with constraint on one edge opposite to nozzle plate, as shown in Fig. 4.7. As mentioned above, the realistic nozzle configuration is approximately axisymmetric to the nozzle center line through the fabrication of lithography and electroforming, as presented in Fig. 4.6. In the present experiment, the gravitational force is directed toward the direction of nozzle center line and the interference of ejected droplets in different nozzle could be ignored due to the large hole-to-hole spacing of up to 2 mm compared to drop size. Moreover, the diameter of nozzle inlet and nozzle outlet is small enough compared to the size of nozzle plate and hemispherical liquid drop on the nozzle plate, so the vibration mode near the nozzle region could be simply assumed to move up and down along the direction of nozzle center line.

The micro-flow visualization system consist of a charge-coupled device (IDT XS-4) equipped with a long distance microscope including 6.5x optical system (Optem zoom-125) and 5x objective lens (Mitutoyo 378-803-2). A high intensity illuminator (Techniquip FOI-250) with 250 Watt was used as light source. The camera can capture images at limited rate of 73 500 frames per second due to the constraint of observed field where the formation of droplet occurs. In the present study, the limited capturing rate of images is insufficient for observing the detailed process of drop

breakup; however, macro features of drop formation including drop volume and drop flight speed could be determined from the sequence of liquid ejection images and compared with theoretical models. The images were then processed by an image acquisition card, displayed on a monitor screen and stored in a personal computer as files. Moreover, the image of a well-defined scale is also examined and captured through the CCD camera with the same magnification of the microscope used to observe the drop ejection process. With the aid of an image processing software (ImageJ 1.42), number of pixels per micrometer can be obtained and the reciprocal of this quantity represent the spatial resolution defined as a length per pixel. Based on the spatial resolution defined, the length of target line is calculated by measuring number of pixels this line holds.

With de-ionized water as the working fluid whose volume was fixed at 100 μL and placed on the center of nozzle plate, the shape of ejected droplet after the oscillation of surface wave is sufficiently decayed by viscous dissipation could be approximated to a sphere whose diameter was determined by measuring the maximum end-to-end distance of the liquid drop on the monitor screen and could be used to estimate the drop volume. In addition, the drop velocity was determined by measuring the displacement of the leading edge of the droplet in a time period, as shown in Fig. 4.8. The uncertainty in the measurement of length is around $\pm 3\mu m$,

which could be attributed to the limit of observed scope and spatial resolution of camera associated with exposure time.

In order to measure the wetting condition of the system, we simply placed a hemispherical water drop on the nozzle plate. The visualization method mentioned above also allows a measurement of the contact angle, which is defined as an angle between the tangent to the drop profile and tangent to the surface at the intersection point of air, liquid and solid, and represents the wetting condition of considered system. The difficulty was in the accurate estimate of the tangent to the curved drop profile since the end point of this curve must be measured. Moreover, this visualization method also requires that the drop was in focus and the base line tangent to the liquid-solid interface was sufficiently clear. All measurements of contact angle can be done by directly using image processing software (ImageJ 1.42). The contact angle of nickel material was measured to be 73°, as shown in Fig. 4.9(a). By conducting reactive ion etching (R.I.E.), we can shift the contact angle of nickel nozzle plate from 73° to 54° due to the change in surface roughness, as shown in Fig. 4.9(b).

4.3 Results and discussion
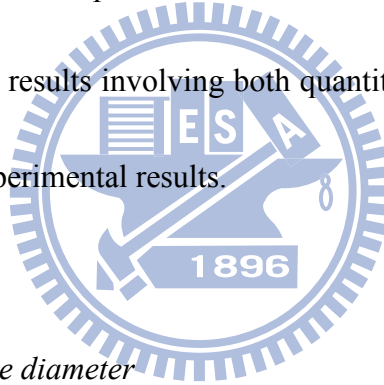
4.3.1 Model validation

In an early stage of this work, we performed tests of the grid dependence with

the total number of grids being about 175 432, 195 388 and 251 496. As shown in Fig.

4.10, the computational domain having the shape of a cylindrical pie slice uses 2D

axially symmetric grids, thus enabling 2D computations in a cylindrical coordinate

system. To achieve a uniform distribution of the discretization errors, we utilized

non-uniform grids that adopt small grid spacing in regions such near the nozzle, the

immediate solid walls and the trajectory of the flight drops for which the derivatives

of the variables alter rapidly and large discretization errors are expected. The solution

domain above the nozzle plate represents a large square 5×10 mm^2 in the *r-z* plane,

which contains the quadrant liquid drop of radius 4 mm. In the nozzle region, the

variation of the curvature of the nozzle passage approximates an elliptic shape. All

other parameters are listed in Table 11. Here, R_{exit} is the radius of the nozzle exit,

$R_{entrance}$ is the radius of the nozzle entrance, *T* is the thickness of the nozzle plate, *A* is

the vibration amplitude of the nozzle plate, *f* is the vibration frequency of nozzle plate

and θ_e is the static contact angle of the nozzle passage wall. With water as a working

fluid, the mass density, viscosity and surface tension are 10^3 kg m^{-1}, 1.0x10^{-3} N s m^{-2}

and 7.27×10^{-2} N m^{-1} respectively. All these parameters are consistent with the

experimental measurements. To obtain the velocity and pressure fields in a time step,

we required that the normalized residual errors of flow variables converge to 10^{-4}. The

entire simulation required 456 h (CPU time on a computer with processor Pentium P4

at 3.0 GHz). The grid convergence study shows that the average drop velocity and

drop volume with 175 432 grids were 20.45 m s^{-1} and 0.045 pL, while those with 195

388 grids were 20.5 m s^{-1} and 0.0442 pL, respectively. Moreover, the average drop

velocity and drop volume with 251 496 grids were 20.9 m s^{-1} and 0.044 pL. These

tests indicate that the 175 432 grids were sufficiently fine, causing an estimated

discretization error smaller than 3 % and achieving a compromise between accuracy

and CPU time. In this study, a simulation case was also carried out to demonstrate the

repeatability of the prediction of drop formation process not shown here.

To validate the present theoretical models, we also made a comparison between

numerical calculations and experimental results. Table 12 offers the parameters used.

Figure 4.11 shows a qualitative comparison of the prediction with the visualized

micro-image of the liquid shape at a time instant. Both experimental and numerical

results showed that the liquid column was ejected continuously in these circumstances

even if the driving force imposing momentum on the liquid drop and induced by the

vibration of the nozzle plate varied periodically.

A quantitative comparison shows that, in case A, the measured volume and

average velocity of each formed drop consistently were 22.812 pL and 4.3 m s^{-1},

whereas the predicted volume and average velocity were 22.657 pl and 4.173 m s^{-1}.

For case B the measured volume and average velocity were 43.009 pL and 6.27 m s^{-1},

whereas the predicted volume and average velocity were 44.16 pL and 6.52 m s^{-1}.

Here, the shape of the liquid drop is approximated as spherical from the breaking-up

point and the average velocity was estimated on measuring the distance of the drop

flight over an interval 10 μs in both numerical and experimental results. The errors

between measured and predicted average velocities are thus 2.9 % for case A and 4.0

% for case B, and the errors of drop volume are 0.68 % for case A and 2.7 % for case

B. In general, the predicted results involving both quantitative and qualitative aspects

agree satisfactorily with experimental results.

4.3.2 The effect of the orifice diameter

As mentioned above, both the visualized experiment and numerical calculations

agree that the liquid strands are discharged continuously under the validation

conditions of our theoretical models given above. The tail of the ejecting drop would

not detach from the remaining liquid portion inside the nozzle during the entire

periodic vibration as shown in Fig. 4.12. A primary drop can be formed about every

three periods of nozzle plate vibration through the destabilizing effect of surface

tension. Fixed under the same conditions as the validation case except for the

diameter of the orifice decreasing to 24 μm, the new liquid drop would overtake and

coalesce into the previous one inside the nozzle after the beginning of the second

periodic vibration as shown in Fig. 4.13.

When the diameter further decreased to 14 μm and 4 μm, the primary drop was

formed and the remaining liquid column then disintegrated into a few small drops, so

called satellite drops during one periodic vibration, but, in the case of diameter 14 μm,

the following liquid column induced by the new vibration moved more rapidly than

the previous satellite decreased, thus causing coalescence of the liquid drops. Figure

4.14 illustrates the effect of the orifice diameter on the average drop velocity and

volume.

The drop volume increased and velocity decreased with increasing diameter. In

the uniformity analysis of the drop volume, the maximum difference between

individual and average drop volumes attained 4.4 % when the orifice diameter was 34

μm. In contrast, when the diameter decreased to 14 μm, the difference increased by 37

%. On the basis of the limited data available, it is certain that when the diameter

equals to 34 μm, the satellite drops could not occur because of a continuous liquid

supplement into an ejected liquid column, and only the uniform primary drops

become formed at the leading edge. When the diameter was decreased to 14 μm,

except for the formation of the primary drop at the leading edge, the liquid portions

that follow tended to disintegrate into a few satellite drops, therefore causing a non-uniform drop volume. Excluding the orifice diameter, 14 µm because of an occurrence of complicated coalescence of liquid drops and the first drop being inconsistent, the analysis of the period for disintegration of the drop shows that for the orifice diameter of 34 µm the breaking point occurred approximately at 77.43 µs whereas at 68.2 µs for a diameter 24 µm. A possible reason might be that the momentum per volume for the diameter of 24 µm is greater than that for the diameter of 34 µm to overcome the restoring effects including viscosity and surface tension.

4.3.3 The effect of the curvature of the nozzle passage

To investigate the influence of the curvature of the nozzle passage on the drop formation, we devised a curvature of six types, as shown in Fig. 4.15. The *x* axis coincides with the nozzle centerline and the *y* axis the direction of the radius. All other parameters and configuration size information are found in Table 13. Figure 4.16 illustrates the effect of the passage curvature, vibrating amplitude and frequency on the average drop velocity. The linear or uncurved type has the greatest drop velocity among all cases. When the vibrational amplitude and frequency increases from 0.25 µm to 1 µm and 100 kHz to 200 kHz, the drop velocity tends to increase. It is unlikely that a varied wall curvature contributed to the distinct distribution of liquid pressure

and thus a pressure difference between the liquid and ambient air, the source of the forward momentum of liquid drops. Notice that the velocity in the flow field of the linear type is as large as 845 m s^{-1} when the vibrational amplitude is 1 μm and 420 m s^{-1} when the frequency is 200 kHz. The Mach number, M$\equiv$u/c, where u is the speed of flow and c the speed of sound is comparable to the value 0.3. Therefore, the constant density assumption is invalid [51]. In other words, the present theoretical models fail to predict the droplet ejection process and dynamics in these cases. In addition, the method for estimating the average primary drop velocity is to measure the displacement of the leading edge of droplet in a time period. According to the research [52], the deceleration, β, of a drop with a radius r_d and speed v_d is

$$\beta = 4.577(\frac{\rho_{air}^{2/5}\mu_{air}^{3/5}}{\rho_d})(\frac{v_d^{7/5}}{r_d^{8/5}}),$$

(27)

in which ρ_{air} is the density of the surrounding air, ρ_d the density of drops and μ_{air} the viscosity of the air. For a drop with a radius of 2 μm and speed of about 100 m s^{-1}, the deceleration is around 1 μm μs^{-2}. In the current simulation, this decreasing velocity of primary drop could be observed in the limit of solution domain. Shown in Fig. 4.17 is the magnitude of the stagnation pressure of different curvature cases along the nozzle centerline when the vibrational amplitude and frequency are 0.25 μm and 100 kHz, respectively. The overall pressure value in the linear case is greater than the

others. The divergent and zero-curvature types might not expel the liquid column from the drops having insufficient forward momentum. Figure 4.18 shows the effect of the wall curvature, the vibration amplitude and frequency on the primary drop volume. The linear type curvature seems to produce the smallest drop volume among all cases with the same vibrational amplitude and frequency. Having a larger forward momentum per unit volume, the ejecting liquid column tended to be thinner and longer, thus causing smaller drops through the destabilizing effect of surface tension. When the vibrational amplitude was increased from 0.25 μm to 1 μm or the vibrational frequency from 100 kHz to 200 kHz, the volume difference for the parabolic type of curvature was the smallest among all curvatures. These results indicate that there is a diminishing return to a decreased drop volume on increasing the forward momentum imposed. The effect of the wall curvature, vibration amplitude and frequency on the duration of formation of the primary drop is shown in Fig. 4.19. The linear cases appeared to have the least time to disintegrate regardless of the amplitude and frequency.

4.3.4 The effect of the dynamic contact angle

The effects of the dynamic contact angle on the drop velocity, volume and duration of formation are shown in Figs. 4.20, 4.21 and 4.22 respectively. All other

parameters and configuration size information are found in Table 14. The drop

velocity increases for the contact angle increasing from 7.1^o to 170°; the variation of

the contact angle caused the effect on the difference between velocities as much as

0.54 % in the linear case compared to a third-order case as much as 60 %. The linear

wall curvature might tend to have large momentum per unit volume in ejecting drops

relative to the variable momentum caused by the effect of contact angle. As shown in

Fig. 4.21, a contact angle smaller than 70° causes an increased impact on the drop

volume among all cases other than the linear type case that appeared to decrease

slightly. For the duration of formation of the primary drop, the results reveal that this

time is relatively small when the wetting condition of nozzle wall is highly

hydrophobic. A decrease in dynamic contact angle leads to an increase in the

formation duration of primary drop except for the case of parabolic-type curvature

which reaches its maximum value at about contact angle $\theta_e=70^o$. Figure 4.23

illustrates the erratic change of the primary drop volume behind breaking-up when

dynamic contact angle is 70°. The difference between maximum and minimum

primary drop volume over a time period is within 1.5%. Based on the above results,

numerical calculations have demonstrated that the effect of the wetting conditions on

droplet formation process has significant difference among various types of the

curvature of the nozzle passage.

Table 11. Parameters for the grid dependence test.

R_{exit}	$R_{entrance}$	T	A	f	θ_e
/ μm	/ μm	/ μm	/ μm	/kHz	/deg
2	40	30	0.25	100	7.1

Table 12. Parameters for the validation cases.

Case	R_{exit}	$R_{entrance}$	T	A	f	θ_e
	/ μm	/ μm	/ μm	/ μm	/kHz	/deg
A	17	55.75	46	0.275	61.703	73
B	22.35	60.35	46	0.34124	64.63	54

Table 13. Parameters and size information pertinent to types of passage curvature.

R_{out}	R_{in}	T	A	f	θ_e
/μm	/μm	/μm	/μm	/kHz	/deg
2	40	30	0.25,1	100,200	7.1

Table 14. Parameters and size information to investigate of the effect of contact angle.

R_{out}	R_{in}	T	A	f	θ_e
/μm	/μm	/μm	/μm	/kHz	/deg
2	40	30	0.25	100	7.1,70,120,170
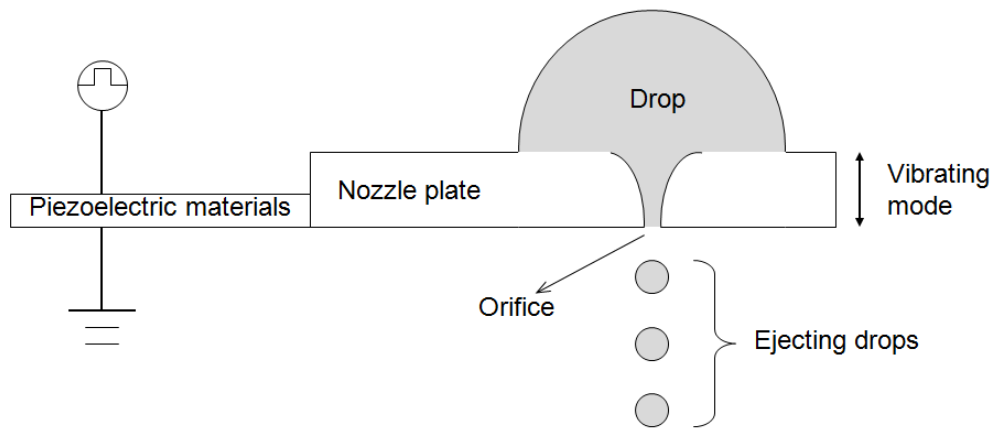
Figure 4.1. Diagram of a nozzle-plate system.
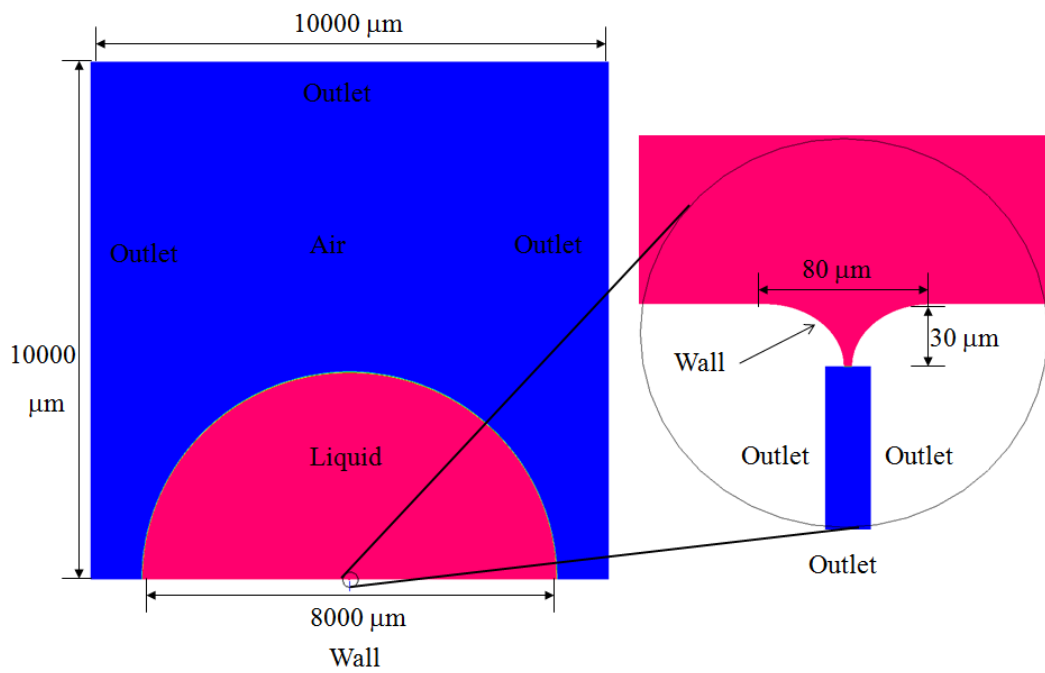
Figure 4.2. Configuration of the computational domain.
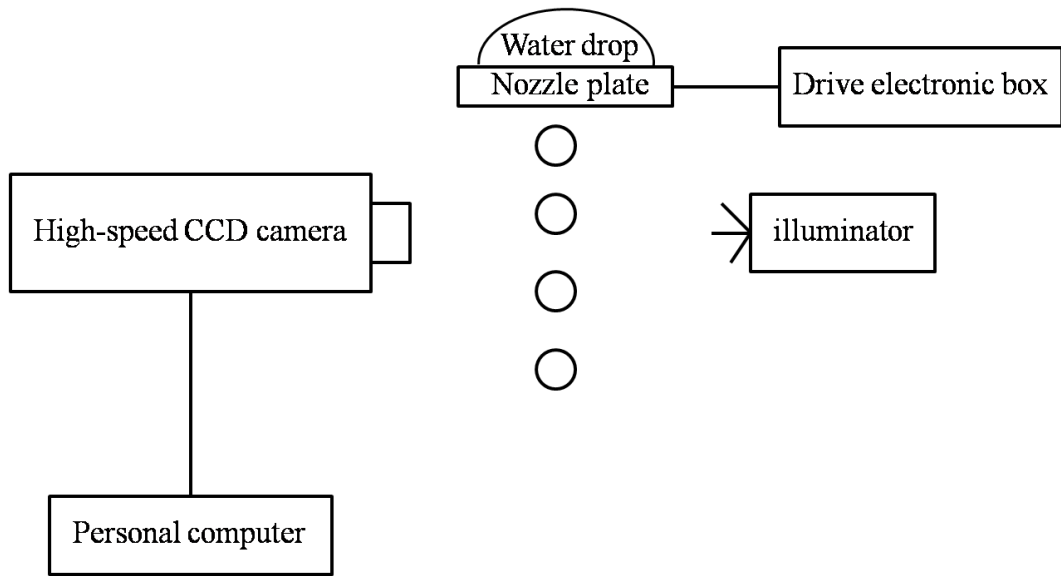
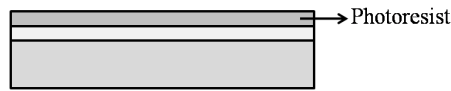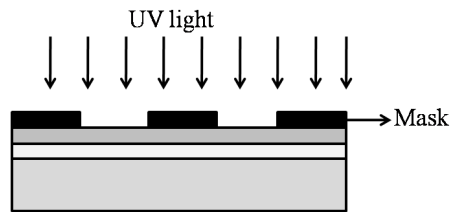**Figure 4.3.**   Schematic diagram of the experimental setup.
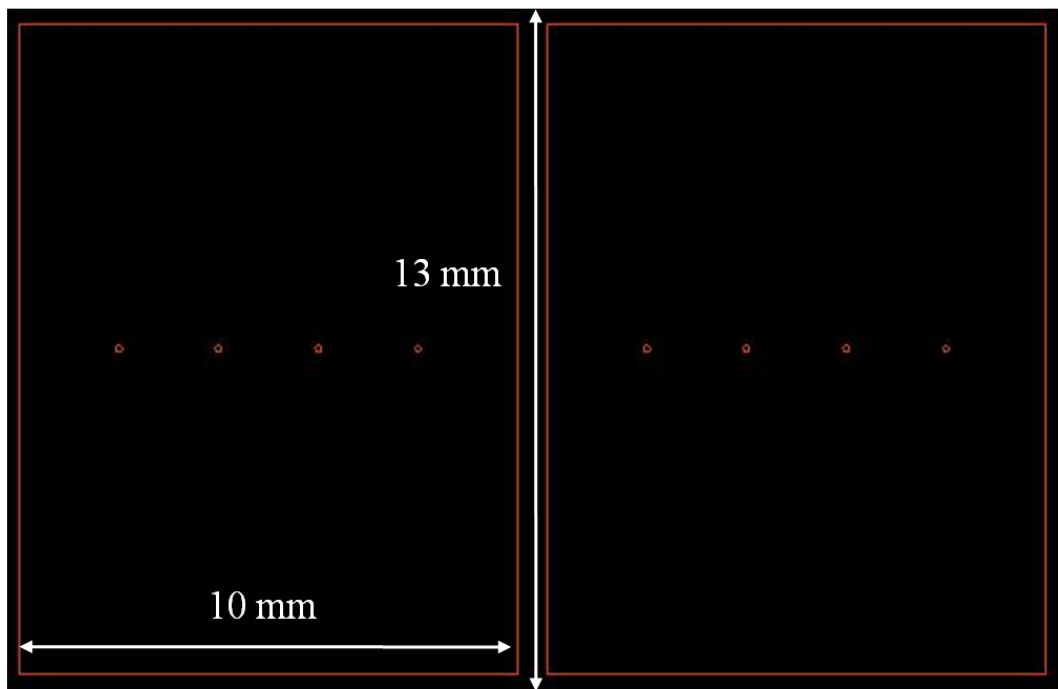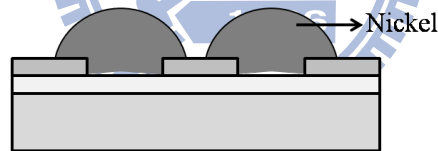
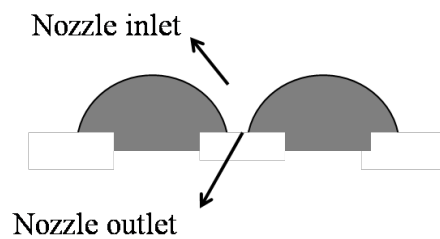

Figure 4.4.   Mask pattern used to fabricate nozzle plate[53].
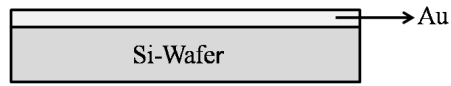
Figure 4.5. Schematic diagram of the process of fabricating nozzle plate: (a) metal deposition, (b) resist coating, (c) UV light exposure, (d) pattern development, (e) electroforming and (f) take off.
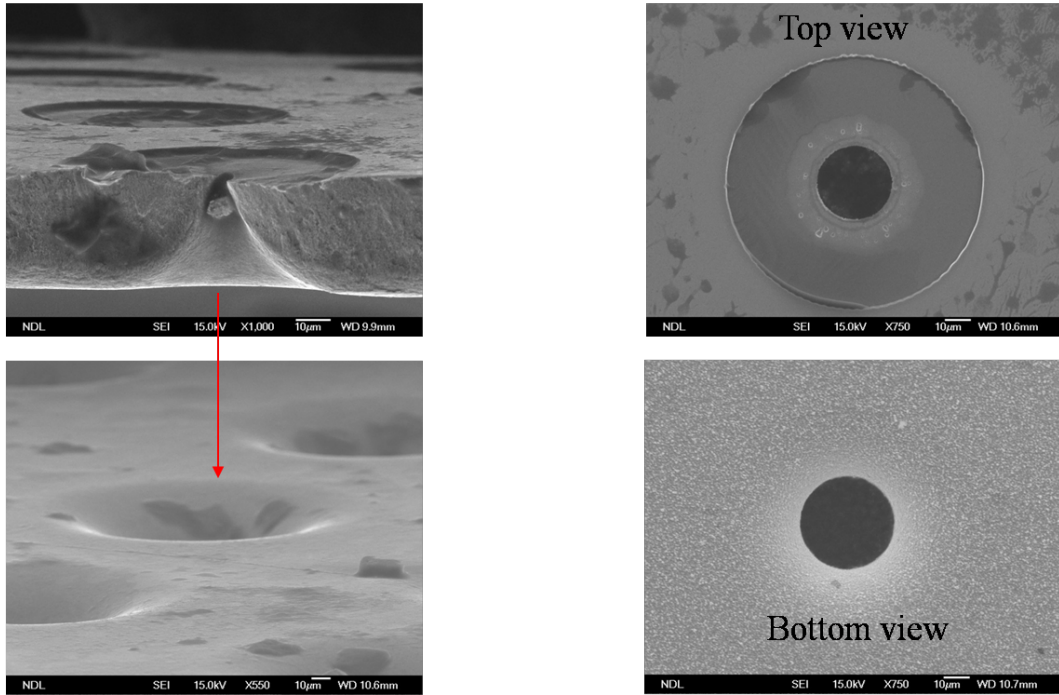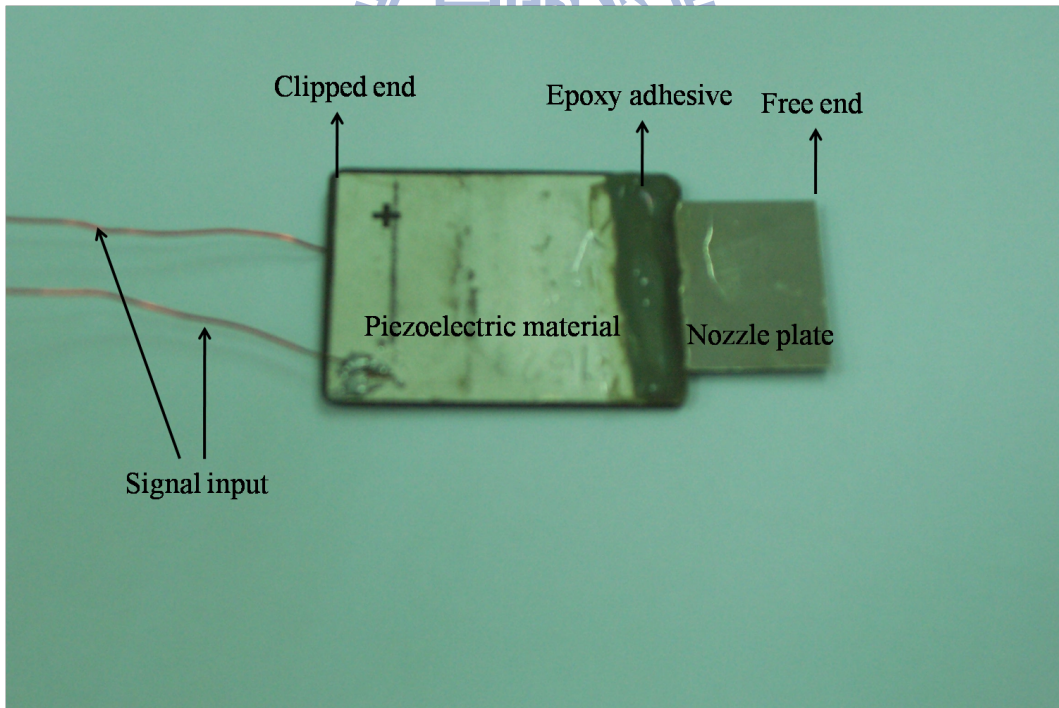
Figure 4.6. SEM photo of a fabricated nozzle[53].

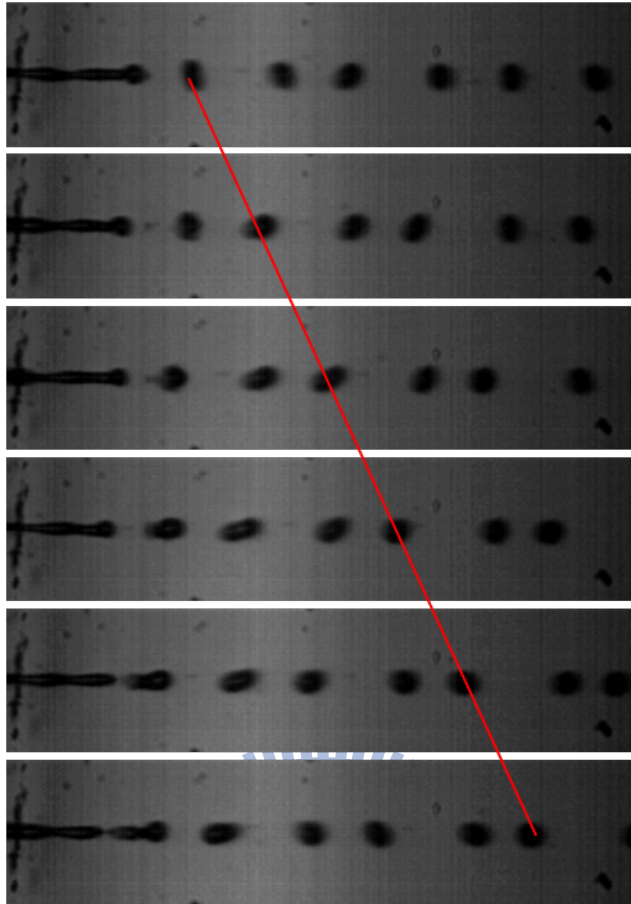**Figure 4.7.** Picture of the nozzle plate connected with piezoelectric material[53].

Figure 4.8. Measurement of droplet velocity using the time sequence of ejected liquid drop; the solid line indicates the same droplet in different time periods[53].
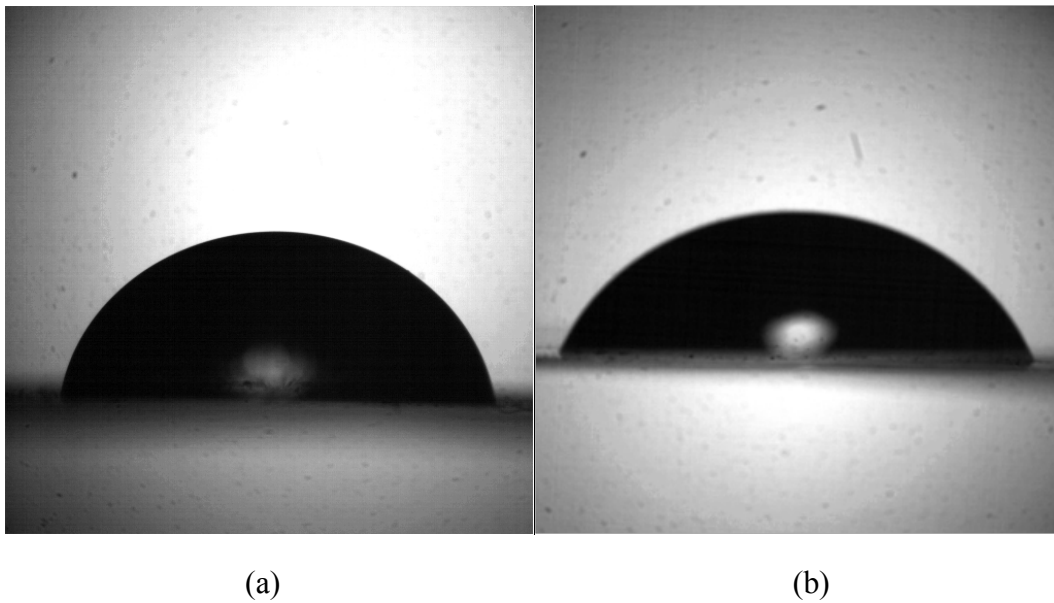

| (a) | (b) |

Figure 4.9. Measurement of contact angle using the visualization method: (a) water drop on nickel surface and (b) water drop on nickel surface processed by R.I.E.[53].
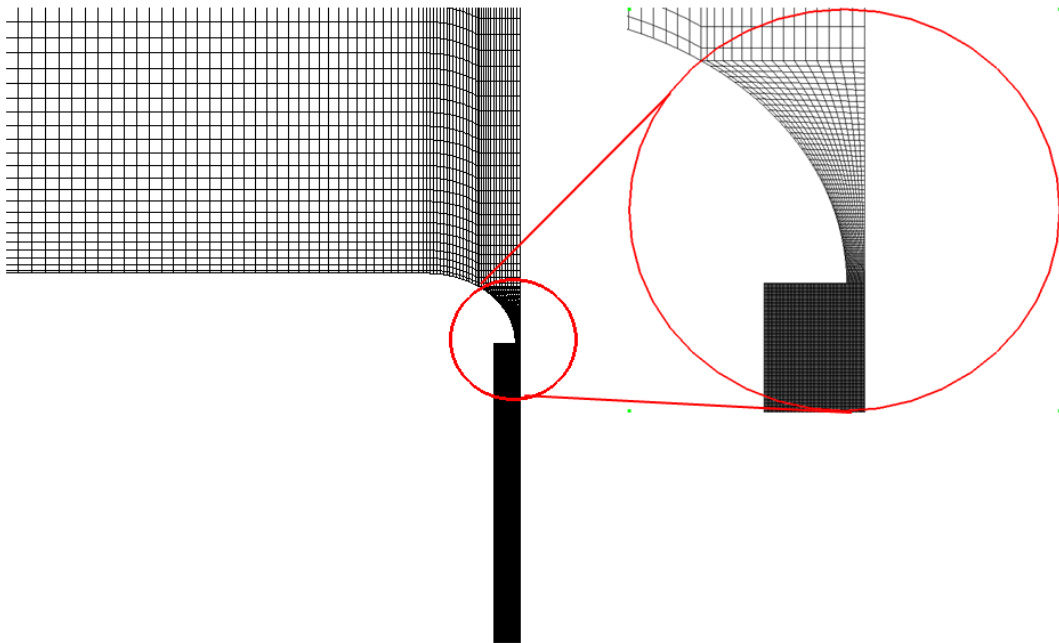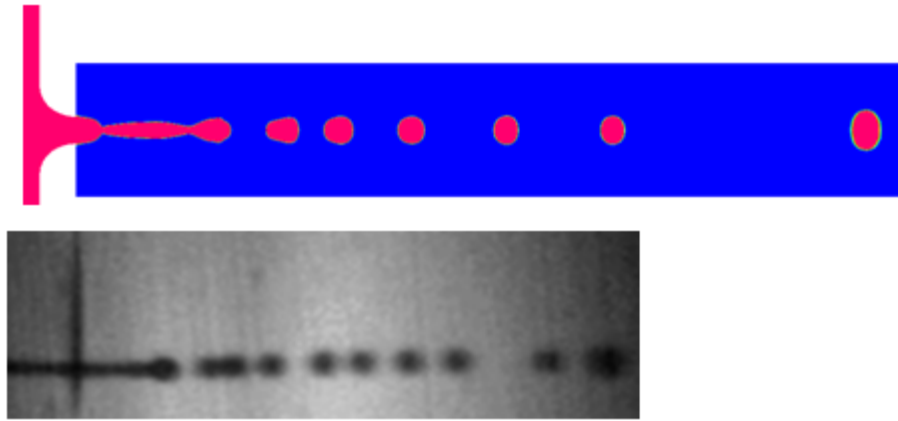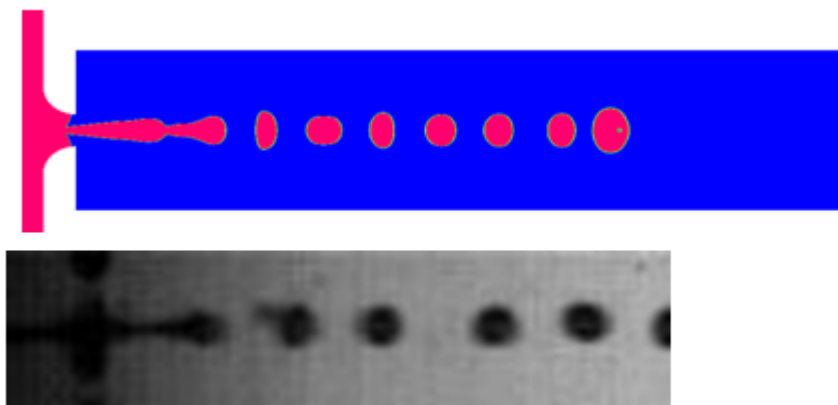
Figure 4.10.   Magnified view of numerical grids neighboring the nozzle exit.

167.44 µs

(a)

174.51 µs

(b)

Figure 4.11.   Comparison of predicted and observed micro-images of the liquid shape: (a) case A, (b) case B.

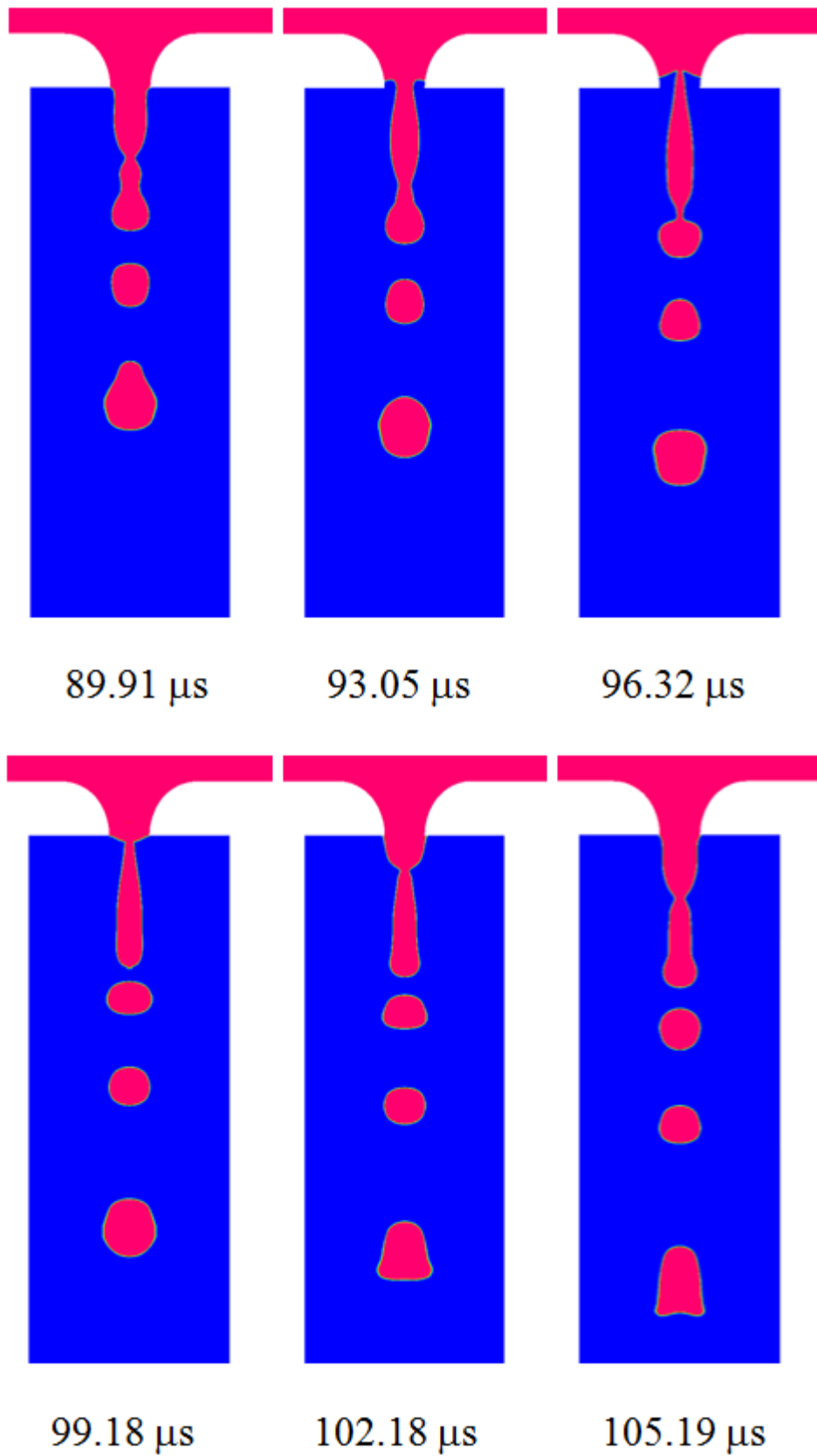| 89.91 μs | 93.05 μs | 96.32 μs |

| 99.18 μs | 102.18 μs | 105.19 μs |

Figure 4.12. Temporal evolution of ejecting drops at a nozzle exit diameter 34 μm.
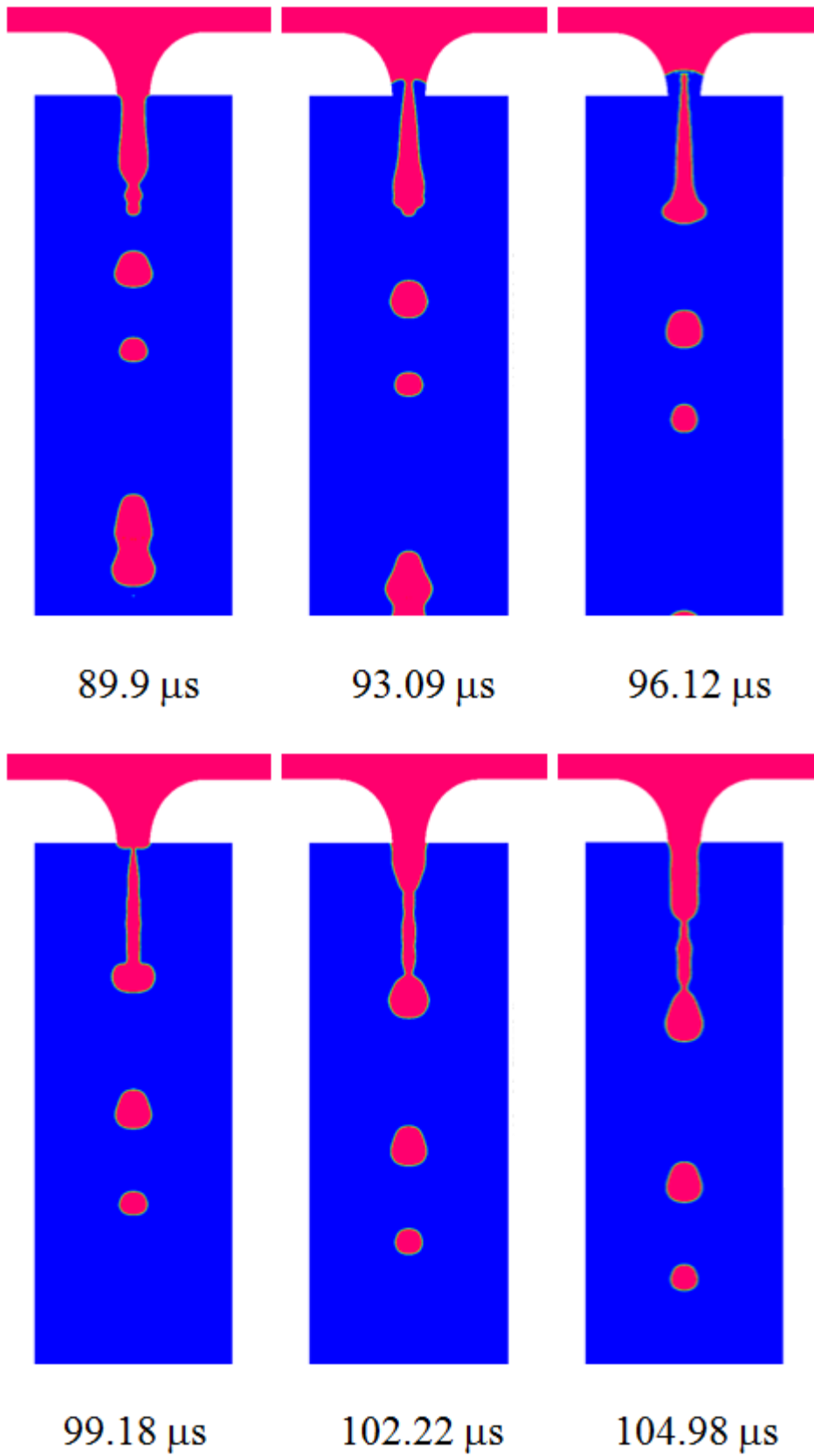
Figure 4.13. Temporal evolution of ejecting drops with nozzle exit diameter 24 μm.
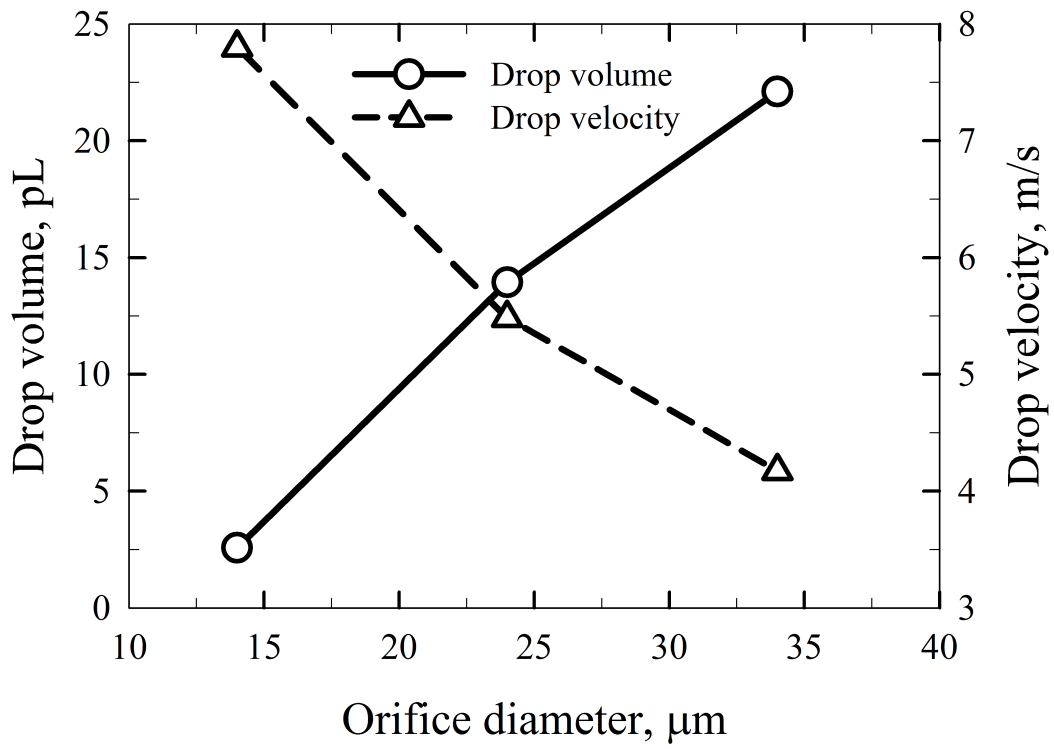
Figure 4.14. Effect of the diameter of the nozzle exit on the average drop velocity and volume.

a: linear type

b: parabolic type

c: elliptic type

d: third order polynomial

e: divergent type (diameter of neck: 2.5 μm)
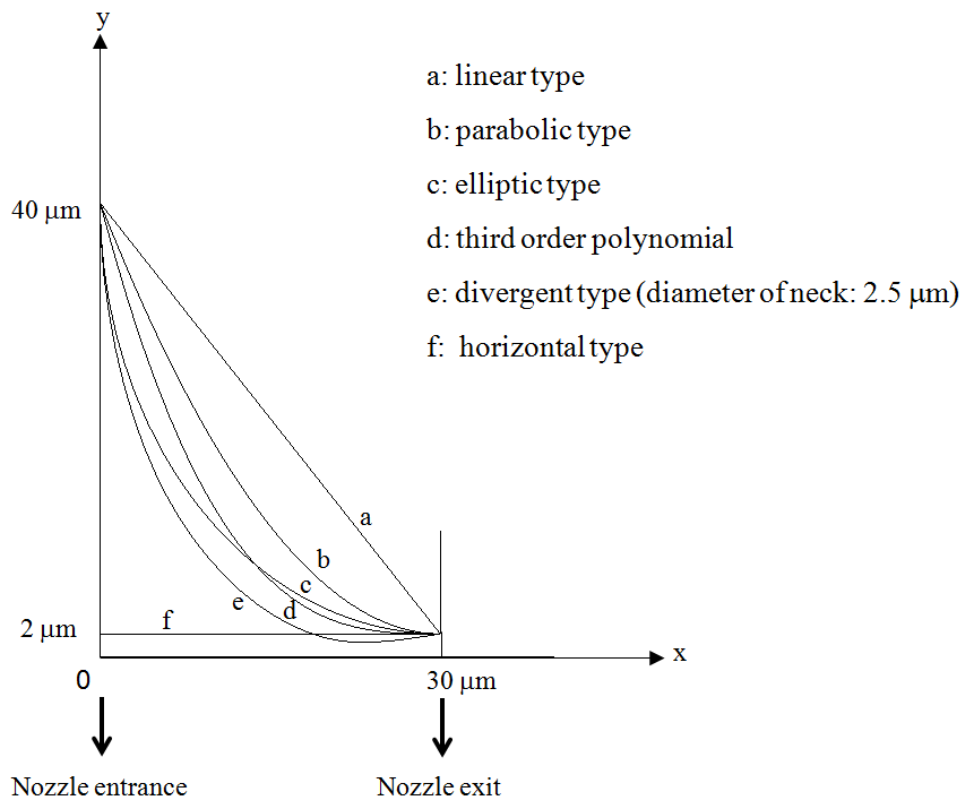
f: horizontal type

Figure 4.15. Types of nozzle passage curvature[54].

Figure 4.16. Effect of the curvature of the nozzle passage on the drop velocity, (a) varied   amplitude with constant frequency 100 kHz and (b) varied frequency with constant amplitude 0.25 μm.

Figure 4.17. Magnitude of stagnation pressure of different curvature cases along the nozzle centerline.

(a)
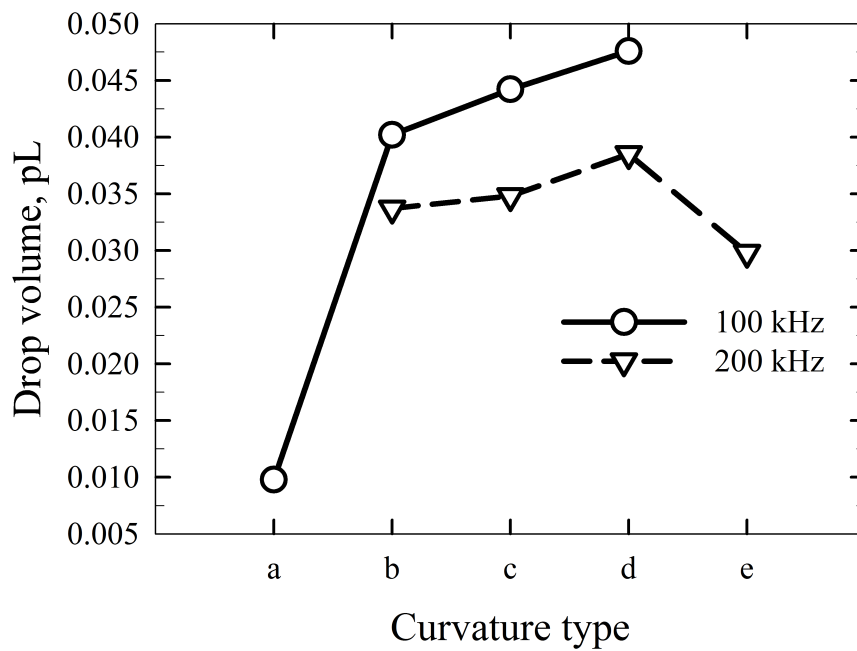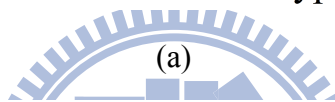
(b)

Figure 4.18. Effect of curvature of the nozzle wall on the primary drop volume, (a) varied amplitude with constant frequency 100 kHz and (b) varied frequency with constant amplitude 0.25 μm.
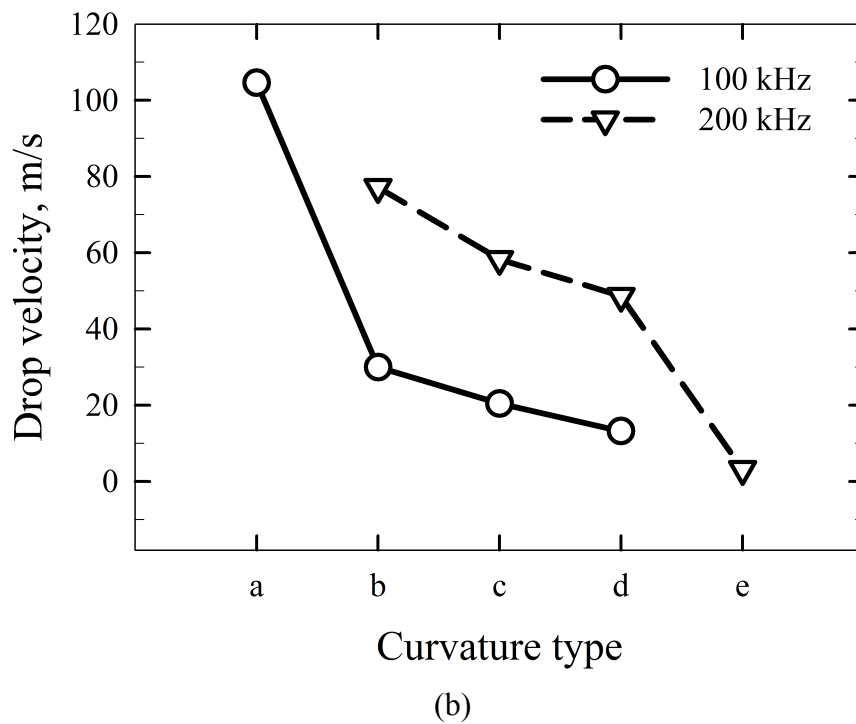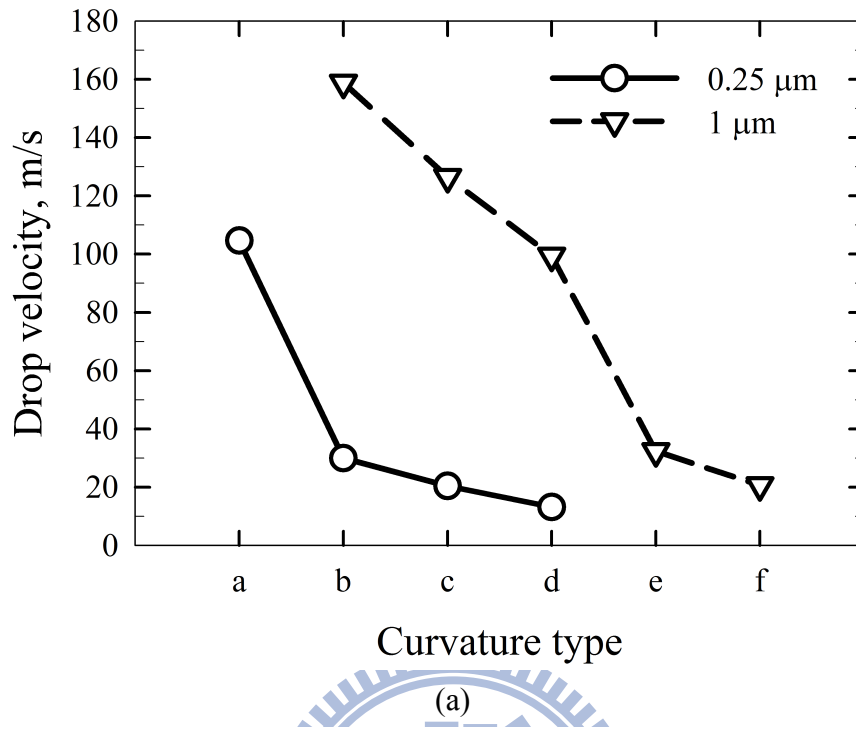
(a)
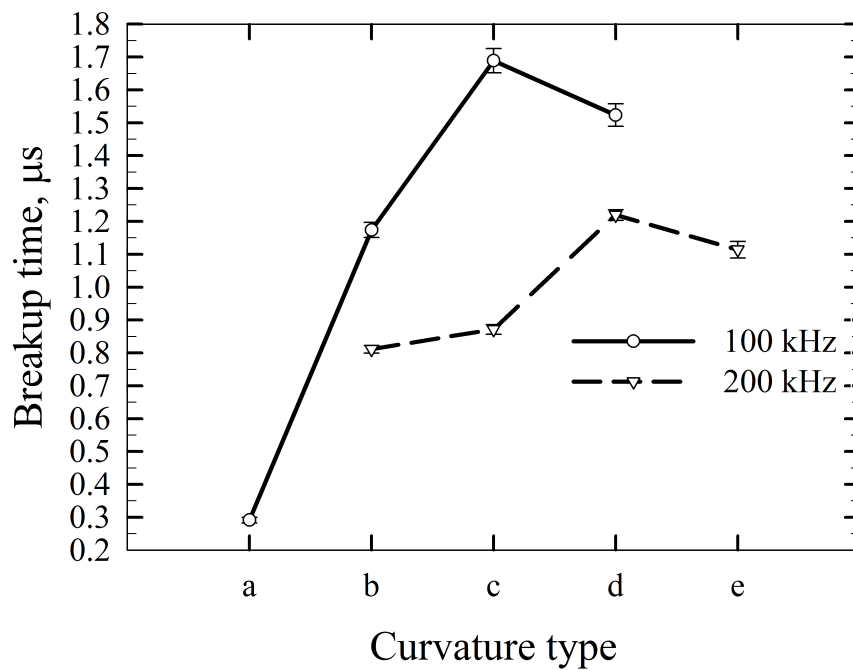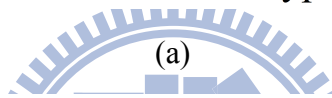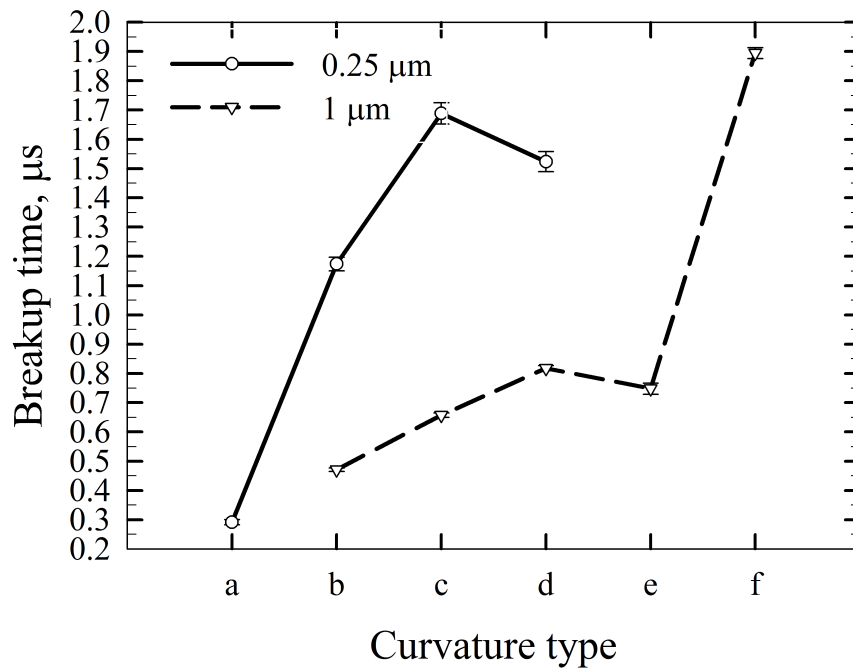
(b)

Figure 4.19. Effect of curvature of the nozzle wall on the drop pinching-off time, (a) varied amplitude with constant frequency 100 kHz and (b) varied frequency with constant amplitude 0.25 μm.
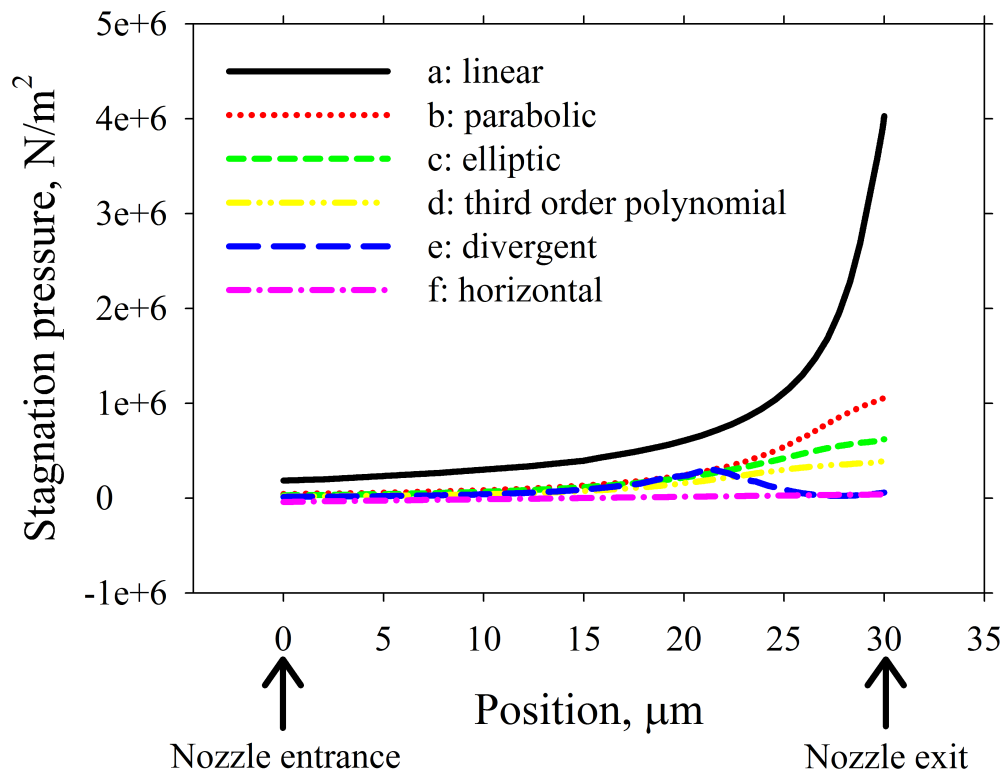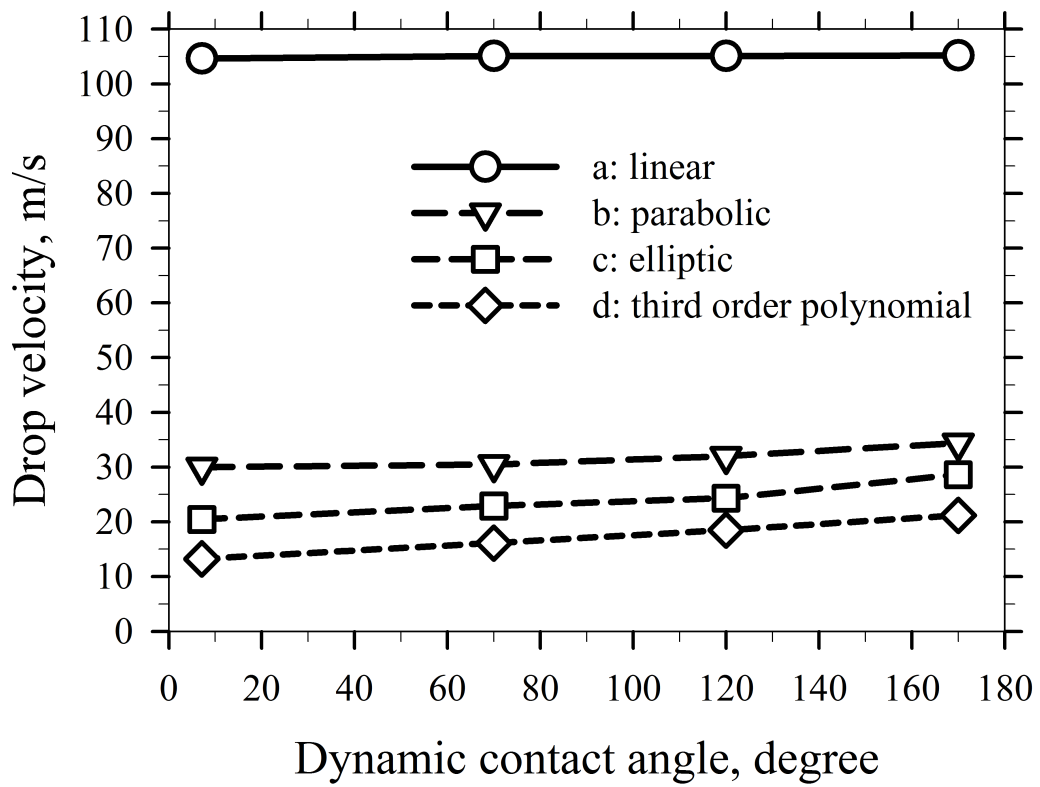
Figure 4.20. Effect of dynamic contact angle on the drop velocity.
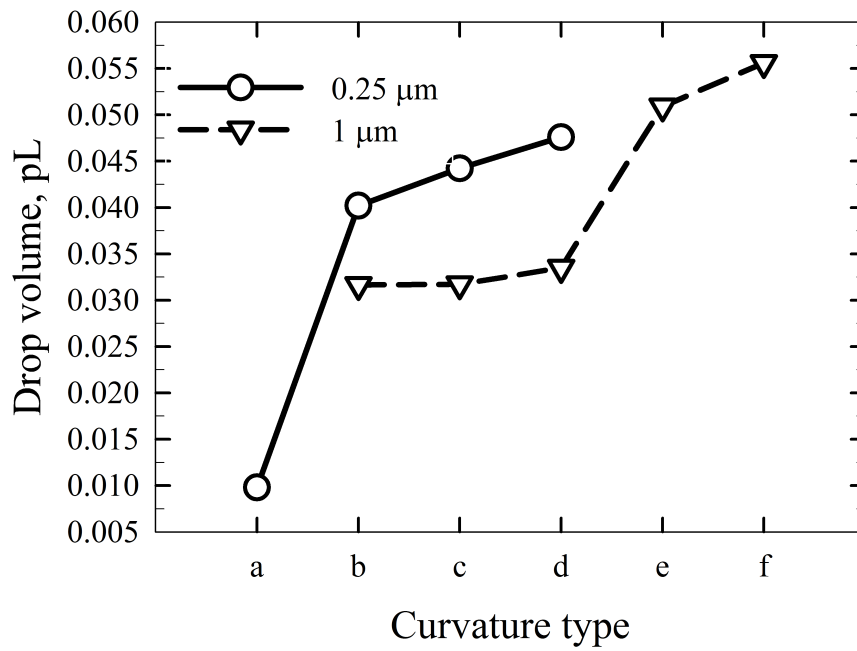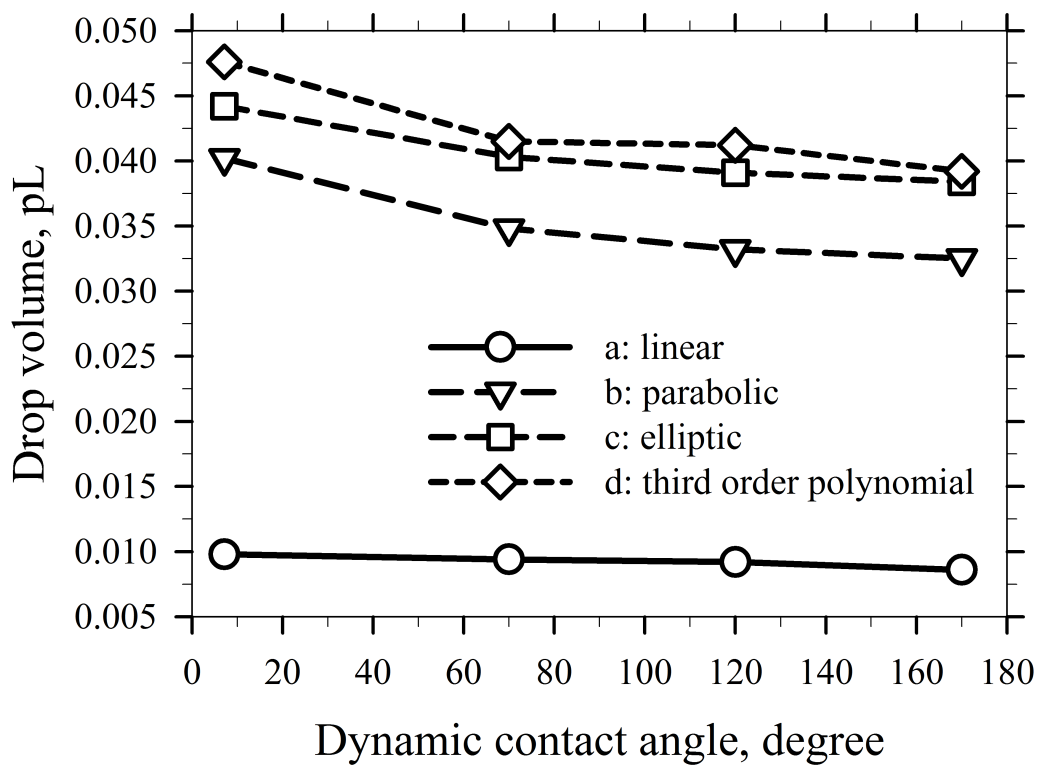
Figure 4.21. Effect of dynamic contact angle on the drop volume.
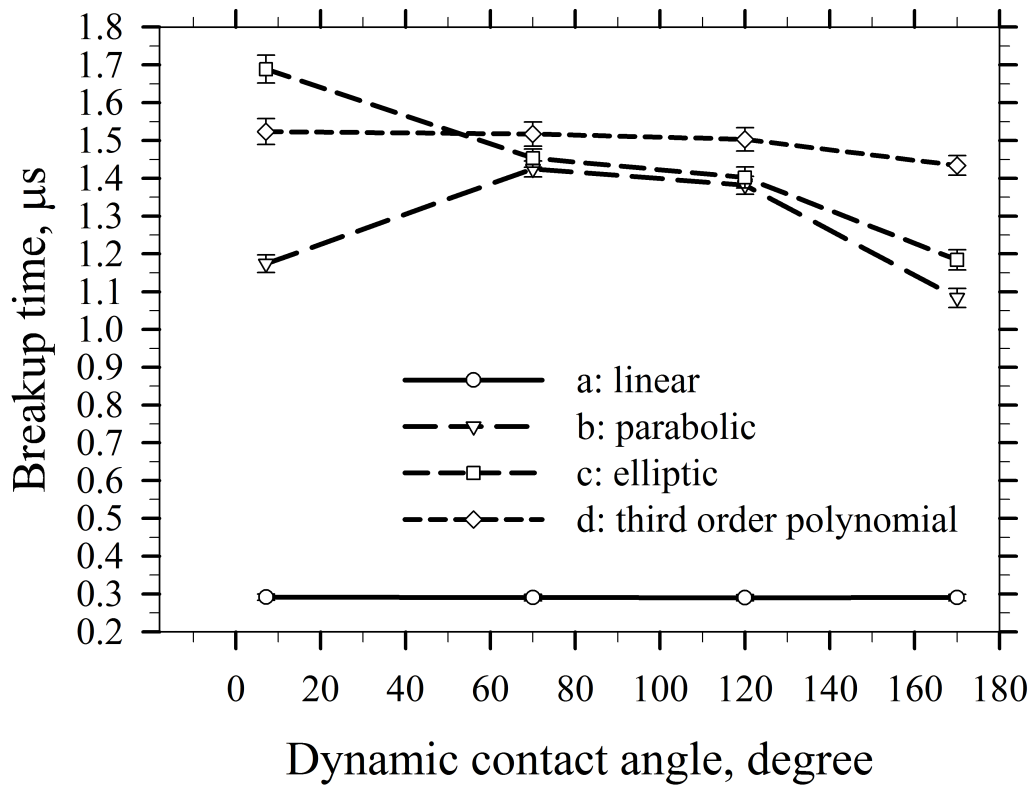
Figure 4.22. Effect of dynamic contact angle on the drop pinching-off time.
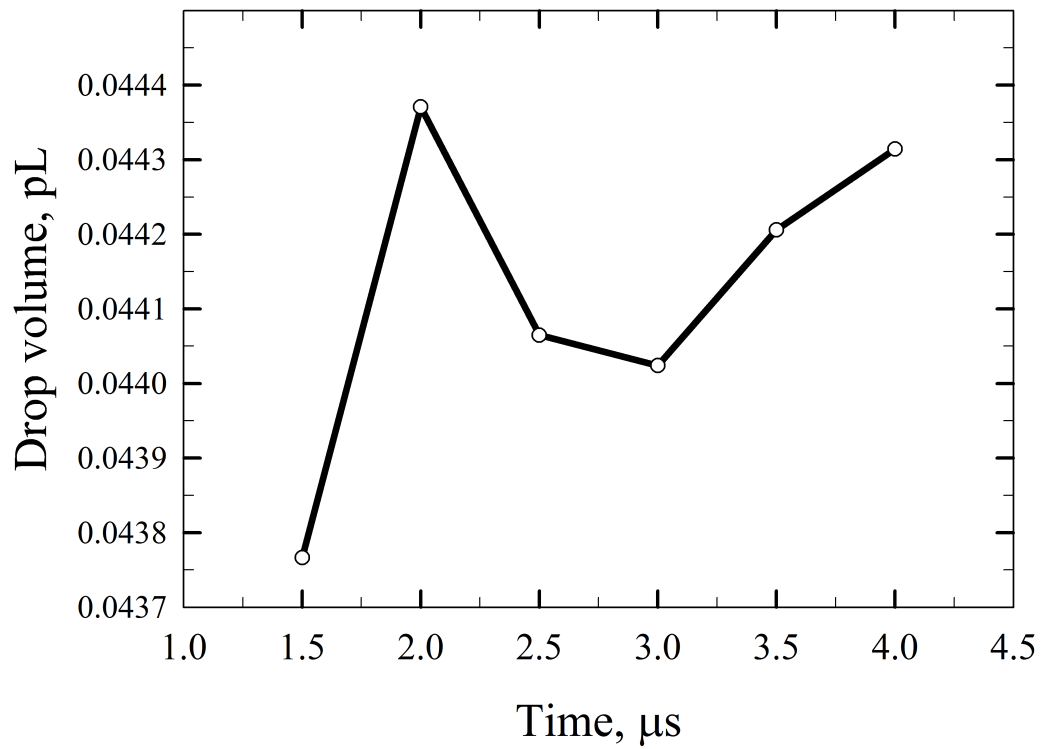
Figure 4.23. Variation of primary drop volume with time behind pinch-off.

Chapter 5. Conclusions and future work

5.1 Conclusions

We conducted numerical simulations to investigate the effect of actuation conditions on the drop ejection of a printhead (Picojet) of DOD type that is commercially available. According to numerical results of the finite-element simulation, the temporary displacement function of the piezoelectric diaphragm displays a trapezoidal shape with higher-order vibration ignored and is divisible into six stages – supply, refill, forward, pause, backward, and equilibrium. The fluid is assumed to be an isothermal, incompressible Newtonian fluid of constant physical properties – density and viscosity. The dynamics of the drop ejection are governed by these independent parameters: We_s, We_f, We_b, D_s, D_f, D_b, $\Delta\tau_{p1}$, $\Delta\tau_{p2}$ and Ohnesorge number Oh, in which We represents Weber number, D the maximum displacement of the piezoelectric diaphragm, $\Delta\tau$ the duration of the different stages of a single transducer pulse and the subscripts s, f, b, $p1$, and $p2$ depict supply, forward, backward, refill, and pause stages, respectively.

For the investigation of the forward stage, the flow inertia, i.e. We_f, must be large enough that a DOD drop can be formed in accordance with intuition. The simulations also show that the volume of the primary drop increases as D_f increases.

These results are consistent with the fact that the larger is the volume displacement of the ink chamber, the larger is the volume of liquid ejected from the DOD nozzle. Increasing We_f might produce an increased velocity of the primary drop. The drop velocity slightly increases when the volume of the ejected drop increases. This result is explicable on assuming that an increased volume of the ejected drop might cause a decreased curvature of the liquid interface, thus accounting for the decreased restoring effect of surface tension.

From the investigation of the backward stage, the velocity and the volume of the primary drop seem to depend weakly on the varied conditions of the backward stroke. The extent of tube invasion by the retracting meniscus is closely related to We_b and $\Delta\tau_b$. From the investigation of the pause stage, the velocity and the volume of the primary drop remain constant but the formation of the satellite drops tends to be suppressed as $\Delta\tau_{p2}$ decreases. There is a strong possibility that decreasing $\Delta\tau_{p2}$ might decrease the length l_b of the liquid thread at pinching off and increase the upper limit l_b^* for the free thread length without satellite formation. This maximum limit l_b^* depends strongly on the time t_{b1} at which the liquid thread pinches off from nozzle outlet, time t_{b2} at which the free liquid thread breaks up into primary drop and secondary liquid thread and the average speed v_r of the retreating thread tail. Moreover, the pinch-off time t_{b1} and breakup time t_{b2} are shown to be

significantly associated with the waveform of the transducer pulse.

Based on the non-dimensional analysis of the system parameters and variables in the present theoretical models, the effect of liquid viscosity can be related to Ohnesorge number $Oh = \mu / \sqrt{\rho R_{noz} \sigma}$, which measures the important of viscous force relative to surface tension force. As Oh increases with constant actuation conditions, the pinching-off and breaking-up time of the ejected liquid increase slightly, while the liquid thread length at pinching off decreases slightly. The primary drop volume tends to be constant with Oh. In addition, a drop ejected at larger Oh tends to move at a slower speed. In some cases with larger Oh, drop breakup may not occur and more powerful actuation is required.

In order to investigate the effect of liquid hydrophobicity and nozzle passage curvature on the drop formation process without interference from the complicated geometry of the interior flow channels in ink jet printheads, we designed a system of a nozzle plate connected to a flat-plate piezoelectric material. A numerical model was constructed and validated by the comparison of simulation results with experimental observation. When the diameter of the orifice equals 34 μm or 24 μm, the liquid strands seem to be expelled continuously and drops with uniform size distribution can be formed in the absence of satellite drops. In contrast, when the orifice diameter equals 14 μm or 4 μm, a primary drop with a few satellite drops are observed. The

drop volume increased and average drop velocity decreased with increasing orifice diameter. Among varied curvatures of the nozzle wall, the linear type seems to have a larger drop velocity, a smaller drop volume and a smaller pinching-off period because of a larger pressure difference between water and ambient air. When the dynamic contact angle was altered from 7.1° to 170°, the drop velocity slightly increased and the volume decreased. The period to pinch off a drop tends to be relatively small when the contact angle is extremely large and small.

The most popular application of ink-jet printheads is to print digital data onto a medium at high resolution. The drop size should hence be as small as practicable, but an ink-jet printhead designed to deliver a small drop size for high resolution undergoes a severe restriction of throughput for an application at poor resolution. A reliable approach to decrease the drop size for one case but not others should hence extend the applicable areas of the specific ink-jet printhead. A prospectively unique capability of piezoelectric printheads is modulation of the drop size with a single transducer pulse having complicated positive and negative parts to manipulate the fluid motion in the nozzle. The results of this work might yield physical insight into the components of the transducer pulse and lead to the development of modulation of the drop size in piezoelectric DOD ink-jet printheads.

5.2 Future work

In this study, a transducer pulse with bipolar waveform was considered for driving a piezoelectric ink-jet printhead (Picojet). This succession of two square-wave pulses induces the suck-push-suck pulses of the pressure in the nozzle flow field. To modulate the drop size with a transducer pulse, it is worthwhile to further investigate the effect of the waveforms with more suck and push pulses on the drop formation of DOD ink jet printheads. The effect of other basic signal waveforms including sine and triangle shapes on the DOD drop formation could be incorporated into future research. In addition, different printheads may have different relation between applied electric pulse and drop formation. Therefore, generality of the results shown in this study is a concern and further investigation using different systems is worthwhile.

This research is based on low-viscosity Newtonian flow. The results should be valid for many DOD applications whose viscosity of dispersed liquid is less than 20 cp. For non-Newtonian fluids such as colloidal and polymeric solutions, further investigation of the influence of a transducer pulse on the DOD drop formation is worthwhile.

References

1. J. F. Dijksman and A. Pierik, "Fluid dynamical analysis of the distribution of ink jet printed biomolecules in microarray substrates for genotyping applications," Biomicrofluidics 2(4), 044101 (2008).

2. Y. Do Kim, J. P. Kim, O. S. Kwon and I. H. Cho, "The synthesis and application of thermally stable dyes for ink-jet printed LCD color filters," Dyes and Pigments 81(1), 45-52 (2009).

3. T. Shimoda, K. Morii, S. Seki and H. Kiguchi, "Inkjet printing of light-emitting polymer displays," MRS Bull. 28(11), 821-827 (2003).

4. B. A. Ridley, B. Nivi and J. M. Jacobson, "All-inorganic field effect transistors fabricated by printing," Science 286(5440), 746-749 (1999).

5. M. Komatsu, Y. Murayama and H. Hashimoto, "Protein fragment imaging using ink jet printing digestion technique," Applied Surface Science 255(1162-1164 (2008).

6. L. Rayleigh, "On the stability of liquid jets," Proc. London Math. Soc. 10(4), (1878).

7. J. Eggers, "Nonlinear dynamics and breakup of free-surface flows," Rev. Mod. Phys. 69(3), 865-929 (1997).

8. S. F. Pond, Inkjet technology and product development strategies, Torrey Pines Research, Carlsbad (2000).

9. R. R. Allen, J. D. Meyer and W. R. Knight, "Thermodynamics and hydrodynamics of thermal ink jets," Hewlett-Packard J. 36(5), 21-27 (1985).

10. Y. Wang and J. Bolkor, "Ultra-high-resolution monolithic thermal bubble inkjet print head," J. Micro-Nanolithogr. MEMS MOEMS 6(4), 10 (2007).

11. P. H. Chen, W. C. Chen and S. H. Chang, "Bubble growth and ink ejection process of a thermal ink jet printhead," Int. J. Mech. Sci. 39(6), 683-695 (1997).

12. K. C. Fan, J. Y. Chen, C. H. Wang and W. C. Pan, "Development of a drop-on-demand droplet generator for one-drop-fill technology," Sens. Actuator A-Phys. 147(2), 649-655 (2008).

13. K. S. Kwon, "Speed measurement of ink droplet by using edge detection techniques," Measurement 42(1), 44-50 (2009).

14. C. D. Meinhart and H. S. Zhang, "The flow structure inside a microfabricated inkjet printhead," J. Microelectromech. Syst. 9(1), 67-75 (2000).

15. T. W. Shield, D. B. Bogy and F. E. Talke, "Drop formation by DOD ink-jet nozzles: a comparison of experiment and numerical simulation," IBM J. Res. Dev. 31(1), 96-110 (1987).

16. H. M. Dong, W. W. Carr and J. F. Morris, "An experimental study of drop-on-demand drop formation," Phys. Fluids 18(7), 16 (2006).

17. A. Asai, "Three-dimensional calculation of bubble growth and drop ejection in a bubble jet printer," J. Fluids Eng.-Trans. ASME 114(4), 638-641 (1992).

18. A. Asai, T. Hara and I. Endo, "One-dimensional model of bubble growth and liquid flow in bubble jet printers," Jpn. J. Appl. Phys. Part 1 - Regul. Pap. Short Notes Rev. Pap. 26(10), 1794-1801 (1987).

19. P. H. Chen, H. Y. Peng, H. Y. Liu, S. L. Chang, T. I. Wu and C. H. Cheng, "Pressure response and droplet ejection of a piezoelectric inkjet printhead," Int. J. Mech. Sci. 41(2), 235-248 (1999).

20. J. E. Fromm, "Numerical calculation of the fluid dynamics of drop-on-demand jets," IBM J. Res. Dev. 28(3), 322-333 (1984).

21. W. T. Pimbley, "Drop formation from a liquid jet: a linear one-dimensional analysis considered as a boundary value problem," IBM J. Res. Dev. 20(2), 148-156 (1976).

22. C. W. Hirt and B. D. Nichols, "Volume of fluid (VOF) method for the dynamics of free boundaries," J. Comput. Phys. 39(1), 201-225 (1981).

23. J. Q. Feng, "A general fluid dynamic analysis of drop ejection in drop-on-demand ink jet devices," Journal of Imaging Science and Technology 46(5), 398-408 (2002).

24. N. Link and R. Semiat, "Ink drop motion in wide-format printers I. Drop flow from Drop-On-Demand (DOD) printing heads," Chem. Eng. Process. 48(1), 68-83 (2009).

25. T. M. Liou, K. C. Shih, S. W. Chau and S. C. Chen, "Three-dimensional simulations of the droplet formation during the inkjet printing process," Int. Commun. Heat Mass Transf. 29(8), 1109-1118 (2002).

26. K. S. Moon, J. H. Choi, D. J. Choi, S. H. Kim, M. H. Ha, H. J. Nam and M. S. Kim, "A new method for analyzing the refill process and fabrication of a piezoelectric inkjet printing head for LCD color filter manufacturing," J. Micromech. Microeng. 18(12), 13 (2008).

27. F. X. Pan, J. Kubby and J. K. Chen, "Numerical simulation of fluid-structure interaction in a MEMS diaphragm drop ejector," J. Micromech. Microeng. 12(1), 70-76 (2002).

28. H. C. Wu, W. S. Hwang and H. J. Lin, "Development of a three-dimensional simulation system for micro-inkjet and its experimental verification," Mater. Sci. Eng. A-Struct. Mater. Prop. Microstruct. Process. 373(1-2), 268-278 (2004).

29. A. S. Yang, J. C. Yang and M. C. Hong, "Droplet ejection study of a Picojet

printhead," J. Micromech. Microeng. 16(1), 180-188 (2006).

30.   N. Anantharamaiah, H. V. Tafreshi and B. Pourdeyhimi, "A simple expression for predicting the inlet roundness of micro-nozzles," J. Micromech. Microeng. 17(5), N31-N39 (2007).

31.   N. Anantharamaiah, H. V. Tafreshi and B. Pourdeyhimi, "Numerical simulation of the formation of constricted waterjets in hydroentangling nozzles - Effects of nozzle geometry," Chem. Eng. Res. Des. 84(A3), 231-238 (2006).

32.   Y. Suh and G. Son, "A level-set method for simulation of a thermal inkjet process," Numer Heat Tranf. B-Fundam. 54(2), 138-156 (2008).

33.   J. D. Yu, S. Sakai and J. Sethian, "A coupled quadrilateral grid level set projection method applied to ink jet simulation," J. Comput. Phys. 206(1), 227-251 (2005).

34.   C. S. Kim, S. J. Park, W. Sim, Y. J. Kim and Y. Yoo, "Modeling and characterization of an industrial inkjet head for micro-patterning on printed circuit boards," Comput. Fluids 38(3), 602-612 (2009).

35.   H. P. Le, H. P. Le and T. P. Le, "Microfluid device and ultrasonic bonding process," U.S. Patent NO. US 6464324 B1 (Oct. 15, 2002).

36.   R. Li, N. Ashgriz and S. Chandra, "Droplet generation from pulsed micro-jets," Exp. Therm. Fluid Sci. 32(8), 1679-1686 (2008).

37.   H. Y. Gan, X. C. Shan, T. Eriksson, B. K. Lok and Y. C. Lam, "Reduction of droplet volume by controlling actuating waveforms in inkjet printing for micro-pattern formation," J. Micromech. Microeng. 19(5), 8 (2009).

38.   Q. Xu and O. A. Basaran, "Computational analysis of drop-on-demand drop formation," Phys. Fluids 19(10), 12 (2007).

39.   W. J. Rider and D. B. Kothe, "Reconstructing volume tracking," J. Comput. Phys. 141(2), 112-152 (1998).

40.   D. B. Kothe, W. J. Rider, S. J. Mosso, J. S. Brock and J. I. Hochstein, "Volume tracking of interfaces having surface tension in two and three dimensions," in AIAA 34th Aerospace Sciences Meeting and Exhibit, pp. 96-0859, Reno, NV (1996).

41.   J. U. Brackbill, D. B. Kothe and C. Zemach, "A continuum method for modeling surface-tension," J. Comput. Phys. 100(2), 335-354 (1992).

42.   M. Renardy, Y. Renardy and J. Li, "Numerical simulation of moving contact line problems using a volume-of-fluid method," J. Comput. Phys. 171(1), 243-263 (2001).

43.   H. A. Stone, B. J. Bentley and L. G. Leal, "An experimental study of transient effects in the breakup of viscous drops," J. Fluid Mech. 173(131-158 (1986).

44. D. Henderson, H. Segur, L. B. Smolka and M. Wadati, "The motion of a falling liquid filament," Phys. Fluids 12(3), 550-565 (2000).

45. P. K. Notz and O. A. Basaran, "Dynamics and breakup of a contracting liquid filament," J. Fluid Mech. 512(223-256 (2004).

46. R. Schulkes, "The contraction of liquid filaments," J. Fluid Mech. 309(277-300 (1996).

47. 沈聖智，王郁人，吳泰鋒，陳易呈，李聰瑞，"微機電技術應用於吸入式霧化器之研發，" 機械工業雜誌 Vol. 269 77-88 (2005).

48. S. C. Chen, C. H. Cheng and Y. C. Lin, "Fabrication of components for a valve-less micropump or microejector by multilevel electroforming technology," in 6th Biennial International Workshop on High Aspect Ratio Micro Structure Technology, pp. 455-463, Springer, Gyenogju, SOUTH KOREA (2005).

49. C. H. Cheng, S. C. Chen and Z. S. Chen, "Multilevel electroforming for the components of a microdroplet ejector by UV LIGA technology," J. Micromech. Microeng. 15(4), 843-848 (2005).

50. W. Ehrfeld, "Electrochemistry and microsystems," in 53rd Annual Meeting of the International-Society-of-Electrochemistry, pp. 2857-2868, Pergamon-Elsevier Science Ltd, Dusseldorf, Germany (2002).

51. P. K. Kundu and I. M. Cohen, Fluid Mechanics, Elsevier Academic Press, San Diego (2004).

52. J. F. Dijksman, "Hydrodynamics of small tubular pumps," J. Fluid Mech. 139(Feb.), 173-191 (1984).

53. C.-Y. Huang, The analysis of Taguchi on droplet ejection process with the nozzle plate connected to a piezoelectric actuator. Master's thesis, National Chiao Tung University (2008).

54. C.-H. Chen, Influence of channel curvature and liquid hydrophobicity on microfluidic dynamics in droplet ejection process. Master's thesis, National Chiao Tung University (2008).

List of publications

1. J. M. Lai, C. Y. Huang, C. H. Chen, L. L. Kung and J. D. Lin, "Influence of liquid hydrophobicity and nozzle passage curvature on microfluidic dynamics in a drop ejection process," J. Micromech. Microeng. 20(1), p. 14 (2010).

2. J. M. Lai and J. D. Lin, "Numerical investigation of the effect of the transducer pulse on the drop ejection process," Proceedings of The 3rd IEEE International Conference on Nano/Molecular Medicine and Engineering, pp. 163-164 (2009), 18-21 October 2009, Tainan, Taiwan.

3. J. M. Lai and J. D. Lin, "An analysis of the effect of liquid hydrophobicity on the drop formation of a piezoelectric print head," Conference Proceedings of International Symposium on Microchemistry and Microsystems, pp. 88-89 (2010), 28-30 May 2010, Hong Kong.

4. J. M. Lai, K. Linliu and J. D. Lin, "Numerical investigation of the effect of a transducer pulse on the microfluidic control of a piezoelectric printhead," J. Micro-Nanolithogr. MEMS MOEMS (Accepted).